Emerging trends of optical interferometry in astronomy

S. K. Saha

Indian Institute of Astrophysics, Bangalore 560034, India.

Abstract. The current status of the high spatial resolution imaging interferometry in optical astronomy is reviewed in the light of theoretical explanation, as well as of experimental constraints that exist in the present day technology. The basic mathematical interlude pertinent to the interferometric technique and its applications in astronomical observations using both single aperture, as well as diluted apertures are presented in detail. An elaborate account of the random refractive index fluctuations of the atmosphere producing random aberrations in the telescope pupil, elucidating the trade offs between long-exposure and short-exposure imaging is given. The formation of speckles and of ways to detect them in the case of astronomical objects are discussed. Further, the other methods viz., (i) speckle spectroscopy, (ii) speckle polarimetry, (iii) phase closure, (iv) aperture synthesis, (v) pupil plane interferometry, (vi) differential speckle interferometry etc., using single moderate or large telescopes are described as well. The salient features of various detectors that are used for recording short-exposure images are summarized. The mathematical intricacies of the data processing techniques for both Fourier modulus and Fourier phase are analysed; the various schemes of image restoration techniques are examined as well with emphasis set on their comparisons. A brief account of obtaining diffraction-limited high resolution features of a few extended objects is presented. The recent technological innovation to compensate the deleterious effects of the atmosphere on the telescope image in real-time is enumerated. The experimental descriptions of several working long baseline interferometers in the visible band using two or more telescopes are summarized. The astrophysical results obtained till date using both single aperture interferometry, as well as long baseline interferometry with diluted apertures are highlighted.

Key words : interferometry, atmospheric turbulence, Fried's parameter, speckle imaging, speckle spectroscopy, speckle polarimetry, single aperture, interferometry, interferometers, aperture synthesis, detectors, image reconstruction, adaptive optics, long baseline interferometry, stellar objects.

S. K. Saha

Table of contents

1. Prologue

Diffraction-limited resolution achievable by any terrestrial large telescope far surpasses that imposed by atmospheric fluctuations above the telescope aperture as against lone orbiting telescope. Turbulence with its associated random refractive index inhomogeneities in the atmosphere distorts the characteristics of light traveling through it. The limitation is due to warping of iso-phase surfaces and intensity variation across the wave-front, thereby, distorting the shapes of the wave-front (Fried, 1966). Due to the diffraction phenomenon, the image of a point source blurs at the focal point of the telescope. This phenomena is present in the sound waves, as well as in the electro-magnetic spectrum starting from gamma rays to radio waves. The blurring suffered by such images is modeled as convolution with the point spread function (PSF). Degradation in image quality can occur because of (i) opto-mechanical aberrations of the telescope and (ii) density inhomogeneities in the path of the optical wave-front. Understanding of the effect of atmospheric turbulence on the structure of stellar images and of ways to overcome the hindrance would enable astronomers to retrieve high spatial resolution of the object.

Though interferometry at optical wavelengths in astronomy began more than a century and a quarter ago (Fizeau, 1868), the progress in achieving high angular resolution has been modest. The first successful measurement of the angular diameter of α Orionis was performed in 1920 using stellar interferometer (Michelson and Pease, 1921), but the field lay dormant until it was revitalized by the development of intensity interferometry (Brown and Twiss, 1958). On the other hand, real progress has been made at radio wavelengths in post war era. Development of long baseline and very long baseline interferometry (VLBI), as well as usage of sophisticated image processing techniques have brought high dynamic range images with milliarc-second (mas) resolution.

The implementation of imaging by interferometry in optical astronomy is a challenging task. Over the last two decades, a marked progress has been witnessed in the development

of this field, offering to realize the potential of the interferometric technique. Single aperture speckle interferometry (Labeyrie, 1970) offers a new way of utilizing the large telescopes to obtain diffraction-limited spatial Fourier spectrum and image features of the object. A profound increase has been noticed in its contribution to measure fundamental stellar parameters, viz., (i) diameter of stars, (ii) separation of close binary stars, (iii) imaging of emission line of the active galactic nuclei (AGN), (iv) the spatial distribution of circumstellar matter surrounding objects, (v) the gravitationally lensed QSO's etc. Further benefits have been witnessed when the atmospherically degraded images of these objects is applied to image restoration techniques (Liu and Lohmann, 1973, Rhodes and Goodman, 1973, Knox and Thomson, 1974, Lynds et al., 1976, Weigelt, 1977, Lohmann et al., 1983, Ayers and Dainty, 1988) for obtaining Fourier phase.

Development of various interferometric techniques, namely, (i) speckle spectroscopy (Grieger and Weigelt, 1992), (ii) speckle polarimetry (Falcke et al., 1996), (iii) pupil plane interferometry (Roddier and Roddier, 1988), (iv) Phase-closure method (Baldwin et al., 1986), (v) aperture synthesis using both partial redundant and non-redundant masking (Haniff et al., 1987, 1989, Nakajima et al., 1989, Busher et al., 1990, Bedding et al., 1992, 1994, Bedding, 1999), (vi) differential speckle interferometry (Petrov et al., 1986) using single aperture telescope have brought out a considerable amount of new results.

Significant improvements in technological innovation over the past several years have brought the hardware to compensate in real-time for telescope image degradation induced by the atmospheric turbulence. Wave-front sensing and adaptive optics (AO) are based on this hardware oriented correction (Babcock, 1953, Rousset et al., 1990). Adaptive optical systems may become standard tool for the new generation large telescopes.

Although large telescope helps in gathering more optical energy, the angular resolution is limited with its diameter. In the optical band, a large mirror of diameter more than 10 m class with high precision in figuring may not be possible to develop, thereby, restricting the resolution in the single aperture interferometry. Introduction of long baseline interferometry using diluted apertures became necessary (Labeyrie, 1975). Success in synthesizing images obtained from a pair of independent telescopes on a North-South baseline configuration (Labeyrie, 1975, Labeyrie et al., 1986, Shao et al., 1988), impelled astronomers to venture towards ground-based very large arrays (Davis et al., 1992). Potentials for progress in the direction of developing large interferometric arrays of telescopes (Labeyrie, 1996) are expected to provide images, spectra of quasar host galaxies, exo-planets that may be associated with stars outside the solar system (Labeyrie, 1995, 1998a, 1998b). Plans are also on to put an interferometer of a similar kind on the surface of the moon by early next century.

The surge of activities in this field over the past two decades reflect the motivation for obtaining true diffraction-limited images with the ground based telescopes. Over the years optical interferometry has slowly gained in importance and today it has become a powerful tool. This review focuses on the application of interferometry to optical astronomy, as well as on the current activities of the various groups across the globe. The problems encountered by the astronomers to develop various interferometers in the optical domain

and possibilities offered to astronomy by high resolution imaging in the optical domain are addressed. The basic principle of interferometry and its applications, atmospheric turbulence and its behaviour in the case of wave propagation, speckle imaging and different interferometric techniques, adaptive optics system, the salient features of long baseline interferometers are enumerated. In addition, the various techniques applied to image restoration and their shortcomings are illustrated. Some of the important results obtained so far using various interferometers are also highlighted.

2. Preamble

Before venturing into the complicated equations pertinent to the interferometric systems, some of the fundamental equations describing a plane wave of monochromatic/quasi-monochromatic light impinging on an ideal instrument, say a telescope, are illustrated.

Let $V(\mathbf{r},t)$ represent the monochromatic optical wave which at a point, $\mathbf{r}$, can be specified in the form, $a(\mathbf{r})e^{-i[2\pi\nu_\circ t - \psi]}$, where, $a(\mathbf{r})$ is the instantaneous complex amplitude of the wave,

$$V(\mathbf{r},t) = \Re\left\{a(\mathbf{r})e^{-i[2\pi\nu_\circ t - \psi]}\right\} \tag{1}$$

Here, $\mathbf{r} = (x,y,z)$ is the position vector of the point (x,y,z), t the time, and $\nu_\circ$ the frequency of the wave.

The complex representation of the analytic signal, $\mathcal{U}(\mathbf{r},t)$, associated with $V(\mathbf{r},t)$ can be expressed as,

$$\mathcal{U}(\mathbf{r},t) = a(\mathbf{r})e^{-i[2\pi\nu_\circ t - \psi]} = \Psi(\mathbf{r})e^{-i2\pi\nu_\circ t}, \tag{2}$$

where, $\Psi(\mathbf{r}) = a(\mathbf{r})e^{i\psi}$, is a complex vector function of position.

From the equations (1) and (2), the relationship can be translated in the form of following equation,

$$V(\mathbf{r},t) = \Re\left\{\Psi(\mathbf{r})e^{-i\omega t}\right\} = \frac{1}{2}\left[\Psi(\mathbf{r})e^{-i\omega t} + \Psi^*(\mathbf{r})e^{i\omega t}\right], \tag{3}$$

where, $\omega = 2\pi\nu_\circ$ is the angular frequency.

The intensity of light is defined as the time average of the amount of energy, therefore, taking the latter over an interval much greater than the period, $T = 2\pi/\omega$, the intensity at the same point is calculated as,

$$\mathcal{I} = <V^2> = \frac{1}{2}\Psi\Psi^*,\tag{4}$$

where, $<>$ stands for the ensemble average of the quantity within the bracket. and Ψ^* represents for the complex conjugate of Ψ.

Since the complex amplitude is a constant phasor in the monochromatic case, the spectrum of the complex representation of the signal, $\mathcal{U}(\mathbf{r}, t)$, is given by,

$$\widehat{\mathcal{U}}(\mathbf{r}, \nu) = a(\mathbf{r})e^{i\psi}\delta(\nu - \nu_0).\tag{5}$$

It is equal to twice the positive part of the instantaneous spectrum, $\widehat{V}(\mathbf{r}, \nu)$. In the polychromatic case, the expression for complex amplitude can be formulated as,

$$\mathcal{U}(\mathbf{r}, t) = 2\int_0^\infty \widehat{V}(\mathbf{r}, \nu)e^{-i2\pi\nu t}d\nu.\tag{6}$$

The disturbance produced by a real physical source is calculated by the integration of the monochromatic signals over a optical band pass. In the case of quasi-monochromatic approximation (if the width of the spectrum, $\Delta\nu \ll \nu_0$), the expression can be read as,

$$\mathcal{U}(\mathbf{r}, t) = |\Psi(\mathbf{r}, t)| e^{i[\psi(t) - 2\pi\nu_0 t]}.\tag{7}$$

The field is characterized by the complex amplitude, $\Psi(\mathbf{r}, t) = |\Psi(\mathbf{r}, t)| e^{i\psi(t)}$; the phasor is time dependent, although it is varying slowly with respect to $e^{-i2\pi\nu_0 t}$.

In the case of 2-dimensional (2-d) distributions of the optical fields in the object and image planes, the following steps are necessary to be incorporated. The distribution of the complex amplitude, $\Psi(\mathbf{x})$, in the image plane for a monochromatic point source of wavelength λ, can be formulated as,

$$\Psi(\mathbf{x}) = \int \mathcal{T}(\mathbf{x}, \mathbf{x}_0)\Psi_0(\mathbf{x}_0)d\mathbf{x}_0,\tag{8}$$

where, $\mathbf{x} = (x, y)$ is a 2-d space vector, $\Psi_0(\mathbf{x}_0)$ is complex amplitude in the telescope pupil plane, $\mathcal{T}(\mathbf{x}, \mathbf{x}_0)$ is the impulse response of the optical system. According to the diffraction theory, $\mathcal{T}(\mathbf{x}, \mathbf{x}_0)$ is proportional to $\int \mathcal{P}(\mathbf{x})e^{-i2\pi\mathbf{x}\cdot\mathbf{x}_0/\lambda}d\mathbf{x}$. Therefore, the equation (8) can be represented as,

$$\Psi(\mathbf{x}) \propto \int \mathcal{P}(\mathbf{x})\Psi_0(\mathbf{x}_0)e^{-i2\pi\mathbf{x}\cdot\mathbf{x}_0/\lambda}d\mathbf{x},\tag{9}$$

where, $\mathcal{P}(\mathbf{x})$ is the pupil transmission function.

The complex amplitudes exhibit a time-dependency in quasi-monochromatic case; therefore, the field in the image plane can be expressed as,

$$\Psi(\mathbf{x}, t) = \int \mathcal{T}(\mathbf{x}, \mathbf{x}_\circ) \Psi_\circ(\mathbf{x}_\circ, t) d\mathbf{x}_\circ. \tag{10}$$

Since the detectors in the visual band are not sensitive to the field but to the intensity, $\mathcal{I}(\mathbf{x})$,

$$\mathcal{I}(\mathbf{x}) = < \Psi(\mathbf{x}, t) \Psi^*(\mathbf{x}, t) > . \tag{11}$$

For an ideal telescope, $\mathcal{P}(\mathbf{x}) = 1$, for inside the aperture and 0 for outside the aperture. In the space-invariant case, the expression for the transfer function can be derived as,

$$\Psi(\mathbf{x}) \propto \int \mathcal{P}(\mathbf{u}) \Psi(\mathbf{u}) e^{-i2\pi \mathbf{x}\mathbf{u}/\lambda} d\mathbf{u}, \tag{12}$$

where, $\int \mathcal{P}(\mathbf{u}) \Psi(\mathbf{u}) e^{-i2\pi \mathbf{x}\mathbf{u}/\lambda} d\mathbf{u} = \int \int_\infty^\infty \mathcal{P}(u, v) \Psi(u, v) e^{-i2\pi[ux+vy]/\lambda} du dv$ and the dimensionless variable, $\mathbf{u}$, stands for $\mathbf{x}/\lambda$, and hence, $\Psi(\mathbf{u})$ can be written for $\Psi_\circ(\lambda\mathbf{u})$.

Similarly, $\mathcal{P}(\mathbf{u}) = \mathcal{P}_\circ(\lambda\mathbf{u})$. From equation (11), it is seen that the complex amplitude in the image plane is the convolution of the complex amplitude of the pupil plane and the pupil transmission function (Goodman, 1968). The mathematical description of the convolution of two functions is of the form:

$$\Psi(\mathbf{x}) = \mathcal{P}(\mathbf{x}) * \Psi_\circ(\mathbf{x}), \tag{13}$$

where, $*$ stands for the convolution operator.

Convolution equations can be reduced to agreeable form using the Fourier convolution theorem. The Fourier transform of a convolution of two functions is the product of the Fourier transform of the two functions. Therefore, in the Fourier plane the effect becomes a multiplication, point by point, of the transfer function of the pupil, $\widehat{\mathcal{P}}(\mathbf{u})$, with the transform of the complex amplitude of the pupil plane, $\widehat{\Psi}_\circ(\mathbf{u})$. i. e.,

$$\widehat{\Psi}(\mathbf{u}) = \widehat{\mathcal{P}}(\mathbf{u}) \cdot \widehat{\Psi}_\circ(\mathbf{u}). \tag{14}$$

The illumination at the focal plane of the telescope observed as a function of the image plane is,

$$\mathcal{S}(\mathbf{x}) = \mid \Psi(\mathbf{x}) \mid^2, \tag{15}$$

where, $\mathcal{S}(\mathbf{x})$, is the PSF produced by both the telescope and the atmosphere and its Fourier transform, $\widehat{\mathcal{S}}(\mathbf{u})$, the optical transfer function (OTF), while its modulus, $\mid \widehat{\mathcal{S}}(\mathbf{u}) \mid^2$, is the modulus transfer function (MTF).

In the ideal condition, the resolution that can be achieved in an imaging experiment, $\mathcal{R}$, is limited only by the imperfections in the optical system and according to Strehl's criterion, is given by the integral of its transfer function.

$$\mathcal{R} = \int \widehat{\mathcal{S}}(\mathbf{u}) d\mathbf{u}. \tag{16}$$

If $\mathcal{R} = \mathcal{S}(0)$, the central intensity in the image is known as Strehl's intensity.

2.1. Interference of two light waves

The astronomical sources emit incoherent light consisting of the random superposition of numerous successive short-lived waves sent out from many elementary radiators, and therefore, the optical coherence is related to the various forms of correlations of the random process. When two light beams from a single source are superposed, the intensity at the place of superposition varies from point to point between maxima, which exceed the sum of the intensities in the beams, and minima, which may be zero, known as interference. The correlated fluctuation can be partially or completely coherent (Born and Wolf, 1984).
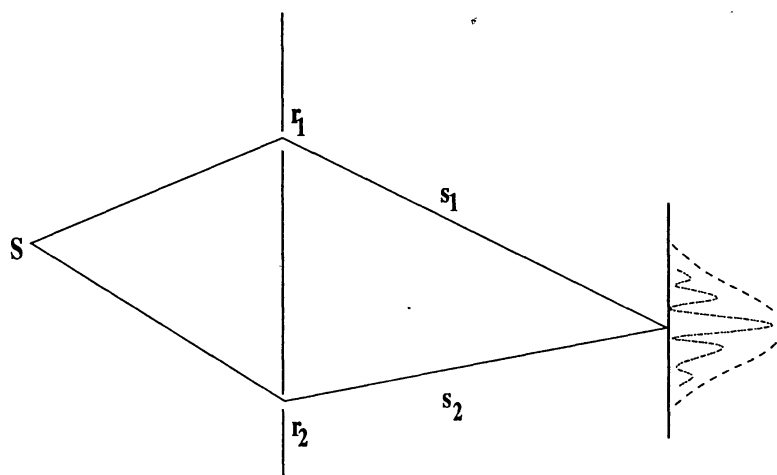

Figure 1. Concept of Young's interferometer.

Figure 1 depicts the concept of Young's interferometer with 2 apertures. Let the two monochromatic waves represented by the vector $\mathbf{V}_1$ and $\mathbf{V}_2$ be superposed at the recombination point. The correlator sums the instantaneous amplitudes of the fields. The total field at the output is,

$$\mathbf{V} = \mathbf{V}_1 + \mathbf{V}_2, \tag{17}$$

$$\mathbf{V}^2 = \mathbf{V}_1^2 + \mathbf{V}_2^2 + 2\mathbf{V}_1\mathbf{V}_2. \tag{18}$$

The total intensity, (see equation 4), at the same point is calculated as,

$$\mathcal{I} = \mathcal{I}_1 + \mathcal{I}_2 + \mathcal{J}_{12}, \tag{19}$$

where, $\mathcal{I}_1 = <\mathbf{V}_1^2>$; $\mathcal{I}_2 = <\mathbf{V}_2^2>$ are the intensities of two waves; $\mathcal{J}_{12} = 2 < \mathbf{V}_1\mathbf{V}_2 >$ is the interference term.

Now, let Ψ_1 and Ψ_2 be the complex amplitudes of the two waves, with the corresponding phases ψ_1 and ψ_2.

$$\mathcal{J}_{12} = \frac{1}{2}\left(\Psi_1\Psi_2^* + \Psi_1^*\Psi_2\right) = 2\sqrt{\mathcal{I}_1\mathcal{I}_2}cos\delta. \tag{20}$$

This expression depicts that the interference term depends on the amplitude components, as well as on the phase-difference between the two waves, $\delta = 2\pi\Delta\varphi/\lambda_o$, where, $\Delta\varphi$, is the optical path difference (OPD) between the two waves from the common source to the intersecting point and λ_o is the wavelength in vacuum. In general, two light beams are not correlated but the correlation term, $\Psi_1\Psi_2^*$, takes significant values for a short period of time and $< \Psi_1\Psi_2^* > = 0$. The total intensity can be derived as,

$$\mathcal{I} = \mathcal{I}_1 + \mathcal{I}_2 \pm 2\sqrt{\mathcal{I}_1\mathcal{I}_2}\ cos\delta. \tag{21}$$

The maximum and minimum intensity can be obtained, when $\mid \delta \mid = 0, 2\pi, 4\pi$ and $\mid \delta \mid = \pi, 3\pi, 5\pi$, respectively. If $\mathcal{I}_1 = \mathcal{I}_2$,

$$\mathcal{I} = 4\mathcal{I}_1 cos^2\frac{\delta}{2}. \tag{22}$$

The intensity varies between $4\mathcal{I}_j$, and 0.

Unlike the monochromatic wave field, where the amplitude of the vibration at any point is constant and the phase varies linearly with time, the amplitude and phase in the case of the quasi-monochromatic wave field, undergo irregular fluctuations (Born and Wolf, 1984). The rapidity of fluctuations depends on the effective width of the spectrum.

The interferometers based on, viz., (i) wave-front division (Young's experiment), (ii) amplitude division (Michelson's interferometer) are generally used to measure spatial coherence and temporal coherence respectively. On the other hand, Young's holes (see figure 1) set-up is sensitive to the bandwidth of the source. A mathematical description of the Young's experiment is as follows.

Let the analytical signal, $\mathcal{U}(t)$, obtained at the output be,

$$\mathcal{U}(t) = \mathbf{K}_1 \mathcal{U}(r_1, t - \tau_1) + \mathbf{K}_2 \mathcal{U}(r_2, t - \tau_2), \tag{23}$$

where, $\mathbf{K}_j$'s are the constants, r_j's the positions of two pin-holes in the wave field, $j = 1, 2$, s_j's the distances of a meeting point of the two beams from the two pin-holes, $\tau_j = s_j/c$, the time needed to travel from the respective pin-holes to the meeting point, and c the velocity of light.

If the pin-holes are small and the diffracted fields are considered to be uniform, the intensity at the output can be expressed as,

$$\mathcal{I} = \mid \mathbf{K}_1 \mid^2 < \mid \mathcal{U}(r_1, t - \tau_1) \mid^2 > + < \mid \mathbf{K}_2 \mid^2 \mathcal{U}(r_2, t - \tau_2) \mid^2 > + \mathbf{K}_1 \cdot \mathbf{K}_2^* \times$$

$$< \mathcal{U}(r_1, t - \tau_1)\mathcal{U}^*(r_2, t - \tau_2) > + \mathbf{K}_1^* \cdot \mathbf{K}_2 < \mathcal{U}^*(r_1, t - \tau_1)\mathcal{U}(r_2, t - \tau_2) >, \tag{24}$$

If the value of the constants can be put as, $\mid \mathbf{K}_j \mid = K_j$; it turns out to be, $\mathbf{K}_1^* \cdot \mathbf{K}_2 = \mathbf{K}_1 \cdot \mathbf{K}_2^* = K_1 K_2$ and noting, $\mathcal{I}_j = \mid \mathbf{K}_j \mid^2 < \mid \mathcal{U}(r_j, t - \tau_j) \mid^2 >$, and therefore, equation (24) leads to,

$$\mathcal{I} = \mathcal{I}_1 + \mathcal{I}_2 + 2K_1 K_2 \Re \left[\boldsymbol{\gamma}_{12} \left(\frac{s_2 - s_1}{c} \right) \right]. \tag{25}$$

The Van Cittert-Zernicke theorem states that the modulus of the complex degree of coherence (describes the correlation of vibrations at a fixed point and a variable point) in a plane illuminated by a incoherent quasi-monochromatic source is equal to the modulus of the normalized spatial Fourier transform of its brightness distribution (Born and Wolf, 1984). The complex degree of (mutual) coherence, $\boldsymbol{\gamma}_{12}(\tau)$, of the observed source is defined as,

$$\boldsymbol{\gamma}_{12}(\tau) = \frac{\boldsymbol{\Gamma}_{12}(\tau)}{\sqrt{\boldsymbol{\Gamma}_{11}(0)\boldsymbol{\Gamma}_{22}(0)}} = \frac{\boldsymbol{\Gamma}_{12}(\tau)}{\sqrt{\mathcal{I}_1 \mathcal{I}_2}}. \tag{26}$$

The function, $\boldsymbol{\Gamma}_{12}(\tau) = < \mathcal{U}(r_1, t+\tau)\mathcal{U}^*(r_2, t) >$, is measured at two points. At a point where both the points coincide, the self coherence, $\boldsymbol{\Gamma}_{11}(\tau) = < \mathcal{U}(r_1, t + \tau)\mathcal{U}^*(r_1, t) >$, reduces to ordinary intensity. When $\tau = 0$, $\boldsymbol{\Gamma}_{11}(0) = \mathcal{I}_1; \boldsymbol{\Gamma}_{22}(0) = \mathcal{I}_2$. The ensemble average can be replaced by a time average due to the assumed ergodicity of the fields. If

both the fields are directed on a quadratic detector, it yields the desired cross-term (time average due to the finite time response). The measured intensity at the detector would be,

$$\mathcal{I} = \mathcal{I}_1 + \mathcal{I}_2 + 2\sqrt{\mathcal{I}_1 . \mathcal{I}_2} \Re \left[\boldsymbol{\gamma}_{12} \left(\frac{s_2 - s_1}{c} \right) \right]. \tag{27}$$

In order to keep the time correlation close to unity, the delay, τ, must be limited to a small fraction of the temporal width or coherence time, $\tau_c = 1/\Delta\nu$; here, $\Delta\nu$, is the spectral width. The relative coherence of the two beams diminishes with the increase of path length difference, culminating in a drop in the visibility of the fringes. A factor less than unity affects the degree of coherence. The corresponding limit for the OPD between two fields is the coherence length, defined by $l_c = c \cdot \tau_c = (\lambda_o)^2/\Delta\lambda$. If $\tau \ll \tau_c$; the function, $\boldsymbol{\gamma}_{12}(\tau)$, can be expressed as, $\boldsymbol{\gamma}_{12}(0)e^{-2\pi i \nu_o \tau}$, The exponential term is nearly constant and $\boldsymbol{\gamma}_{12}(0)$, measures the spatial coherence. Let ψ_{12}, be the argument of $\boldsymbol{\gamma}_{12}(\tau)$, then,

$$\mathcal{I} = \mathcal{I}_1 + \mathcal{I}_2 + 2\sqrt{\mathcal{I}_1, \mathcal{I}_2} \Re \left[|\boldsymbol{\gamma}_{12}(0)| e^{i(\psi_{12} - 2\pi\nu_o\tau)} \right]. \tag{28}$$

The measured intensity at a distance x from the origin (point at zero OPD) on a screen at a distance, z, from the aperture (see figure 1) is

$$\mathcal{I}(x) = \mathcal{I}_1 + \mathcal{I}_2 + 2\sqrt{\mathcal{I}_1, \mathcal{I}_2} |\boldsymbol{\gamma}_{12}(0)| \cos \left\{ \frac{2\pi d(x)}{\lambda} - \psi_{12} \right\}, \tag{29}$$

where, $d(x) = b.x/(z,\lambda)$, is the OPD corresponding to x, and b the distance between the two apertures.

The modulus of the spatial coherence of collected fields at the aperture appears through the contrast of the fringes, V, and is measured by the equation,

$$\mathcal{V} = \frac{\mathcal{I}_{max} - \mathcal{I}_{min}}{\mathcal{I}_{max} + \mathcal{I}_{min}} = |\boldsymbol{\gamma}_{12}(0)| \frac{2\sqrt{\mathcal{I}_1 \mathcal{I}_2}}{\mathcal{I}_1 + \mathcal{I}_2}. \tag{30}$$

2.2. Experiments to measure stellar diameter

In order to produce Young's fringes at the focal plane of the telescope, Fizeau (1868) had installed a screen with two holes on top of the telescope and found the relationship between the aspect of interference fringes and the angular size of the light source. According to him, these fringes remain visible in presence of seeing, therefore, allow measurements of stellar diameters with diffraction-limited resolution. Stefan attempted with 1 meter

S. K. Saha

(m) telescope at Observatoire de Marseille and fringes appeared within the common Airy disk of the sub-apertures. But he could not notice any significant drop of fringe visibility. Since the maximum achievable resolution is limited by the diameter of the telescope, he concluded none of the observed stars approached 0.1 arc-second ($''$) in angular size. Later, Michelson measured the diameter of the satellites of Jupiter with Fizeau interferometer on top of the Yerkes refractor. Similar interferometer (Fizeau mask) was placed on top of the 100 inch telescope at Mt. Wilson Observatory (Anderson, 1920) and the angular separation of the spectroscopic binary star, Capella, was measured. A similar experiment has been conducted by Saha et al., (1987) at VBO, Kavalur using 1 m Carl-Zeiss telescope and recorded the fringes of several bright stars through a broadband filter in the blue region using a 16 millimeter (mm) movie camera giving an exposure of 16 milliseconds (ms) per frame; a Barlow lens was used to magnify the image scale.
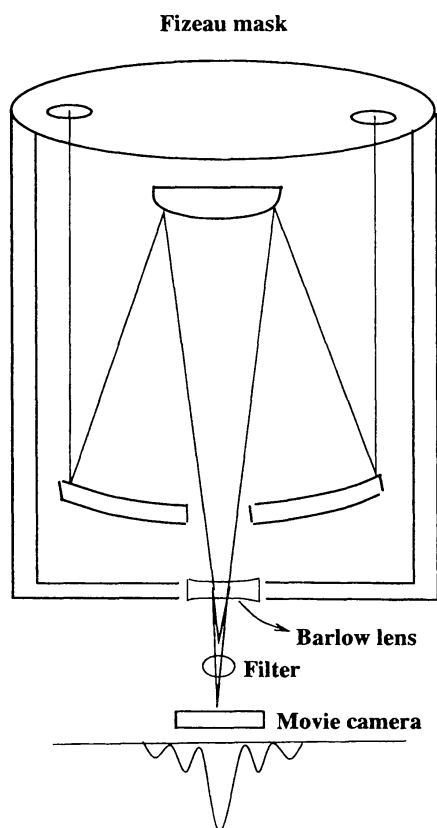
Figure 2. Fizeau - Stefan interferometer using mask over the 1 m telescope at Vainu Bappu Observatory, Kavalur, India (Saha et al., 1987).

Figure 2 describes the concept of the Fizeau - Stefan interferometer. In this, the beams are diffracted by the sub-apertures in front of a telescope which acts as both collector and correlator. A temporal coherence is automatically obtained due to the built-in zero OPD. The spatial modulation frequency, as well as the required sampling of the image change

with the separation of sub-apertures. The intensity in the focal plane can be written as follows:

$$\mathcal{I}(\mathbf{x}) = a(D.x) \left[\mathcal{I}_1 + \mathcal{I}_2 + 2\sqrt{\mathcal{I}_1 \mathcal{I}_2} \mid \boldsymbol{\gamma}_B(0) \mid cos \left\{ \frac{2\pi}{\lambda} \left(\frac{B.x}{f} + d \right) - \psi_B \right\} \right], (31)$$

where, B is the baseline, D the diameter of the sub-apertures, f the focal length, the envelope, $a(D.x)$ the image of each sub-apertures (Airy disk), ψ_B, the phase of $\gamma_B(0)$, $2\pi d/\lambda$, the incidental non-zero OPD between the fields, and d is the extra optical path in front of one aperture.

To overcome the restrictions of the baseline, Michelson (1920) constructed his stellar interferometer by installing a 7 m steel beam on top of the said 100 inch reflecting telescope at Mt. Wilson. It was equipped with 4 flat mirrors to fold the beams in periscopic fashion. Michelson and Pease (1921) were able to resolve the supergiant star, α Orionis, and a few other stars. In this design, the maximum resolution is limited by the length of the girder bearing the collectors. The spatial modulation frequency in the focal plane is independent of the distance between the collectors. This feature allows one to keep the same detection conditions when varying the baseline B. The telescope serves as correlator, thus, provides zero OPD. This experiment had faced various difficulties in resolving stars. These are mainly due to the (i) effect of atmospheric turbulence, (ii) variations of refractive index above small sub-apertures of the interferometer causing the interference pattern to move as a whole, (iii) 7 meter separation of outer mirrors is insufficient to measure the diameter of more stars, and (iv) mechanical instability prevents controlling the large interferometer.

3. Atmospheric turbulence

The turbulent phenomena associated with heat flow and winds in the atmosphere, causing the density of air fluctuating in space and time, occur predominantly due to the winds at various heights, convection in and around the building and the dome, any obstructed location near the ground, off the surface of the telescope structure, inside the primary mirror cell, etc. The cells of differing sizes and refractive indices produced by this phenomena, move rapidly across the path of the light, causing the distortion on the shape of the wave-front and variations on the intensity and phase. In what follows, the descriptions of the atmospheric turbulence theory, metrology of seeing (Coulman, 1985), observational results, mathematical details (Roddier, 1981, 1988a) etc., are enumerated.

3.1. Formation of eddies

Large scale temperature inhomogeneities caused by differential heating of different portions of the Earth's surface produce random micro-structures in the spatial distribution of temperature which, in turn, cause the random fluctuations in the refractive index of air. These large scale refractive index inhomogeneities are broken up by turbulent wind and convection, spreading the scale of the inhomogeneities to smaller sizes.

When the average velocity, v_a, of a viscous fluid of characteristic size, l, is gradually increased, two distinct states of fluid motion, viz., (i) laminar (regular and smooth in space and time), at very low, v_a, (ii) unstable and random fluid motion − turbulence − at $v_a >$ some critical value, are observed (Tatarski, 1967, Ishimaru, 1978). The dimensionless quantity, known as Reynolds number, $R_e = v_a l/\nu_v$, that characterizes a turbulent flow, is a function of the flow geometry, v_a, l, and kinematic viscosity of the fluid, ν_v. When R_e exceeds some value in a pipe (depending on its geometry), the transition of the flow from laminar to turbulent occurs. Between these two extreme conditions, the flow undergoes a series of unstable states. The atmosphere is difficult to study due to the high Reynolds number, of the order of 10^6, which ensures that atmospheric air flow is nearly always turbulent (Ishimaru, 1978).

According to the atmospheric turbulence model the energy enters the flow at low frequencies (Taylor, 1921, 1935, Richardson, 1922, Kolmogorov, 1941b, 1941c) with scale length, L_0, (outer scale length) and spatial frequency, $k_{L_0} = 2\pi/L_0$, as a direct result of the non-linearity of the Navier-Stokes equation governing fluid motion. L_0 varies according to the local conditions, ranging from 2 m (Nightingale and Busher, 1991) to 100 m. A value for L_0, which is more than 2 km is also reported in the literature (Colavita et al., 1987).

The refractive index of the atmosphere, $n(\mathbf{r}, \mathbf{t})[= n_0 + n_1(\mathbf{r}, \mathbf{t})$, where, $n_0 \approx 1$ is the mean refractive index of air, $n_1(\mathbf{r}, \mathbf{t})$, is the randomly fluctuating term, $\mathbf{r}$ is the 3-dimensional (3-d) position vector and t is the time], varies due to the temperature inhomogeneities. The dependence of the refractive index of air upon pressure, P (millibar) and temperature, T (Kelvin), at optical wavelengths is given by $n_1 \cong n-1 = 77.6 \times 10^{-6} P/T$ (Ishimaru, 1978). The packets of air that have a uniform refractive index, referred as turbulent eddies, affect the optical propagation. The statistical distribution of the size and number of these eddies is characterized by the power spectral density, $\Phi_n(\mathbf{k})$, of $n_1(\mathbf{r})$.

3.2. Inertial subrange and structure functions

When the scale length associated with these eddies decreases the Reynolds number to a very low value, where the kinetic energy of the flow is lost as heat via viscous dissipation resulting in a rapid drop in power spectral density, $\Phi_n(\mathbf{k})$, for $k > k_0$ (k_0 is critical wave number), imposes a highest possible spatial frequency on the flow; the break up of the turbulent eddies stops (Tatarski, 1967, 1968). This is denoted as inner scale length, l_0, and spatial frequency, $k_{l_0} = 2\pi/l_0$. l_0, varies from a few millimeter near the ground up to a centimeter (cm) high in the atmosphere. The value of inertial subrange, $l_0 < r < L_0$ ($\mathbf{r}$, is the vector between the two points of interest) would be different at various locations at the site. The 3-d power spectrum, Φ_n, for the wave number, $k > k_0$, (critical wave number), in the case of inertial subrange, can be equated as,

$$\Phi_n(\mathbf{k}) = 0.033 C_n^2 k^{-11/3}, \tag{32}$$

where, C_n^2 is known as structure constant of the refractive index fluctuations.

This spectrum for refractive index changes for a given structure constant and is valid within the inertial subrange, $(k_{L_0} < k < k_{l_0})$. This Kolmogorov-Obukhov model of turbulence, describing the power-law spectrum for the inertial intervals of wave numbers, is widely used for astronomical purposes (Tatarski 1993).

Owing to the non-integrable pole at $k = 0$, mathematical problems arise to use this equation for modeling the spectrum of the refractive index fluctuations when, $k \to 0$. To overcome this defect, von Kármán model is often used (Goodman, 1985). The structure functions of the refractive index and phase fluctuations are the main characteristics of the light propagation through the turbulent atmosphere, influencing the performance of the imaging system. The refractive index structure function, $\mathcal{D}_n(\mathbf{r})$, can be defined as,

$$\mathcal{D}_n(\mathbf{r}) = <|\, n\,(\boldsymbol{\rho} + \mathbf{r}) - n\,(\boldsymbol{\rho})\,|^2>, \qquad (33)$$

which expresses its variance at two points r_1, r_2.

The structure functions are related to the covariance function, $\mathcal{B}_n(\mathbf{r})$, through

$$\mathcal{D}_n(\mathbf{r}) = 2[\mathcal{B}_n(\mathbf{0}) - \mathcal{B}_n(\mathbf{r})], \qquad (34)$$

where, $\mathcal{B}_n(\mathbf{r}) = <\, n\,(\boldsymbol{\rho})\, n\,(\boldsymbol{\rho} + \mathbf{r})\, >$ and the covariance is the 3-d Fourier transform of the spectrum, $\Phi_n(\mathbf{k})$ (Roddier, 1981).

Kolmogorov (1941a) states that the structure function in the inertial range (homogeneous and isotropic random field) depends on $\mathbf{r} = |\,\mathbf{r}\,|$, as well as on the values of the rate of production or dissipation of turbulent energy ϵ_0 and the rate of production or dissipation of temperature inhomogeneities η_0. From the Tatarski (1967) approximation, the refractive index structure function can be written as,

$$\mathcal{D}_n(\mathbf{r}) = C_n^2 r^{2/3}. \qquad (35)$$

Similarly, the velocity structure function, $\mathcal{D}_v(\mathbf{r}) = C_v^2 r^{2/3}$, and temperature structure function, $\mathcal{D}_T(\mathbf{r}) = C_T^2 r^{2/3}$, can also be derived. The temperature structure constant, C_T^2, is proportional to the vertical temperature gradient but is not related to the velocity of the flow. Several experiments confirm this two-thirds power law in the atmosphere (Wyngaard et al., 1971, Coulman, 1969, 1974, Hartley et al., 1981, Walters and Kunkel, 1981, Lopez, 1991). The rms fluctuation in the difference between the refractive index at any two points in earth's atmosphere is often approximated as a power law of the separation between the points.

Seeing affects the measurements of fringe visibility with a long baseline optical amplitude interferometer (section 9.2), by introducing phase aberrations across the wave

$$\mathcal{R} = \int \mathcal{B}(\mathbf{u}) \cdot \mathcal{T}(\mathbf{u}) d\mathbf{u}. \tag{51}$$

It is limited either by the telescope or by the atmosphere, depending on the relative width of the two functions, $\mathcal{B}(\mathbf{u})$ and $\mathcal{T}(\mathbf{u})$. The diffraction-limited resolving power, $\mathcal{R}_D$, of a small telescope with an unobscured circular aperture of diameter, $D \ll r_0$, depends on its optical transfer function (Roddier, 1981);

$$\mathcal{R}_D = \int \mathcal{T}(\mathbf{u}) d\mathbf{u} = \frac{\pi}{4} \left(\frac{D}{\lambda}\right)^2 \tag{52}$$

The resolving power of a large telescope, $(D >> r_0)$ is dominated by the turbulence effects;

$$\mathcal{R}_\infty = \int \mathcal{B}(\mathbf{u}) d\mathbf{u}. \tag{53}$$

According to equation (47), $\mathcal{B}(\mathbf{u})$, can be expressed as,

$$\mathcal{B}(\mathbf{u}) = \mathcal{B}_0(\lambda \mathbf{u}) = e^{-\frac{1}{2}\left[2.91k^2(\lambda u)^{5/3}/cos\gamma \int C_n^2(z)dz\right]} \tag{54}$$

$$\mathcal{R}_\infty = (6\pi/5) \left[\frac{1}{2}\left(\frac{2.91k^2\lambda^{5/3}}{cos\gamma}\int C_n^2(z)dz\right)\right]^{-6/5} \Gamma(6/5). \tag{55}$$

Fried, (1966) had introduced the critical diameter r_0, for a telescope for which $\mathcal{R}_D = \mathcal{R}_\infty$. Therefore, placing $D = r_0$ in equation (52), the equation (44) takes the form as follows,

$$\mathcal{B}(\mathbf{u}) = e^{-3.44(\lambda u/r_0)^{5/3}} \tag{56}$$

$$\mathcal{B}_0(\boldsymbol{\xi}) = e^{-3.44(\xi/r_0)^{5/3}} \tag{57}$$

The expression for the phase structure function across the telescope aperture can be written as (see equation 40),

$$\mathcal{D}_\psi(\boldsymbol{\xi}) = 6.88 \left(\frac{\xi}{r_0}\right)^{5/3} \tag{58}$$

Several observers have confirmed this relationship (O'Byrne, 1988, Nightingale and Buscher, 1991). The resolving power of any large telescope (larger than r_0) is essentially limited by the size of the seeing disk, $1.22\lambda/r_0$. By replacing the value of $\mathcal{B}_0(\boldsymbol{\xi})$, in

value of $\mathcal{C}_n^2$ increases about 11 km over Paranal, Chile using Scidar and DIMM data. The turbulence concentrates into a thin layer of 100−200 m thickness where the value of $\mathcal{C}_n^2$ increases by more than an order of its background level. Orographic disturbances also play an important role, while the behaviour of the former is independent of the location (Barletti et al., 1976).

3.3. Wave propagation through the turbulent atmosphere

The random refractive index fluctuations deflect the rays of the light propagating down the turbulence of the atmosphere; the longer the path, more it suffers the deflection. The spatial correlational properties of the turbulence-induced field perturbations are evaluated by combining the basic turbulence theory with the stratification and phase screen approximations. The variance of the ray can be translated into a variance of the phase fluctuations. For calculating the same, Roddier (1981) used the correlation properties for propagation through a single (thin) turbulence layer and then extended procedure to account for many such layers. It is assumed that the refractive index fluctuations between the individual layers are statistically independent (Tatarski, 1967). Several investigators (Goodman, 1985, Troxel et al., 1994) have argued that individual layers can be treated as independent provided the separation of the layer centres is chosen large enough so that the fluctuations of the log amplitude and phase introduced by different layers are uncorrelated. The method set out by Roddier (1981) for the wave propagation through the atmosphere runs as follows.

Let a monochromatic plane wave of wavelength λ from a distant star at zenith, propagate towards the ground based observer; the complex amplitude at co-ordinate, $(\mathbf{x}, h)$, is given by,

$$\Psi_h(\mathbf{x}) = \mid \Psi_h(\mathbf{x}) \mid e^{i\psi_h(\mathbf{x})}. \tag{37}$$

Here, for height h, the average value of the phase, $< \psi_h(\mathbf{x}) > = 0$, and the unperturbed complex amplitude outside the atmosphere is normalized to unity $[\Psi_\infty(\mathbf{x}) = 1]$.

When this wave is allowed to pass through a thin layer of turbulent air of thickness δh_j, which is considered to be large compared to the scale of turbulent eddies but small enough for the phase screen approximation (diffraction effects is negligible over the distance, δh_j), the complex amplitude of the plane wave-front after passing through the layer can be expressed as,

$$\Psi_j(\mathbf{x}) = e^{i\psi_j(\mathbf{x})}. \tag{38}$$

Here, $\psi_j(\mathbf{x}) \left[= k \int_{h_j}^{h_j+\delta h_j} n(\mathbf{x}, z) dz\right]$ is the phase-shift introduced by the refractive index fluctuations, n(x,h) inside the layer, $k = 2\pi/\lambda$ is the wave number of the vibration. In this case, the rest of the atmosphere is thought to be calm and homogeneous.

The coherence function of the complex amplitude, $< \Psi_j(\mathbf{x})\Psi_j^*(\mathbf{x}+\boldsymbol{\xi}) >$, at the layer output leads to

$$\mathcal{B}_j(\boldsymbol{\xi}) = < e^{i\left[\psi_j(\mathbf{x})-\psi_j(\mathbf{x}+\boldsymbol{\xi})\right]} > . \tag{39}$$

The quantity $\psi_j(\mathbf{x})$ can be considered to be the sum of a large number of independent variables, and therefore, have Gaussian statistics. Roddier (1981) points out that the expression in square brackets is Gaussian too with zero mean. He finds the similarity of this equation to Fourier transform of the probability density function at unit frequency, therefore;

$$\mathcal{B}_j(\boldsymbol{\xi}) = e^{-\frac{1}{2}\mathcal{D}_{\psi_j}(\boldsymbol{\xi})}, \tag{40}$$

where, $\mathcal{D}_{\psi_j}(\boldsymbol{\xi})\left[=<\mid\psi_j(\mathbf{x})-\psi_j(\mathbf{x}+\boldsymbol{\xi})\mid^2>\right]$, is the 2-d structure function of the phase, $\psi_j(\mathbf{x})$.

Let the covariance of the phase be defined as $\mathcal{B}_{\psi_j}(\boldsymbol{\xi}) = < \psi_j(\mathbf{x})\psi_j(\mathbf{x}+\boldsymbol{\xi}) >$, and by replacing $\psi_j(\mathbf{x})$,

$$\mathcal{B}_{\psi_j}(\boldsymbol{\xi}) = k^2 \int_{h_j}^{h_j+\delta h_j} dz \int_{h_j-x}^{h_j+\delta h_j-x} \mathcal{B}_n(\boldsymbol{\xi},\zeta)\,d\zeta, \tag{41}$$

where, $\mathcal{B}_n(\boldsymbol{\xi},\zeta) = < n(\mathbf{x},z)n(\mathbf{x}+\boldsymbol{\xi},z') >$ is the 3-d refractive index covariance and $\zeta = z'-z$.

Since the thickness of the layer, δh_j, is large compared to the correlation scale of the turbulence, the integration over ζ from $-\infty$ to $+\infty$, leads to

$$\mathcal{B}_{\psi_j}(\boldsymbol{\xi}) = k^2\delta h_j \int \mathcal{B}_n(\boldsymbol{\xi},\zeta)\,d\zeta. \tag{42}$$

The phase structure function is related to its covariance (equation 34), and therefore,

$$\mathcal{D}_{\psi_j}(\boldsymbol{\xi}) = 2k^2\delta h_j \int [\mathcal{B}_n(\mathbf{0},\zeta) - \mathcal{B}_n(\boldsymbol{\xi},\zeta)]\,d\zeta. \tag{43}$$

The refractive index structure function defined in equation (35) can be evaluated as, $\mathcal{D}_n(\boldsymbol{\xi},\zeta) = \mathcal{C}_n^2\left(\xi^2+\zeta^2\right)^{1/3}$, and recalling equation (34), equation (43) can be integrated and yields,

$$\mathcal{D}_{\psi_j}(\boldsymbol{\xi}) = 2.91k^2\mathcal{C}_n^2\xi^{5/3}\delta h_j. \tag{44}$$

The covariance of the phase can be obtained by substituting equation (44), in equation (40),

$$\mathcal{B}_{h_j}(\boldsymbol{\xi}) = e^{-\frac{1}{2}\left(2.91k^2C_n^2\xi^{5/3}\delta h_j\right)}. \tag{45}$$

Using Fresnel approximation, Roddier (1981) enunciates that the covariance of the phase at the ground level due to a thin layer of turbulence at some height off the ground, $\mathcal{B}_0(\boldsymbol{\xi}) = \mathcal{B}_{h_j}(\boldsymbol{\xi})$. For high altitude layers the complex field will fluctuate both in phase and in amplitude, and therefore, the wave structure function, $\mathcal{D}_{\psi_j}(\boldsymbol{\xi})$, is not strictly true as the ground level. The turbulent layer acts like a diffracting screen; however, correction in the condition of astronomical observation remains small (Roddier, 1981).

The wave structure function after passing through N layers can be expressed as the sum of the N wave structure functions associated with the individual layers, For each layer, the coherence function is multiplied by the term, $e^{-\frac{1}{2}\left[2.91k^2C_n^2(h_j)\xi^{5/3}\delta h_j\right]}$; therefore, the coherence function at ground level is given by

$$\mathcal{B}_0(\boldsymbol{\xi}) = \prod_{j=1}^{N} e^{-\frac{1}{2}\left[2.91k^2C_n^2(h_j)\xi^{5/3}\delta h_j\right]} = e^{-\frac{1}{2}\left[2.91k^2\xi^{5/3}\sum_{j=1}^{N}C_n^2(h_j)\delta h_j\right]}. \tag{46}$$

This expression can be generalized for a star at an angular distance γ away from the zenith viewed through all over the turbulent atmosphere,

$$\mathcal{B}_0(\boldsymbol{\xi}) = e^{-\frac{1}{2}\left[2.91k^2\xi^{5/3}/cos\gamma\int C_n^2(z)dz\right]}. \tag{47}$$

3.4. Fried's parameter (r_0)

When a plane wave-front passes down through refractive index inhomogeneities, it suffers phase fluctuations and reaches the entrance pupil of a telescope with patches of random excursions in phase (Fried, 1966). Each patch of the wave-front with diameter, r_0, known as Fried's Parameter (atmospheric coherence diameter), would act independently of the rest of the wave-front.

Let the modulation transfer function (MTF) of an optical system be composed of the atmosphere and a telescope. The long-exposure PSF is defined by the ensemble average, $< \mathcal{S}(\mathbf{x}) >$, which is independent of the direction. Figure 3 depicts the plane-wave propagation through multiple turbulent layers. If the object emits incoherently, the average illumination, $\mathcal{I}(\mathbf{x})$, of a resolved object, $\mathcal{O}(\mathbf{x})$, obeys the convolution relationship,

$$< \mathcal{I}(\mathbf{x}) >= \mathcal{O}(\mathbf{x}) * < \mathcal{S}(\mathbf{x}) > . \tag{48}$$
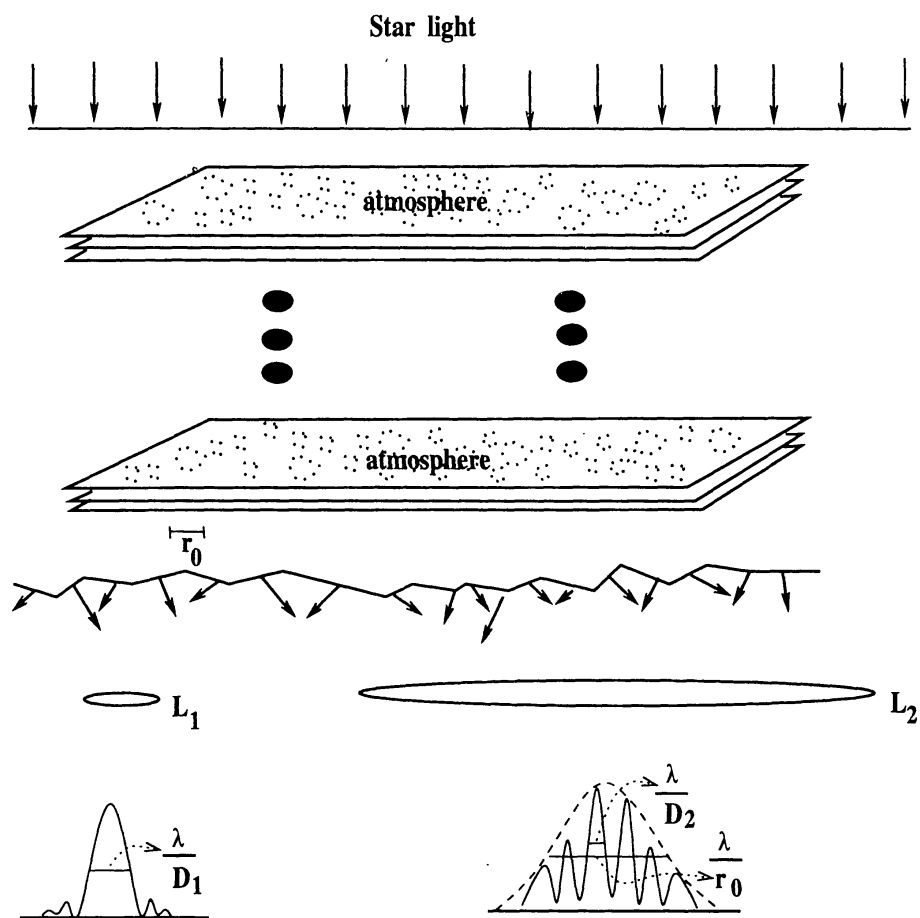
S. K. Saha

Star light

Figure 3. Plane-wave propagation through the multiple turbulent layers.

Using 2-d Fourier transform, the above equation can be written,

$$< \widehat{\mathcal{I}}(\mathbf{u}) >= \widehat{\mathcal{O}}(\mathbf{u}) \cdot < \widehat{\mathcal{S}}(\mathbf{u}) >, \tag{49}$$

where, $< \widehat{\mathcal{S}}(\mathbf{u}) >$ denotes the transfer function for long-exposure images, $\mathbf{u}$, the spatial frequency vector with magnitude, u and $\widehat{\mathcal{O}}(\mathbf{u})$ the object spectrum.

The transfer function is the product of the atmosphere transfer function (wave coherence function), $B(\mathbf{u})$, and the telescope transfer function, $T(\mathbf{u})$,

$$< \widehat{\mathcal{S}}(\mathbf{u}) >= \mathcal{B}(\mathbf{u}) \cdot \mathcal{T}(\mathbf{u}). \tag{50}$$

For a long-exposure through the atmosphere, the resolving power, $\mathcal{R}$, of any optical telescope, is expressed as,

fronts incident on the interferometer, therefore, the relative phase of the wave fronts at the apertures changes with time, as well as varies the optical paths through the two arms. Venkatakrishnan and Chatterjee, (1987) pointed out that the afore-mentioned power law is not valid for large separations. The rms fluctuation tends to a constant for large separations which reduces the random excursions of fringes in an interferometer from the value expected from the power law. In turn, this pushes the observing limits to fainter magnitudes. Venkatakrishnan, (1987) applied this idea to the question of astronomical seeing. It was shown that the correct statistical behaviour at large separations predicts a lower value for seeing than that expected from a power law behaviour. Davis and Tango, (1996) have developed a method for measuring the atmospheric coherence time that can be carried out in parallel with the determination of the fringe visibility in an amplitude interferometer. The measured coherence time was found to be ranged between ~ 1 to ~ 7 ms.

Since the fluctuations in the air refractive index are proportional to the temperature fluctuations, the refractive index structure constant can be related by the following equation (Roddier, 1988a),

$$\mathcal{C}_n = 75 \times 10^{-6} \frac{P}{T^2} \mathcal{C}_T. \tag{36}$$

The value of the $\mathcal{C}_n^2$ depends on both local conditions, as well as on the planetary boundary layer. The significant scale lengths, in the case of former, depend on the local objects and the primary effect is to change the inertial subrange, as well as to introduce temperature differentials. While the latter can be generalized as: (i) surface boundary layer due to the ground convection, extending up to a few kilometer (km) height of the atmosphere, where shear is the dominant source of turbulence (scale lengths are roughly constant and $\mathcal{C}_T^2 \propto z^{-2/3}$), (ii) the free convection layer associated with orographic disturbances, where the scale lengths are height dependent, ($\mathcal{C}_T^2 \propto z^{-4/3}$) and (iii) in the tropopause and above, where the turbulence is due to the wind shear and the temperature gradient vanishes slowly. The values of $\mathcal{C}_T^2$ have been measured by various techniques, viz., micro-thermal studies, radar and acoustic soundings, balloon and aircraft experiments (Coulman, 1969, 1974, Tsvang, 1969, Lawrence et al., 1970, Kallistratova and Timanovskiy, 1971, Ochs and Lawrence, 1972, Metcalk, 1975)

The turbulence which reaches a minimum just after the sunrise and steeply increases until afternoon, is primarily due to the solar heating of the ground (Hess, 1959). It decreases to a secondary minimum after sunset and slightly increases during night. The typical values of $\mathcal{C}_n^2$, 12 m above the ground, during the daytime is found to be $10^{-13} \, m^{-2/3}$ and $10^{-14} \, m^{-2/3}$, during night time (Kallistratova and Timanovskiy, 1971). These values are height-dependent; (i) $h^{-4/3}$, under unstable daytime conditions, (ii) $h^{-2/3}$, under neutral conditions, (iii) a slow decrease under stable condition, say during night time (Wyngaard et al., 1971). It reaches a minimum value of the order of $10^{-17} \, m^{-2/3}$ around 6−9 km with slight increase to a secondary maximum near the tropopause and decreases further in the stratosphere (Roddier, 1981). Masciadri et al., (1999) have noticed the

equation (47), an expression for r_0 in terms of the distribution of the turbulence in the atmosphere can be derived.

$$r_0 = \left[0.423 \frac{k^2}{cos\gamma} \int C_n^2(z)dz \right]^{-3/5}. \tag{59}$$

Computer simulations by Venkatakrishnan et al., (1989), demonstrated the destructions of the finer details of an image of a star by the atmospheric turbulence.

3.4.1. Benefit of short-exposure images

In the long-exposure images, the image is spread during the exposure by its random variations of the tilt. The image sharpness and the MTF are affected by the wave-front tilt, as well as by the more complex shapes, while in the case of a short-exposure image, the image sharpness and MTF are insensitive to the tilt. The random factor associated with the tilt is extracted from the MTF before taking the average, where in the long-exposure case, no such factor is removed (section 3.4).

Let the two seeing cells be separated by a vector $\lambda\mathbf{u}$, in the telescope pupil. If a point source is imaged through the telescope by using pupil function consisting of two apertures (θ_1, θ_2), corresponding to the two seeing cells, then a fringe pattern is produced with narrow spatial frequency bandwidth. Each sub-aperture is small enough for the field to be coherent over its extent. Any stellar object is too small to be resolved through a single sub-aperture. Atmospheric turbulence does not affect the amplitude of the fringes produced, but introduces phase delays, which, in turn, shift the fringe pattern randomly and blur the fringe pattern during long-exposure.

The major component $\widehat{\mathcal{I}}(\mathbf{u})$, at the frequency, $\mathbf{u}$, is produced by contributions from all pairs of points with separations $\lambda\mathbf{u}$, with one point in each aperture. If the major component is averaged over many frames, the resultant for frequencies greater than r_0/λ, tends to zero since the phase-difference, $\theta_1 - \theta_2$; mod 2π, between the two apertures is distributed uniformly between $\pm\pi$, with two mean. The Fourier component performs a random walk in the complex plane and averages to zero:

$$< \widehat{\mathcal{I}}(\mathbf{u}) >= 0, \quad u > r_0/\lambda. \tag{60}$$

The argument of equation (49) is expressed as,

$$arg \mid \widehat{\mathcal{I}}(\mathbf{u}) \mid = \psi(\mathbf{u}) + \theta_1 - \theta_2, \tag{61}$$

where, $\psi(\mathbf{u})$ is the Fourier phase at $\mathbf{u}$, and $arg \mid\mid$ stands for, 'the phase of'.

While in the case of autocorrelation technique, the autocorrelation of $\mathcal{I}(\mathbf{x})$ is the correlation of $\mathcal{I}(\mathbf{x})$ and $\mathcal{I}(\mathbf{x})$ multiplied by the complex exponential factor with zero spatial frequency. The major Fourier component of the fringe pattern is averaged as a product with its complex conjugate and so the atmospheric phase contribution is eliminated and the averaged signal is non-zero. Therefore, the resulting representation in the Fourier space is,

$$< \widehat{\mathcal{I}}^A(\mathbf{u}) >=< \widehat{\mathcal{I}}(\mathbf{u})\widehat{\mathcal{I}}^*(\mathbf{u}) >=<| \widehat{\mathcal{I}}(\mathbf{u}) |^2 >\neq 0. \tag{62}$$

The argument of this equation is given by the expression,

$$arg \mid \widehat{\mathcal{I}}(\mathbf{u})\widehat{\mathcal{I}}(-\mathbf{u}) \mid = \theta^A(\mathbf{u}) = \psi(\mathbf{u}) + \theta_1 - \theta_2 + \psi(-\mathbf{u}) - \theta_1 + \theta_2 = 0. \tag{63}$$

For a large telescope, the aperture, $\mathcal{P}$, can be sub-divided into a set of sub-apertures, p_j. Each pair of them, p_n, p_m, separated by a distance (baseline) B would form fringes. The intensity in the focal plane of the telescope, $\mathcal{I}$, according to the diffraction theory (Born and Wolf, 1984), is given by the expression,

$$\mathcal{I} = \sum_{n,m} < \Psi_n \Psi_m^* > \tag{64}$$

The term, $\Psi_n \Psi_m^*$, is multiplied by $e^{i\psi}$, where, ψ is the random instantaneous shift in the fringe pattern. With increasing distance between the two sub-apertures, the fringes move with an increasingly larger amplitude. On a long-exposure image no shift is observed, which implies the loss of the high frequency components of the image. If the integration time is shorter (< 20 ms) than the evolution time of the phase inhomogeneities, the interference fringes are preserved but their phases are randomly distorted. This produces the speckle pattern observed in short-exposure images. These speckles can occur randomly along any direction within an angular patch of diameter, λ/r_0. The sum of several statistically uncorrelated speckle patterns from a point source can result in an uniform patch of light a few arcseconds wide (conventional image).

3.4.2. Measurement of r_0

Measurement of r_0 is of paramount importance to estimate the seeing at any astronomical site. Systematic studies of this parameter would help in understanding the various causes of the local seeing. Various methods of measuring r_0 have been discussed in the literature (Von der Lühe, 1984, Wood, 1985, Roddier, 1988a, Vernin et al., 1991). Using Fizeau mask interferometer with two apertures, the atmospheric transfer function can be estimated by measuring the coherence function, $\mathcal{B}(\mathbf{u})$. The intensity of the star light at telescope focus is,
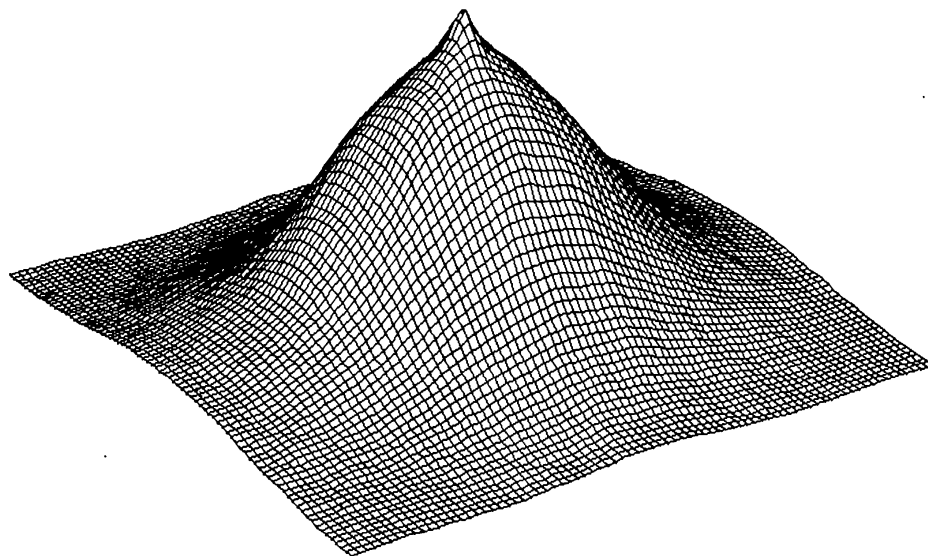
S. K. Saha

HR2305a1

Figure 4. 3-d picture of the autocorrelation of HR2305 observed at at 2.34 m VBT, Kavalur, India, on 28th March, 1991, 1510 hr. UT (Saha and Chinnappan, 1999).

$$\mathcal{I} = \mid \Psi(\mathbf{x}) \mid^2 + \mid \Psi(\mathbf{x} + \lambda\mathbf{u}) \mid^2 + 2\Re[\Psi(\mathbf{x})\Psi^*(\mathbf{x} + \lambda\mathbf{u})]. \tag{65}$$

The amplitude of the long-exposure fringes is proportional to $< \Psi(\mathbf{x})\Psi^*(\mathbf{x}+\lambda\mathbf{u}) >$, and therefore, provides the measurement of $\mathcal{B}(\mathbf{u})$. Rotational shear interferometers (Roddier and Roddier, 1988) can be used to determine the coherence of the source by using a short integration time.

Another qualitative method is that based on from the short-exposure images using speckle interferometric technique (Labeyrie, 1970). In this, the area of the telescope aperture divided by the estimated number of speckles gives the wave-front coherence area σ, from which r_0 can be found by using relation,

$$\sigma = 0.342\left(\frac{r_0}{\lambda}\right)^2. \tag{66}$$

The averaged autocorrelation of the these images contains both the autocorrelations of the seeing disk, as well as of the mean speckle cell. It is the width of the speckle component of the autocorrelation that provides the information on the size of the object being

observed (Saha and Chinnappan, 1999, Saha et al., 1999a). The form of transfer function, $<| \widehat{\mathcal{S}}(\mathbf{u}) |^2>$, can be obtained by calculating Wiener spectrum of the instantaneous intensity distribution from a point source (section 6). Figure 4 depicts the autocorrelation of HR2305 observed at 1510 hrs UT, obtained at the Cassegrain focus of 2.34 m VBT, Kavalur, India.

3.4.3. Seeing at the telescope site

The term 'seeing' is the total effect of distortion in the path of the star light via different contributing layers of the atmosphere (see section 3.2) to the detector placed at the focus of the telescope. Though the effect of the different layer turbulence has been receiving attention to identify the best site, the major sources of image degradation predominantly comes from the thermal and aero-dynamic disturbances in the atmosphere surrounding the telescope and its enclosure, viz., (i) thermal distortion of primary and secondary mirrors when they get heated up, (ii) dissipation of heat by the secondary mirror (Zago, 1995), (iii) rise in temperature at the primary cell, and (iv) at the focal point causing temperature gradient close to the detector etc. The aberrations in the design, manufacture and alignment of the optical train also add to this degradation.

Various corrective measures, viz., (i) insulating the surface of the floors and walls, (ii) introducing active cooling system to eliminate the heat produced by electric equipments on the telescope and elsewhere in the dome, (iii) installing ventilator to generate a sucking effect through the slit to counteract the upward action of the bubbles (Racine, 1984, Ryan and Wood, 1995), and (iv) maintaining a uniform temperature in and around the primary mirror of the telescope (Saha and Chinnappan, 1999) have been proposed to improve the seeing at the telescope site.

Mirror seeing is an important source of image spread and has the longest time-constant, of the order of several hours depending on the size and thickness of the mirror, for equilibrating with the ambient temperature (Woolf and Cheng, 1988). The spread amounts to 0.5″ for a 1° difference in temperature. The production of mirror seeing takes place very close to its surface, $\sim$ 2 cm above (Harding et al., 1979, Lowne, 1979, Zago, 1995 and references therein). The free convection above the mirror depends on the excess temperature of its surface above the ambient temperature with an exponent of 1.2. Iye et al., (1991) opined that a temperature difference of $< 1°$ C should be maintained between the mirror and its ambient. The mirror seeing becomes weak and negligible if the mirror can be kept at a 1° lower temperature than the surrounding air (Iye et al., 1992). While, Racine et al., (1991) found that mirror seeing sets in as soon as the mirror is measurably warmer than the ambient air and is quite significant if it is warmer by 1°. Gillingham (1984a, 1984b) reported that the ventilation of the primary mirror of the 3.9 m Anglo-Australian telescope (AAT) was found to improve the seeing when the mirror is warmer than the ambient dome air, and degrade the seeing when mirror is cooler than the latter (Barr et al., 1990).

On the other hand, a $4-5°\,C$ difference in temperature between the outside and inside of the dome causes a seeing degradation amounting to $0.5''$ only (Racine et al., 1991). The reported improvement of seeing at the 3.6 m Canada-France-Hawaii telescope (CFHT), Mauna-Kea, Hawaii, is largely due to the implementation of the floor chilling system to damp the natural convection, which essentially keeps the temperature of the primary mirror closer to the air volume (Zago, 1995). Saha and Chinnappan (1999) have measured the night-time variation of Fried's parameter, as obtained at the Cassegrain focus of the VBT, Kavalur, India, using the speckle interferometer. It is found that average observed r_0 is higher during the later part of the night than the earlier part, implying that the PSF has a smaller FWHM during the former period. This might indicate that the slowly cooling mirror creates thermal instabilities that decreases slowly over the night (Saha and Chinnappan, 1999).

4. Single aperture interferometry

Labeyrie (1970) identified the short-exposure turbulence degraded images as speckles and suggested an interferometric technique − speckle interferometry − to retrieve diffraction-limited informations of a stellar object using a large telescope. Ever since the development of this technique, it is widely used both in the visible, as well as in the infrared (IR) bands. With the photon counting detectors, it is able to record speckles of faint stellar objects up to the visual magnitude $m_v \approx 16$. In what follows, the stellar speckle interferometry and related techniques are elucidated.

4.1. Speckle interferometry

The term, 'Speckle', refers to the grainy structure observed when an uneven surface of an object is illuminated by a fairly coherent source. The formation of speckles results from the summation of coherent vibrations having different random characteristics. The statistical properties of speckle pattern − the summation of many sine functions having different random characteristics − depend both on the coherence of the incident light and the random properties of medium. Since the positive and negative values cannot cancel out everywhere, adding an infinite number of such sine functions would result in a function with 100% constructed oscillations (Labeyrie, 1985).

Depending on the randomness of the source, spatial or temporal, speckles tend to appear (Labeyrie, 1985). Spatial speckles may be observed when all parts of the source vibrate at same constant frequency but with different amplitude and phase, while temporal speckles are produced if all parts of it have uniform amplitude and phase. With a heterochromatic vibration spectrum, in the case of random sources of light, spatio-temporal speckles are produced. The speckle size is of the same order of magnitude as the Airy disc of the telescope in the absence of turbulence. The number of correlation cells is determined by the equation, $N = D/r_0$ and the number of photons per speckle is independent of telescope diameter (Dainty, 1975).

Speckle interferometry is a method to estimate the modulus of the Fourier transform from a set of short-exposure specklegrams of the object of interest. A specklegram represents the resultant of diffraction-limited incoherent imaging of the object irradiance, $\mathcal{O}(\mathbf{x})$, convolved with the function representing the combined effects of the turbulent atmosphere and the image forming optical system, $\mathcal{S}(\mathbf{x})$. This is averaged over the duration of the short, narrow bandpass exposure. An ensemble of such specklegrams, $\mathcal{I}_k(\mathbf{x}), k = t_1, t_2, t_3, \ldots, t_M$, constitute an astronomical speckle observation. The transfer function of $\mathcal{S}(\mathbf{x})$, can be estimated by calculating Wiener spectrum of the instantaneous intensity from the unresolved star. The size of the data sets is constrained by the consideration of the signal-to-noise (S/N) ratio. Integration time of each exposure varies from a few milliseconds to twenty milliseconds, depending on the condition of seeing, to freeze the single realization of the turbulence. Usually specklegrams of the brightest possible reference star are recorded to ensure that the S/N ratio of reference star is much higher than the S/N ratio of the programme star.

4.1.1. Speckle interferometer

A speckle interferometer is a high quality diffraction-limited camera where magnified ($\sim$ f/100) short-exposure images can be recorded. To compensate for the atmospherically induced dispersion at zenith angles larger than a few degrees, counter-rotating computer controlled dispersion correcting prisms are used in many conventional speckle cameras. The observation can also be carried out using a narrow bandwidth filter (Saha et al., 1997a) without using the correcting process. Instead of interchangeable filters, a concave grating was used by Labeyrie (1974) to provide the necessary filtering in a tunable way. In this system, the object spectrum is displayed by a video monitor when adjusting the wavelength and bandwidth selection decker. The spectral features of interest is isolated down to 1 nm bandwidth. Subsequently, the system has been modified by replacing the concave grating with a concave holographic grating providing a four-channel facility (Foy, 1988). Labeyrie (1988) suggested for development of an interferometer with more spectral channels with narrow bandwidth down to 0.03 nm using a large spectrograph, facilitating the tuning of the desired wavelength in real time simultaneously.

An exceptionally rigid camera system has been developed by Saha et al., (1997a, 1999a) for the 2.34 m telescope, VBO, Kavalur, India. In this set up, the wave-front falls on the focal plane of an optical flat made of low expansion glass with a high precision hole of aperture, ($\sim$ 350 μm), at an angle of 15°, on its surface (Saha et al., 1997a). The image of the object passes on to a microscope objective through this aperture, which slows down the image scale of the telescope to f/130. A narrow band filter is set before the detector (cooled intensified-CCD) to avoid the chromatic blurring. The surrounding star field gets reflected from the optical flat on to a plane mirror and is re-imaged on an uncooled ICCD for guiding the object remotely. Figure 5 shows an overview of the speckle interferometer for VBT. In this set-up, the design analysis has been carried out with the modern finite element method (Zienkiewicz, 1967) and computer controlled machines were used in manufacturing to get the required dimensional and geometrical accuracies. Another versatile speckle interferometer has been developed by Prieur et al.,

(1998) recently for use at the 2 m Bernard Lyot Telescope, Pic du Midi Observatory. It provides the facilities of setting in various operating modes, such as, full pupil imaging, masked-pupil speckle imaging and aperture synthesis, spectroscopy, wave front sensor, stellar coronography. The system is in operation at the said telescope (Carbillet et al., 1996, Aristidi et al., 1997, 1999).
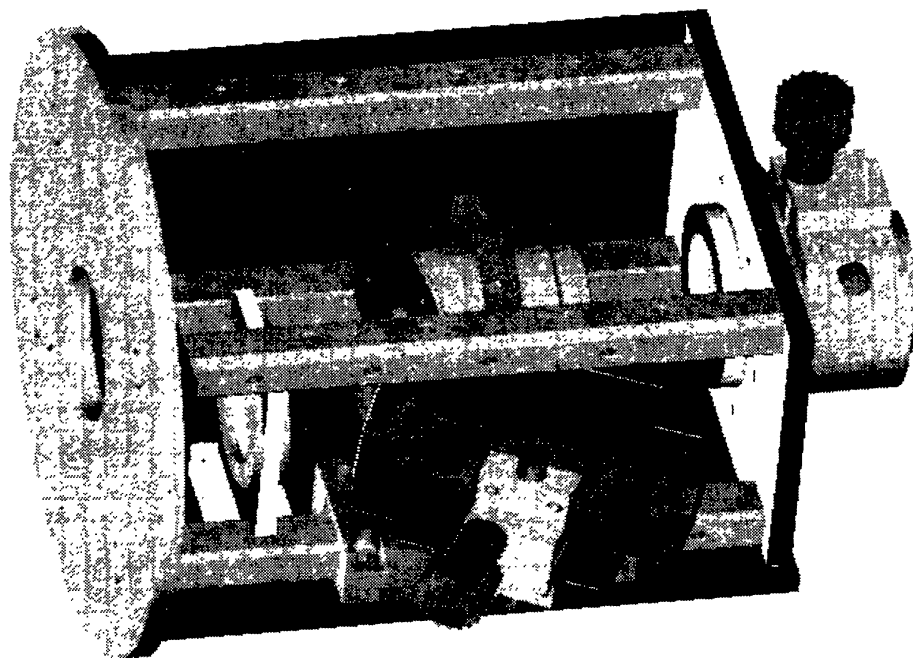

Figure 5. Overview of the speckle interferometer (Saha et al., 1997a, 1999a).

4.1.2. Estimation of Fourier modulus

The post-imaging process of speckle imaging technique are to obtain the spatial auto-correlation of the objects at low light levels. The intensity distribution, $\mathcal{I}(\mathbf{x})$, of the specklegrams, in the case of quasi-monochromatic incoherent source, is described by the space-invariant imaging equations. Let the imaging system be composed of a simple lens based telescope in which the PSF is invariant to spatial shifts. An object at a point, $\mathcal{O}(\mathbf{x}')$, anywhere in the field of view will, therefore, produce a pattern, $\mathcal{S}(\mathbf{x} - \mathbf{x}')$, across the image,

$$\mathcal{I}(\mathbf{x}) = \int \mathcal{O}(\mathbf{x}')\mathcal{S}(\mathbf{x} - \mathbf{x}')d\mathbf{x}'. \tag{67}$$

This equation can be translated into a convolution product,

$$\mathcal{I}(\mathbf{x}) = \mathcal{O}(\mathbf{x}) * \mathcal{S}(\mathbf{x}).\tag{68}$$

The Fourier space relationship between object and the image is

$$\widehat{\mathcal{I}}(\mathbf{u}) = \widehat{\mathcal{O}}(\mathbf{u}) \cdot \widehat{\mathcal{S}}(\mathbf{u}).\tag{69}$$

Taking the modulus square of the expression and averaging over many frames, the average image power spectrum is,

$$<\mid \widehat{\mathcal{I}}(\mathbf{u}) \mid^2>=\mid \widehat{\mathcal{O}}(\mathbf{u}) \mid^2 \cdot <\mid \widehat{\mathcal{S}}(\mathbf{u}) \mid^2> .\tag{70}$$

Since $\mid \widehat{\mathcal{S}}(\mathbf{u}) \mid^2$ is a random function in which the detail is continuously changing, its ensemble average becomes smoother. This form of transfer function can be obtained by calculating Wiener spectrum of the instantaneous intensity distribution from the reference star (unresolved star). The object is reconstructed from the power spectrum of the image knowing the PSF power spectrum and the true object autocorrelation is then obtained by Fourier inversion.

Reconstruction of object autocorrelation in case of the components in a group of stars retrieves the separation, position angle with a 180° ambiguity, and the relative magnitude difference. Saha and Venkatakrishnan, (1997), found the usefulness of the autocorrelation technique in obtaining the prior information on the object for certain applications of the image processing algorithms.

Most of the results obtained in the interferometric measurements of close binary stars are obtained from this technique (McAlister et al., 1987, 1989, 1990). Later Bagnuolo et al., (1992) have developed a PC-based 'directed vector· autocorrelation' (DVA) to eliminate the 180° ambiguity. It is found to be effective in determining the duplicity of the star, as well as in measuring its Cartesian coordinates (McAlister et al., 1993, Hartkopf et al., 1997a, 1997b). Saha et al., (1999d) developed an IRAF-based autocorrelation algorithm, where a Wiener parameter is added to PSF power spectrum in order to avoid zeros in the PSF power spectrum. This Wiener parameter is chosen according to the S/N ratio of image power spectrum. The notable advantage of this method is that the object can be reconstructed with a few frames. However, the phase ambiguities still remain.

The group at Observatoire de la Cote d'Azur, France, has developed a digital correlator for on-line data reduction (Blazit et al., 1977a) which is used for double star measurements (Bonneau and Foy, 1980, Bonneau et al., 1980, 1986, Blazit et al., 1987). Singh (1999) has developed a system for on-line data processing by optical / hybrid means using the correlation techniques. This system is used, at present for the reduction of laboratory speckles.

4.1.3. Difficulties in data processing

In general, the specklegrams have additive noise contamination, $\mathcal{N}_j(\mathbf{x})$, which includes all additive measurement of uncertainties. This may be in the form of (i) photon statistics noise, and (ii) all distortions from the idealized iso-planatic model represented by the convolution of $\mathcal{O}(\mathbf{x})$ with $\mathcal{S}(\mathbf{x})$ that includes non-linear geometrical distortions (Christou, 1988).

The quality of the image degrades (Foy, 1988) due to the following reasons: (i) variations of air mass or of its time average between the object and the reference, (ii) seeing differences between the MTF for the object and its estimation from the reference, (iii) deformation of mirrors or to a slight misalignment while changing its pointing direction, (iv) bad focusing, (v) thermal effect from the telescope etc. These may lead to a dangerous artifact, yielding a wrong identification of the companion star.

To estimate the MTF, it is necessary to calibrate it on a unresolved star for which all observing conditions are required to be identical to those for the object. Such a comparison is likely to introduce deviation in the statistics of speckles from the expected model based on the physics of the atmosphere. This, in turn, would result either in the suppression or in the enhancement of intermediate spatial frequencies which would also lead to artifacts (Foy, 1988). It is essential to choose the point source calibrator as close as possible, preferably within 1° of the programme star; the object and calibrator observations should be interleaved to calibrate for changing seeing condition by shifting the telescope back and forth during the observing run to equalize seeing distributions for both target and reference.

Another difficulty arises from using the frame transfer CCD as detector. It is subjected to limitations in detecting fast photon-event pairs. A pair of photons closer than a minimum separation cannot be detected as a pair by the afore-mentioned sensor. This yields a loss in HF information which, in turn, produces a hole in the centre of the autocorrelation, known as Centreur hole (Foy, 1988), resulting the degradation of the power spectra or bispectra (section 6.4) of short exposures images. This requires to be corrected (Thiébaut, 1994, Berio et al., 1998).

4.2. Speckle spectroscopy

The application of speckle interferometric technique to speckle spectroscopic observations enables to obtain spectral resolution with high spatial resolution of astronomical objects simultaneously. Labeyrie (1980) enunciated the importance of combining angular and spectral resolution for long baseline optical interferometry. Information is concentrated in narrow spectral intervals in astrophysics and can be obtained from narrow band stellar observations.

There are various types of speckle spectrograph. viz., (i) objective speckle spectrograph (slitless) that yields objective prism spectra with the bandwidth spanning from

400 nm − 800 nm (Kuwamura et al., 1992), (ii) wide-band projection speckle spectrograph that yields spectrally dispersed 1-dimensional (1-d) projection of the object (Grieger et al., 1988), (iii) slit speckle spectrograph, where the width of the slit is comparable to the size of the speckle (Beckers et al., 1983) have been developed. A prism or a grism can be used to disperse 1-d specklegrams. In the case of projection spectrograph, the projection of 2-d specklegrams is carried out by a pair of cylindrical lenses and the spectral dispersion is done by a spectrograph (Grieger and Weigelt, 1992). Weigelt et al., (1992) suggested that an image slicer consisting of K slits can also be used for the slit spectrograph.

Baba et al., (1994a) have developed an imaging spectrometer where a reflection grating acts as disperser. Two synchronized detectors record the dispersed speckle pattern and the specklegrams of the object. They have obtained stellar spectra of a few stars with the diffraction-limited spatial resolution of the 1.88 m telescope, Okayama Astrophysical Observatory by referring to the latter that are recorded simultaneously with dispersed speckle patterns. Another imaging spectrometer (see section 4.1.1) has been developed recently by Prieur et al., (1998) facilitating the conversion to a spectrograph by selecting the grism and a slit in the entrance image plane. It provides a low dispersion spectrographic mode with spectral range of 350-500 nm and a spectral resolution of ~0.7″. Figure 6 depicts the concept of a speckle spectroscopic camera.
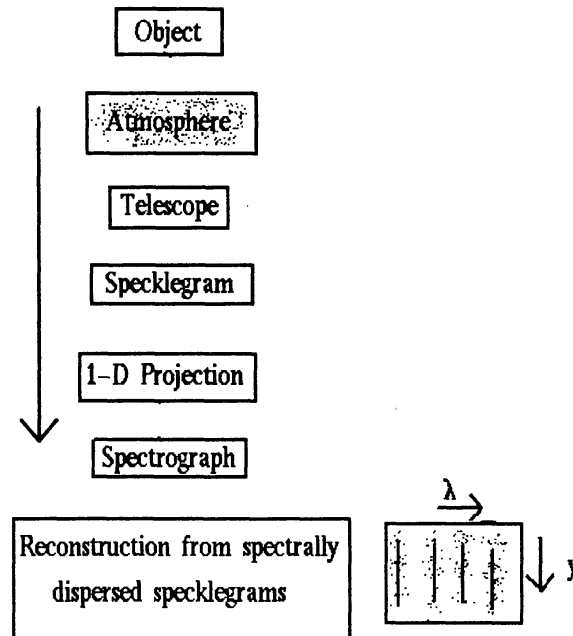

Figure 6. Concept of a speckle spectrograph.

Mathematically, the intensity distribution, $\mathcal{W}(\mathbf{x})$, of an instantaneous objective prism speckle spectrogram can be derived as,

$$\mathcal{W}(\mathbf{x}) = \sum_m \mathcal{O}_m(\mathbf{x} - \mathbf{x}_m) * \mathcal{G}_m(\mathbf{x}) * \mathcal{S}(\mathbf{x}), \tag{71}$$

where, $\mathcal{O}_m(\mathbf{x} - \mathbf{x}_m)$ denotes the mth object pixel and $\mathcal{G}_m(\mathbf{x})$ is the spectrum of the object pixel. In the narrow wavelength bands (<30 nm), the PSF, $\mathcal{S}(\mathbf{x})$, is wavelength independent. The objective prism spectrum, $\sum_m \mathcal{O}_m(\mathbf{x} - \mathbf{x}_m) * \mathcal{G}_m(\mathbf{x})$, can be reconstructed from the speckle spectrograms.

4.3. Speckle polarimetry

Polarized light carries valuable information about where the light is produced, and the various physical parameters which have been responsible for its generation. Processes such as magnetic fields, chemical interactions, molecular structure and mechanical stress cause changes in the polarization state of an optical beam. Applications relying on the study of these changes cover a vast area, viz., astrophysics, molecular biology, electric power generation etc.

The importance of polarimetric observations in astronomy is to obtain information such as dust around stars, size and shape of the dust grains, magnetic fields etc. Among other scientific objectives, (i) the wavelength dependence of the degree of polarization and the rotation of the position angle in stars with extended atmospheres, (ii) the wavelength dependence of degree of polarization and position angle of light emitted by stars present in very young ($\leq 2 \times 10^6$ years) clusters and associations are the important ones to investigate.

The effect on the statistics of a speckle pattern is the degree of depolarization caused by the scattering at the surface. If the light is depolarized, the resulting speckle field is considered to be the sum of two component speckle fields produced by scattered light polarized in two orthogonal directions. The intensity at any point is the sum of the intensities of these component speckle patterns (Goodman, 1975). These patterns are partially correlated, therefore, a polarizer that transmits one of the component speckle patterns, can be used in the speckle camera system.

The advantage of using speckle camera over conventional imaging polarimeter is the capability of monitoring the short-time variability of the atmospheric transmission. Another advantage of high resolution polarimetry is that of using it as a tool to get insight on the binary star mechanism. Recently, speckle polarimetry has been used to obtain polarimetric information with sub-arc-second resolution of astronomical objects (Falcke et al., 1996, Fischer et al., 1998). Falcke et al., (1996) developed a speckle imaging polarimeter consisting of a rotatable, achromatic $\lambda/2$ - retardation mica plate in front of a

fixed polarization filter. These elements were installed on a single mount and inserted into the optical axis in front of the telescope focus of their speckle camera.

4.4. Differential speckle interferometry

Differential speckle interferometry is a method to observe the objects in different wave modes simultaneously and computes the average cross-spectrum or cross-correlation of pairs of speckle images (Beckers, 1982). This technique can be used to resolve close binary system below the diffraction limit of the telescope, as well as to determine (i) the relative orbit orientations in multiple system, (ii) the masses of double-lined spectroscopic system, (iii) the masses of long period binary systems (Tokovinin (1992). Sub-diffraction limit of. measurement of the displacement of the photo-centre of a unresolved object as a function of wavelength has also been reported (Petrov et al., 1992).

Let $\mathcal{O}_1(\mathbf{x})$ and $\mathcal{O}_2(\mathbf{x})$, be respectively the object and reference brightness distributions, and $\mathcal{I}_1(\mathbf{x})$ and $\mathcal{I}_2(\mathbf{x})$ are their associated instantaneous image intensity distributions. The relation between the object and the image in the Fourier space becomes

$$\widehat{\mathcal{I}}_1(\mathbf{u}) = \widehat{\mathcal{O}}_1(\mathbf{u}) \cdot \widehat{\mathcal{S}}_1(\mathbf{u}), \tag{72}$$

$$\widehat{\mathcal{I}}_2(\mathbf{u}) = \widehat{\mathcal{O}}_2(\mathbf{u}) \cdot \widehat{\mathcal{S}}_2(\mathbf{u}), \tag{73}$$

where, $\widehat{\mathcal{S}}_1(\mathbf{u})$ and $\widehat{\mathcal{S}}_2(\mathbf{u})$ are the related transfer functions.

The average cross-spectrum between the object and the reference,

$$< \widehat{\mathcal{I}}_1(\mathbf{u})\widehat{\mathcal{I}}_2^*(\mathbf{u}) > = \widehat{\mathcal{O}}_1(\mathbf{u})\widehat{\mathcal{O}}_2^*(\mathbf{u}) \cdot < \widehat{\mathcal{S}}_1(\mathbf{u})\widehat{\mathcal{S}}_2^*(\mathbf{u}) > . \tag{74}$$

The transfer function for the cross-spectrum, $< \widehat{\mathcal{S}}_1(\mathbf{u})\widehat{\mathcal{S}}_2^*(\mathbf{u}) >$, can be calibrated on reference point source for which, $< \widehat{\mathcal{O}}_1(\mathbf{u}) > = < \widehat{\mathcal{O}}_2(\mathbf{u}) > = 1$. If the two spectral windows are close enough $(\Delta\lambda/\lambda \ll r_0/D)$, the instantaneous transfer function can be assumed identical in both the channels $[\mathcal{S}_1 = \mathcal{S}_2 = \mathcal{S}]$. Therefore, equation (74) can be translated in to,

$$\widehat{\mathcal{O}}_1(\mathbf{u}) = \frac{< \widehat{\mathcal{I}}_1(\mathbf{u})\widehat{\mathcal{I}}_2^*(\mathbf{u}) >}{\widehat{\mathcal{O}}_2^*(\mathbf{u}) <| \widehat{\mathcal{S}}(\mathbf{u}) |^2>} = \widehat{\mathcal{O}}_2(\mathbf{u})\frac{< \widehat{\mathcal{I}}_1(\mathbf{u})\widehat{\mathcal{I}}_2^*(\mathbf{u}) >}{<| \widehat{\mathcal{I}}_2(\mathbf{u}) |^2>}. \tag{75}$$

The noise contributions from two different detectors are uncorrelated, thereby, their contributions cancel out. Aime et al., (1985) have used cross-spectral analysis to correlate the solar photospheric brightness and velocity fields.

Differential interferometry estimates the ratio, $\widehat{\mathcal{O}}_1(\mathbf{u})/\widehat{\mathcal{O}}_2(\mathbf{u})$ and the differential image, $\mathcal{D}_{\mathcal{I}}(\mathbf{x})$, can be obtained by performing inverse Fourier transform of this ratio,

$$\mathcal{D}_{\mathcal{I}}(\mathbf{x}) = \mathcal{F}^{-1}\left[\frac{<\widehat{\mathcal{I}}_1(\mathbf{u})\widehat{\mathcal{I}}_2^*(\mathbf{u})>}{<|\widehat{\mathcal{I}}_2(\mathbf{u})|^2>}\right] \qquad (76)$$

$\mathcal{D}_{\mathcal{I}}(\mathbf{x})$ is self calibrating for seeing and represents an image of the object in the emission feature having the resolution of the object imaged in the continuum (Hebden et al., 1986). Petrov et al., (1986) found an increase in S/N ratio as the band-passes of the two components of the dual specklegram increase.

4.5. Pupil plane interferometry

In the shearing interferometer, interference fringes are produced by two partially or totally superimposed pupil images created by introducing a beam splitter. At each point, interference occurs from the combination of only two points on the wave-fronts at a given baseline, and therefore, behaves as an array of Michelson-Fizeau interferometers. The true object visibility can be recorded by employing the short-exposure. The major advantage of this technique over speckle interferometry is to obtain better S/N ratio on bright sources. The other noted advantages are the insensitivity to calibrate errors due to seeing fluctuations, as well as to telescope aberrations (Roddier and Roddier, 1988). It also makes a better use of the detector dynamic range to detect faint extended structure like stellar envelopes. The following paragraphs enumerates the various types of shearing interferometers.

(i) The lateral shearing interferometer (Cognet 1973, Ribak and Lipson, 1981) shifts the wave-front laterally and mixing it with itself, thereby, obtains the interference patterns which correspond to the wave-front tilt in the shear direction. It is necessary to make two orthogonal measurements to assess the full wave-front tilt. To be precise, this typed interferometer splits the incident field into two optical beams (x and y direction beam). Before detection the beams are split again and laterally shifted (sheared) with respect to each other. All the baselines are identical and a single object Fourier component is measured at a time. To achieve shear one can either make use of gratings (Wyant, 1974, Horwitz, 1990) or use of beam separation by polarization (Hardy and MacGovern, 1987). Depending on the specific type of interferometer, the optical field in each leg is split a number of times (Sandler et al., 1994). The sheared beams are superimposed in a detector to form fringe.

Ribak et al., (1985) enumerated a modified system in which fringes are detected independently in several channels. At increasing baselines, there is a loss of photons. Many sequential measurements are needed to explore the object Fourier spectrum (Roddier, 1988b). The concept of developing an interferometer based on using Babinet compensator (BC) has also been reported (Saxena and Jayarajan, 1981, Saxena and Lancelot, 1982). The system is similar to that of a single beam lateral shearing polarizing interferometer. The cone of light passing through BC would produce fringe pattern due to the

different phase change introduced between the extraordinary and the ordinary vibrations at different points during the oblique passage of the ray.

(ii) The wave-front folding interferometer produces 1-d Fourier transform, providing information on all the object Fourier components in one direction. The other direction may be obtained sequentially. In this interferometer, one pupil image is superimposed to its mirror image and is made of a beam splitter, a flat mirror in one arm and a roof prism in the other arm (Mertz, 1970). The shortcomings of this system comes from the loss of light as it is reflected back to the sky and produces low contrast fringes owing to mismatch of orthogonal polarizations.

(iii) The rotation shear interferometer produces 2-d Fourier transform (Mertz, 1970). In this, one pupil image is rotated with respect to the other. If the rotation axis coincides with the centre of the pupil, the two images overlap. All the object Fourier components within telescope diffraction cutoff frequency are measured simultaneously. Breckinridge (1978) suggested the use of 180° rotational shear. In this system, light enters a beam splitter and is reflected back through a roof prism in each arm; the roof edges are set at right angles to each other. Similar shortcomings can be noticed (Roddier, 1988b) as in the case of wave-front folding interferometer described above. Variable rotational shear was used to develop a similar interferometer by Roddier and Roddier, (1983), where one roof prism is allowed to rotate around the optical axis. They have introduced a phase plate between the beam splitter and the roof prism to correct the mismatch of polarization. A similar set-up has been developed by a group and was able to record fringes of a few bright objects (Saxena, 1993).

4.6. Phase-closure imaging

The advantage of closure-phase technique (Jennison, 1958) in high resolution imaging is that its visibility remains uncorrupted in the presence of atmospheric turbulence. This technique has been applied in the field of radio astronomy. Its potential lies in exploiting fully the resolution attainable with large optical telescope (Baldwin et al., 1986). Equation (62) represents the simplest form of the phase closure technique but unfortunately phase information is not preserved. The phase-closure requirement can be redefined in terms of spatial frequency vectors forming a closed loop. The phase-closure is achieved (equation 62) in the power spectrum by taking pairs of vectors of opposite sign, $-\mathbf{u}$ and $+\mathbf{u}$, to form a closed loop. The closure phase, $\beta_{123}-$ the sum of observed phases around a triangle of baselines is the sum of phases of the source Fourier components and can be derived as,

$$\beta_{123} = \psi_{12} + \psi_{23} + \psi_{31}, \tag{77}$$

where, the subscripts refer to the antennae at each end of a particular baseline, ψ_{ij} are the observed phases of the fringes produced by the antennae i and j on a different baselines; contain the phases of the source Fourier components $\psi_{0,ij}$ and also the error terms.

The observed fringes, ψ_{ij}, represent the following equation,

$$\psi_{ij} = \psi_{0,ij} + \theta_i - \theta_j,$$ (78)

where, θ_i, θ_j, introduced by errors at the individual antenna, as well as by the atmospheric variations at each antenna. Therefore, by adding the corresponding equations the following relationship emerges,

$$\beta_{123} = \psi_{0,12} + \psi_{0,23} + \psi_{0,31}.$$ (79)

Equation (79) implies cancelations of the antennae phase errors. Figure 7 describes the concept of a three element interferometer.
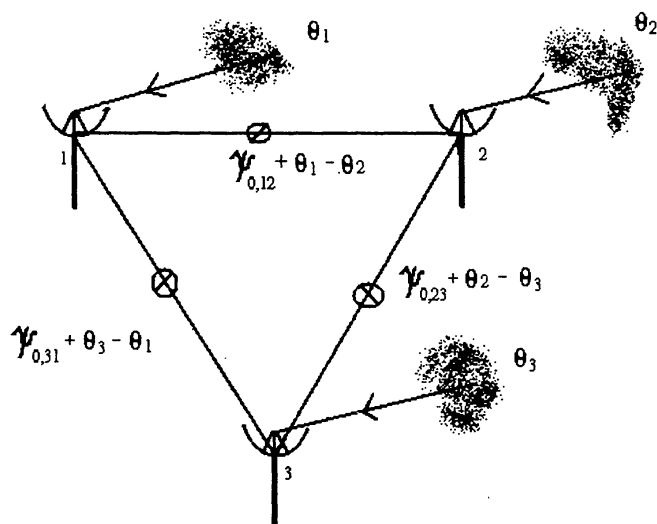

Figure 7. Concept of three element interferometer.

Rogstad (1968) suggested the use of phase-closure technique in optics. Later, several observers (Baldwin et al., 1986, Readhead et al., 1988) reported the measurements of the closure-phases obtained at high light level with three hole aperture mask set in the pupil plane of the telescope and recorded interference pattern of the object using CCD as detector. Similar experiment was conducted by the author around the same time using aperture mask of 3-hole, placed over the telescope, as well as in the laboratory (Saha et al., 1987, 1988, Saha, 1999).

4.6.1. Aperture synthesis

The aperture synthesis imaging technique with telescope involves observing an object through a masked aperture of several holes and recording the resulting interference pattern in a series of short-exposures. Such a mask introduces a series of overlapping two-hole interference patterns projected onto the detector allowing the Fourier amplitude and phase of each baseline can be recovered. By summing up the Fourier phases around each closed triangle, the closure-phase can be obtained (section 4.6).

If a telescope aperture is made of elementary sub-apertures as enumerated in section (3.4), the complex amplitude, Ψ, of the field in the telescope plane is obtained by adding the contribution, Ψ_n, of each sub-aperture (Born and Wolf, 1984). From the equation (64), the illumination $\mid \Psi \mid^2 = \mid \sum_{n,m} \Psi_n \mid^2$, can be written as,

$$\mid \sum_{n,m} \Psi_n \mid^2 = \sum_{n,m} \mid \Psi_n \mid^2 + \sum_{n \neq m} \sum_m \Psi_n \Psi_m^*. \tag{80}$$

The second term of the right-hand side of this equation, describes the interference through the cross product, contains high resolution information. An image can be reconstructed from sequential measurements of all the cross products using pairs of sub-apertures. For n apertures, there are $n(n-1)/2$ independent baselines, with, $n-1$ unknown phase errors. This implies that by using many telescopes in an interferometric array, most of the phase informations can be retrieved.

Non-redundant masking method has been successfully developed and used at telescopes by several groups (Haniff et al., 1987, 1989, Nakajima et al., 1989, Busher et al., 1990, Bedding et al., 1992, 1994, Vasisht et al., 1998, Prieur et al., 1998, Monnier et al., 1999). Some of these experimental details can be found in the article (Saha, 1999 and references therein). In the laboratory, Saha et al., (1988) studied the shapes of fringe pattern of n-hole apertures by introducing different aperture masks of various sizes arranged in both redundantly and non-redundantly.

The advantage of such a technique at telescopes is the built-in delay to observe objects at low declinations. It produces the optical aperture synthesis maps of high dynamic range but is restricted to only high light levels. The instantaneous coverage of spatial frequencies is sparse and most of the available light is discarded. Improvement can be foreseen in utilizing rotatable masks to several different position angles on the sky. Haniff and Busher (1992) have used a doubly-redundant mask geometry for faint source. A new device using cylindrical lens in lieu of aperture mask has been developed recently by Bedding (1999) for fainter objects.

5. Detectors

During the initial phases of the development in speckle interferometry, a few observers used photographic films with an intensifier attached to it for recording speckles of various

stars (Breckinridge et al., 1979). Saha et al., (1987) used a bare movie camera to record the fringes and specklegrams of a few bright stars. Owing to low quantum efficiency of the photographic emulsion, usage of the modern ICCD camera system or a intensified photon counting system (Boksenburg, 1975) became necessary to gather the speckles of faint objects. Though the water-cooled bare CCD was used for certain interferometric observations (Saha et al., 1997c), it is essential to obtain snap shots of very high time resolution of the order of (i) frame integration of 50 Hz (Blazit et al., 1977a, Blazit, 1986), (ii) photon recording rates of a few MHz (Papaliolios et al., 1985, Durand et al., 1987, Paresce et al., 1988, Timothy et al., 1989, Nightingale, 1991, Graves et al., 1993). The following sub-sections enunciate the salient features of various modern recording devices.

5.1. Frame transfer camera system

The frame transfer intensified CCD (ICCD) detector consists of an image intensifier coupled to a CCD camera (Lemonier et al., 1988); the system employs micro-channel plate (MCP) as an intensifier. In the MCP image intensifier, the photo-electron is accelerated into a channel of the MCP releasing secondaries and producing an output charge cloud of about $10^3 - 10^4$ electrons with 5 - 10 kilovolt (KV) potential. With further applied potential of $\sim$ 5 - 7 KV, these electrons are accelerated to impact a phosphor, thus producing an output pulse of $\sim 10^5$ photons. These photons are directed to the CCD by fibre optic coupling and operate at commercial video rate with an exposure of 20 ms per frame (Chinnappan et al., 1991). The video frame grabber cards digitize and store the images in the memory buffer of the card. Depending on the buffer size, the number of interlaced frames stored in the personal computer (PC) can vary from 2 to 32 (Saha et al., 1997a).

McAlister et al., (1987) used an ICCD system which had 30 μm square pixels in a 244×248 format for their interferometric binary star survey programmes. The frame rate varied from 1 - 15 ms by means of gating the voltage of the photo-cathode of the image intensifier. Subsequently, they have obtained another system, ITT camera, with single-stage intensified CCD, which allows detection to a magnitude limit of $m_v \sim 10$ for 90 s integrations (Mason et al., 1993). ICCDs with low duty cycles that are capable of recording a few frames per second (Weigelt et al., 1996) have also been in use. Aristidi et al., (1997) uses a system that has a single stage intensifier and is thus unable to reach beyond $m_v \sim 10$. The exposure time is tunable between 64 μs and 16 ms. The output is an analog video signal, recorded on SVHS video cassettes (Prieur et al., 1998).

Another version of the ICCD (386×576) camera with Peltier cooled system is currently available at IIA, Bangalore, India, which offers options of choosing the exposure time, viz., 1 ms, 5 ms, 10 ms, 20 ms etc. It can operate in full frame, frame transfer and kinetic modes. Since the CCD is cooled to $\sim 40°$, the dark noise is low. Data are digitized to 12 bits and can be archived to a Pentium based PC. In full frame, as well as in frame transfer modes, the region of interests can be acquired at a faster speed. While in the kinetic mode, the image area can be kept small to satisfy the requirements. Horch et al., (1998) came up with a new concept of using large format scientific grade CCD as the

imager to collect speckle patterns. The system consists of an optics module that contains a piezoelectric tip-tilt mirror capable of executing a timed sequence of movements to place many speckle patterns in a block pattern over the entire active area of the CCD chip.

5.2. Photon counting camera system

Ever since the successful development of a photon counting detector system (Boksenburg, 1975), a number of different classes of photon counting systems are in use. The typical values for an object of $m_v = 12$ over a field of 2.5″ are < 50 photons/ms within the narrow band filter. The marked advantage of such a scheme is that of reading the signal a posteriori to optimize the correlation time of short exposures in order to overcome the loss of fringe visibility due to the speckle lifetime. The other notable features are, (i) capability of determining the position of a detected photon to 10 μm to 10 cm, (ii) ability to register individual photons with equal statistical weight and produces signal pulse (with dead time of ns), and (iii) low dark noise typically of the order of 0.2 counts $cm^{-2}s^{-1}$.

5.2.1. CCD-based photon counting system

Blazit et al., (1977a) had used a photon counting system which is coupled with a micro-channel image intensifier to a commercial television camera. This camera operates at the fixed scan line (312) with 20 ms exposure. A digital correlator discriminates the photon events and computes their positions in the digital window. It calculates the vector differences between the photon positions in the frame and integrates in memory a histogram of these difference vectors.

Subsequently, Blazit (1986) has developed another version of the photon counting system (CP40), comprising a set of four Thomson 288×384 CCDs image sensors with a common stack of a 40 mm diameter Varo image tube and a MCP. The readout of this system is standard, 20 ms. The amplified image is split into four quadrants through a fibre optics reducer and four fibre optics cylinders. Each of these quadrants is read out with a CCD device at the video rate (50 Hz). This camera is associated with the CP40 processor — a hardware photon centroiding processor to compute the photo-centre of each event with an accuracy of 0.25 pixel.

The major shortcomings of such system arise from the (i) calculations of the coordinates which are hardware-limited with an accuracy of 0.25 pixel, and (ii) limited dynamic range of the detector. This system is regularly used by the groups at Observatoire de la Cote d'Azur, France, for the speckle interferometric programmes as well as to record the fringes of stars (Mourard et al., 1989, 1992, 1994a) using Grand Interféromètre à Deux Télescope (GI2T). Morel and Koechlin (1998) came out with a concept of using 3 linear CCDs with a 2.6 μs read-out at rates up to a million photons per second. A new photon counting camera that allows a high photon rate and a direct numerisation of photon coordinates is under way (Koechlin and Morel, 1998).

5.2.2. Precision analog photon address (PAPA)

The Precision Analog Photon Address (PAPA) camera is a 2-d photon counting detector which allows recording of the address (position) and time of arrival of each detected photon (Papaliolios et al., 1985). The front-end of the camera is a high gain image intensifier which produces a bright spot on its output phosphor for events detected by the photo-cathode. The back face (phosphor) of the intensifier is then re-imaged by an optical system which is made up of a large collimating lens and an array of smaller lenses. Each of the small lenses produces a separate image of the phosphor on a mask to provide position information of the detected photon. Behind each mask is a field lens which relays the pupil of the small lens onto a small photo-multiplier (PMT). A set of 19 PMTs used out of which 9 + 9 PMTs provides a format of 512×512 pixels optical configuration. The 19th tube acts as an event strobe, registering a digital pulse if the spot in the phosphor is detected by the instrument. 9 tubes are used to obtain positional information for an event in one direction, while the other 9 are used for that in the orthogonal direction. If the photon image falls on clear area, an event is registered by the photo-tubes. The masks use grey code which ensures that mask stripes do not have edges located in the same place in the field.

This first generation of the PAPA detector was used to record the specklegrams of the stellar objects by the group at Center for Astrophysics, Harvard-Smithsonian Observatory, Harvard (Nisenson, 1988 and references therein), as well as to record the fringes of stars using long baseline interferometers by groups at Mt. Wilson (Kaplan et al., 1988) and at Sydney (Lawson, 1994). A modified PAPA camera has been used to observe close binary stars (Aristidi et al., 1999). This version has a new binary mask and refurbished image intensifier. Another modified version of the system with 2000×2000 pixels has been developed by using a CeTe photo-cathode intensifier for the NASA UV applications (Nisenson, 1997). The photo-cathode is sensitive down to 100 nm and operates in vacuum. The system runs at a maximum count rate of 2 million per second. Figure 8 depicts an overview of PAPA camera made for NASA UV applications. The new generation PAPA would replace PMTs by a set of intensified photo-diodes (Nisenson, 1997).

5.2.3. MCP based photon counting detector

Several electronic readout techniques have been developed to detect the charge cloud from a high gain MCP. Some of these systems provide 2-d imaging capabilities (Lampton and Carlson, 1979, Martin et al., 1981, Timothy, 1986, Siegmund et al., 1994). The main advantage of such systems is to obtain spatial event information by means of the position sensitive readout systems; the encoding systems identify each event's location. The short-comings of the MCPs are notably due to its local dead-time which essentially restricts the conditions for use of these detectors for high spatial resolution applications (Rodriguez et al., 1992). These constraints are also related with the luminous intensity and the pixel size. The following paragraphs elucidate a few of these systems.
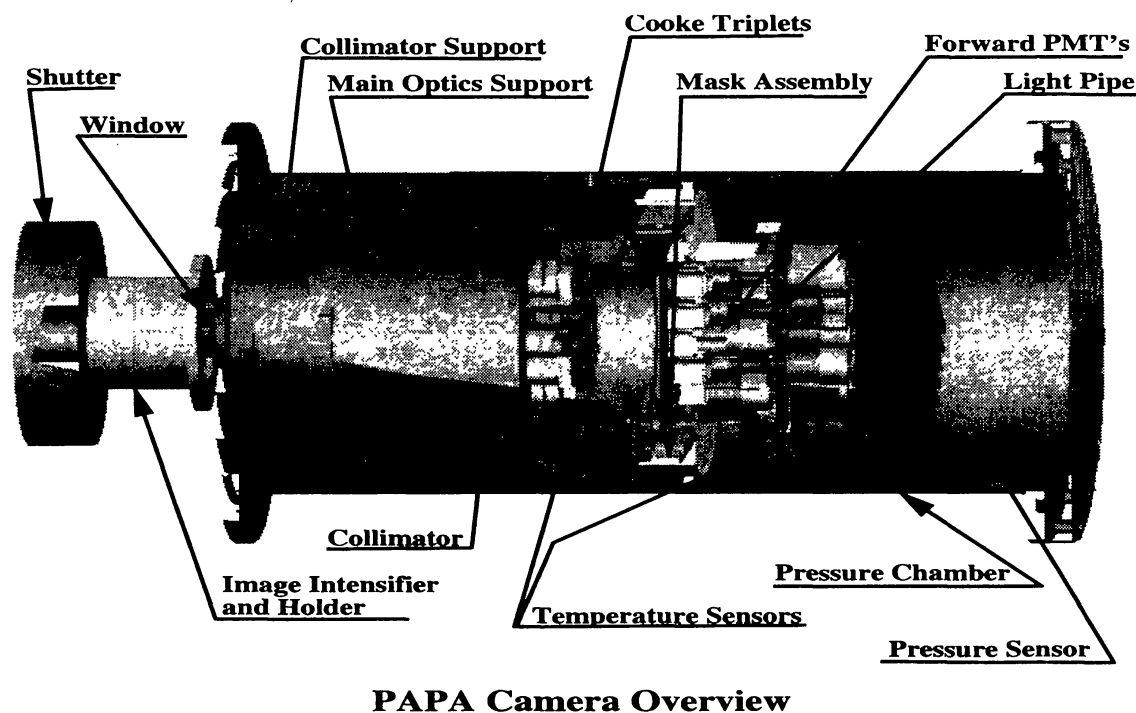
PAPA Camera Overview

Figure 8. An overview of the PAPA camera (Courtesy: P. Nisenson)

(i) In the resistive anode position sensing detector system, a continuous uniform resistive sheet with appropriately shaped electrodes provides the means for encoding the simultaneous location and arrival time of each detected photon. The semi-transparent photo-cathode converts the photons to electrons. This is coupled to a cascaded stack of MCPs acting as the position sensitive signal amplifier. A net potential drop of about 5 KV is maintained from the cathode to the anode. Each primary photo-electron results in an avalanche of $10^7 - 10^8$ secondary electrons onto the resistive anode. The signals resulting from the charge redistribution on the plate are amplified and fed into a high speed signal processing electronics system that produces 12 bit x, y addresses for each event. A PC based data acquisition system builds up a 1024×1024 image from this asynchronous stream of x, y values that can be stored in a PC (Clampin et al., 1988, Paresce et al., 1988). Nakajima et al., (1989) used a similar one for their programme. The drawback of this system is the large pixel response function; the nominal resolution of the system is about 60 μm. For certain applications, this system is used regularly on the GI2T (Mourard et al., 1994a).

(ii) The photon counting system based on the wedge-and-strip anodes (Siegmund et al., 1986), uses conductive array structure, in which the geometrical image distortions might be eliminated. It comprises multiple terminals with the x, y co-ordinate of a charge cloud determined through ratios of charge deposited onto the various terminals. The amplitudes of the signals detected on the wedge, strip and electrodes are linearly proportional to the x, y co-ordinates of the detected photon event. In this system, the spatial resolutions of the order of 40 - 70 μm FWHM and position sensitivities of 10 μm

are obtained at high MCP gains. High resolution wedge-and-strip detectors can operate at event rates up to about 5×10^4 photons per second.

(iii) Another photon counting system based on the delay line anodes has been developed (Lampton et al., 1987, Siegmund et al., 1994) for micro-channel plate spectrometers. The delay line anodes offer high resolution pixels of the order of 15 μm FWHM, as well as high event rate of the order of more than 4×10^5 photons per second (Siegmund et al., 1994). The delay line anode has a zigzag micro-strip transmission line etched onto a low loss, high dielectric substrate. The position of the charge cloud event is encoded as the difference in arrival times of the charge pulse at both ends of the transmission line.

(iv) A new photon counting system, silicon anode detector with integrated electronics is underway (Chakrabarti, 1998). This system offers to integrate the anode of the detector and all supporting electronics onto a single silicon substrate. A charge cloud from the MCP strikes the conducting strips on an anode. The charge is gated into a serial CCD shift register through field effect transistor (FET) charge transfer gates. The captured charge in the CCD can be clocked out through an amplifier using three phase shifting technique. The maximum estimated possible count rate is of 1×10^6 photons per second.

5.2.4. Multi anode micro-channel array (MAMA)

The multi anode micro-channel array (MAMA) detector allows high speed, discrete encoding of photon positions and makes use of numerous anode electrodes that identify each event's location (Timothy, 1993). In this system, the electron amplification is obtained by an MCP and the charge is collected on a crossed grid coincidence array (Timothy et al., 1989). The resulting electron cloud hits two sets of anode arrays beneath the MCP, where one set is perpendicular in orientation to the other; the charge collected on each anode is amplified. The position of the event is determined by coincidence discrimination. The C-plate type MCP, which is a single curved plate that prevents ion feedback, is used. The present generation MAMA detector has the pixel format of 224×960 with 14 or 25 μm square pixels and is equipped with the application specific integrated circuit pixel decoders (Kasle and Morgan, 1991). The pulse-pair resolution is reported to be better than 200 ns. MAMA detector is used for speckle interferometric observations by the group at Stanford University (Horch et al., 1992, 1996).

6. Image processing

The autocorrelation technique enumerated in section 4.1.3. falls short of providing true image reconstructions. The diffraction-limited phase retrieval by various methods, viz., (i) speckle holography method, (ii) shift-and-add method, (iii) Knox-Thomson (KT) technique, (iv) triple-correlation (TC) technique, (v) non-redundant aperture masking technique (Rhodes and Goodman, 1973), (vi) maximum entropy (MEM) method (Jaynes, 1982), (vii) CLEAN algorithm (Hogbom, 1974), (viii) blind iterative deconvolution (BID) technique, have, by and large, produced qualitative scientific results. The following subsections outline some of these techniques of estimating the Fourier phase.

6.1. Speckle holography method

If a reference point source is available within the iso-planatic patch ($\sim 7''$), it can be used as a key to reconstruct the target source in the same way as a reference coherent beam is used in holographic reconstruction (Liu and Lohmann, 1973, Weigelt, 1978). Let the point source be represented by a Dirac impulse, $\mathcal{A}\delta(\mathbf{x})$, at the origin and $\mathcal{O}_1(\mathbf{x})$ be the nearby object to be reconstructed. The intensity distribution in the field of view is

$$\mathcal{O}(\mathbf{x}) = \mathcal{A}\delta(\mathbf{x}) + \mathcal{O}_1(\mathbf{x}). \tag{81}$$

A regular speckle interferometric measurement will give the squared modulus of its Fourier transform, $\widehat{\mathcal{O}}(\mathbf{u})$,

$$\mid \widehat{\mathcal{O}}(\mathbf{u}) \mid^2 = \mid \mathcal{A} + \widehat{\mathcal{O}}_1(\mathbf{u}) \mid^2 = \mathcal{A}^2 + \mathcal{A}\widehat{\mathcal{O}}_1(\mathbf{u}) + \mathcal{A}\widehat{\mathcal{O}}_1^*(\mathbf{u}) + \widehat{\mathcal{O}}_1(\mathbf{u})\widehat{\mathcal{O}}_1^*(\mathbf{u}). \tag{82}$$

The inverse Fourier transform gives the autocorrelation, $\mathcal{C}_{\mathcal{O}}(\mathbf{x})$, of the field of view

$$\mathcal{C}_{\mathcal{O}}(\mathbf{x}) = \mathcal{A}^2\delta(\mathbf{x}) + \mathcal{A}\mathcal{O}_1(\mathbf{x}) + \mathcal{A}\mathcal{O}_1(-\mathbf{x}) + \mathcal{C}_{\mathcal{O}_1}(\mathbf{x}), \tag{83}$$

where, $\mathcal{C}_{\mathcal{O}_1}(\mathbf{x})$ is the autocorrelation of the object.

The first and the last term in equation (83) are centred at the origin. If the object is far enough from the reference source, $\mathcal{O}(\mathbf{x})$, its mirror image, $\mathcal{O}(-\mathbf{x})$, is therefore recovered apart from a 180° rotation ambiguity. Weigelt (1978) had retrieved the deconvolved images of close multiple systems, ζ Cancri and ADS3358, using this algorithm.

Another method, known as cross-spectrum analysis, is to calculate the cross-spectrum between the object and the reference source (see section 4.4). The angular distance between the two sources should be within the iso-planatic patch or the two spectral windows should be close enough. Equation (75) showed that the speckle holography transfer function, $<\mid \widehat{\mathcal{S}}(\mathbf{u}) \mid^2>$, is real. The method is insensitive to aberrations and the expected value of the phase of the cross-spectrum coincides with the phase-difference between the object and the reference. However, when this is not the case, one must use image processing methods by using the different light levels of the speckle clouds (reference and target) to extract the object.

6.2. Shift-and-add algorithm

In this technique, the image data frame is shifted so that the pixel with maximum S/N in each frame can be co-added linearly at the same location in the resulting accumulated image (Lynds et al., 1976, Worden et al., 1976). In a blurred image, each speckle is considered as a distorted image of the object, the brightest one being the least distorted.

S. K. Saha

In this processes, the position of the brightest pixel, $\mathbf{x}_k$, is necessary to be located in each specklegram, $\mathcal{I}_k(\mathbf{x})$, $[\mathcal{I}_k(\mathbf{x}_k) > \mathcal{I}_k(\mathbf{x})$ for all $\mathbf{x} \neq \mathbf{x}_k]$, followed by shifting the specklegram (without any rotation) to place this pixel at the centre of the image space. The shift-and-add image, $\mathcal{I}_{sa}(\mathbf{x})$, is obtained by averaging over the set of the shifted specklegrams,

$$\mathcal{I}_{sa}(\mathbf{x}) = < \mathcal{I}_\mathbf{k}(\mathbf{x} + \mathbf{x_k}) > . \tag{84}$$

The large variations in the brightness of the brightest pixels can be observed in a set of speckle images. The contamination level of a specklegram may not be proportional to the brightness of its brightest pixel (Bates and McDonnell, 1986). The adjusted shift-and-add image, $\mathcal{I}_{asa}(\mathbf{x})$, be defined as,

$$\mathcal{I}_{asa}(\mathbf{x}) = < w[\mathcal{I}_k(\mathbf{x}_k)]\mathcal{I}_k(\mathbf{x} + \mathbf{x}_k) >, \tag{85}$$

where, $w[\mathcal{I}_k(\mathbf{x}_k)]$ is the weighting in relation with the brightness of the brightest pixel. The choice of the same quantity can be made as $w\{\mathcal{I}_k(\mathbf{x}_k)\} = \mathcal{I}_k(\mathbf{x}_k)$.

An array of impulse is constructed by putting an impulse at each of the centre of gravity with a weight proportional to the speckle intensity. This impulse array is considered to be an approximation of the instantaneous PSF and is cross-correlated with the speckle frame (see section 6.1). Disregarding the peaks lower than the pre-set threshold as enumerated above, the mth speckle mask, $mask_m(\mathbf{x})$, is defined by,

$$mask_m(\mathbf{x}) = \sum_{n=1}^{M} \mathcal{I}_m(\mathbf{x}_{m,n})\delta(\mathbf{x} - \mathbf{x}_{m,n}). \tag{86}$$

The mth masked speckled image, $m\mathcal{I}_m(\mathbf{x})$, is expressed as,

$$m\mathcal{I}_m(\mathbf{x}) = \mathcal{I}_m(\mathbf{x}) \otimes mask_m(\mathbf{x}), \tag{87}$$

where, $\otimes$ stands for correlation.

The Lynds-Worden-Harvey image can be obtained by averaging $< m\mathcal{I}_m(\mathbf{x}) >$. This technique contains more information in each $\mathcal{I}_m(\mathbf{x})$ than $\mathcal{I}_{asa}(\mathbf{x})$, and therefore, exhibits more S/N. For direct speckle imaging, the shift-and-add image, $\mathcal{I}_{sa}(\mathbf{x})$, is a contaminated one containing two complications - a convolution, $\mathcal{S}_k(\mathbf{x})$ and an additive residual, $\mathcal{C}(\mathbf{x})$ - which means,

$$\mathcal{I}_{sa}(\mathbf{x}) = \mathcal{O}(\mathbf{x}) * \mathcal{S}(\mathbf{x}) + \mathcal{C}(\mathbf{x}), \tag{88}$$

where, $\mathcal{S}(\mathbf{x}) = \sum_{k=1}^{k} \delta(\mathbf{x} - \mathbf{x}'_k)d_k$, $\mathbf{x}'_k$ being the constant position vectors and d_k, the positive constant.

It is essential to calibrate $\mathcal{I}_{sa}(\mathbf{x})$ with an unresolved point source and reduce it in the same way to produce $\mathcal{S}(\mathbf{x})$. The estimate for the object, $\mathcal{O}(\mathbf{x})$, is evaluated from the inverse Fourier transform of the following equation,

$$\widehat{\mathcal{O}}(\mathbf{u}) = \frac{\widehat{\mathcal{I}}_{sa}(\mathbf{u})}{\widehat{\mathcal{I}}_o(\mathbf{u}) + \widehat{\mathcal{N}}(\mathbf{u})}, \tag{89}$$

where, $\widehat{\mathcal{N}}(\mathbf{u})$ stands for the noise spectrum.

This is the first approximation of the object irradiance. If this technique is applied to a point source, an image similar to Airy pattern yields. This method is found to be insensitive to the telescope aberrations. The limitation of this algorithm is not being applicable when photon noise dominates in addition to the accuracy with which speckle maxima are located. Ribak, (1986) used an iterative matched filter approach to reconstruct the image.

6.3. Knox-Thomson technique (KT)

The Knox-Thomson method (Knox and Thomson, 1974), which is a small modification of the autocorrelation technique, involves the centering in each specklegram with respect to its centroids and in finding the ensemble autocorrelation of the Fourier transform of the instantaneous image intensity.

In lieu of the image energy spectrum, $<| \widehat{\mathcal{I}}(\mathbf{u}) |^2>$, let the general second order moment be the cross spectrum, $< \widehat{\mathcal{I}}(\mathbf{u}_1)\widehat{\mathcal{I}}^*(\mathbf{u}_2) >$. The cross-spectrum takes significant values only if $| \mathbf{u}_1 - \mathbf{u}_2 | < r_o/\lambda$. The typical value of $| \Delta\mathbf{u} |$ is $\sim$ 0.2 - 0.5 r_o/λ. Invoking equation (67), a 2-d irradiance distribution, $\mathcal{I}(\mathbf{x})$ and its Fourier transform, $\widehat{\mathcal{I}}(\mathbf{u})$, is defined by the equation,

$$\widehat{\mathcal{I}}(\mathbf{u}) = \int_{-\infty}^{+\infty} \mathcal{I}(\mathbf{x})e^{-i2\pi\mathbf{u}\mathbf{x}}d\mathbf{x}. \tag{90}$$

Unlike the autocorrelation technique (see section 3.4.1.), KT technique defines the correlation of $\mathcal{I}(\mathbf{x})$ and $\mathcal{I}(\mathbf{x})$ multiplied by a complex exponential factor with a spatial frequency larger than zero. In image space, the correlations of $\mathcal{I}(\mathbf{x})$, is derived as,

$$\mathcal{I}(\mathbf{x}_1, \Delta\mathbf{u}) = \int_{-\infty}^{+\infty} \mathcal{I}^*(\mathbf{x})\mathcal{I}(\mathbf{x} + \mathbf{x}_1)e^{i2\pi\Delta\mathbf{u}\mathbf{x}}d\mathbf{x}, \tag{91}$$

where, $\mathbf{x}_1 = \mathbf{x}_{1x} + \mathbf{x}_{1y}$ are 2-d spatial co-ordinate vectors.

In Fourier space, $\widehat{\mathcal{I}}(\mathbf{u})$ gives the following relationship,

$$\widehat{\mathcal{I}}(\mathbf{u}_1, \Delta\mathbf{u}) = \widehat{\mathcal{I}}(\mathbf{u}_1)\widehat{\mathcal{I}}^*(\mathbf{u}_1 + \Delta\mathbf{u}), \tag{92}$$

where, $\mathbf{u}_1 = \mathbf{u}_{1x} + \mathbf{u}_{1y}$, and $\Delta\mathbf{u} = \Delta\mathbf{u}_x + \Delta\mathbf{u}_y$ are 2-d spatial frequency vectors. $\Delta\mathbf{u}$ is a small, constant offset spatial frequency.

This technique consists of evaluating the three sub-planes in Fourier space corresponding to $\Delta\mathbf{u} = \Delta\mathbf{u}_x$, $\Delta\mathbf{u} = \Delta\mathbf{u}_y$, $\Delta\mathbf{u} = \Delta\mathbf{u}_y + \Delta\mathbf{u}_x$. If digitized images are used, $\Delta\mathbf{u}$ normally corresponds to the fundamental sampling vector interval (Knox, 1976). A number of sub-planes can be used by using different values of $\Delta\mathbf{u}$. Invoking equation (69), into equation (92), the following relationship can be found as,

$$\widehat{\mathcal{I}}(\mathbf{u}_1)\widehat{\mathcal{I}}^*(\mathbf{u}_1 + \Delta\mathbf{u}) = \widehat{\mathcal{O}}(\mathbf{u}_1)\widehat{\mathcal{O}}^*(\mathbf{u}_1 + \Delta\mathbf{u})\widehat{\mathcal{S}}(\mathbf{u}_1)\widehat{\mathcal{S}}^*(\mathbf{u}_1 + \Delta\mathbf{u}). \tag{93}$$

The argument of the equation (92) provides the phase-difference between the two spatial frequencies separated by $\Delta\mathbf{u}$ and can be expressed as,

$$arg \mid \widehat{\mathcal{I}}^{KT}(\mathbf{u}_1, \Delta\mathbf{u}) \mid = \theta^{KT}(\mathbf{u}_1, \Delta\mathbf{u}) = \psi(\mathbf{u}_1) - \psi(\mathbf{u}_1 + \Delta\mathbf{u}). \tag{94}$$

The equation (93) can be expressed as,

$$\widehat{\mathcal{I}}(\mathbf{u}_1)$$

$$= \mid \widehat{\mathcal{O}}(\mathbf{u}_1) \mid\mid \widehat{\mathcal{O}}(\mathbf{u}_1 + \Delta\mathbf{u}) \mid\mid \widehat{\mathcal{S}}(\mathbf{u}_1) \mid\mid \widehat{\mathcal{S}}(\mathbf{u}_1 + \Delta\mathbf{u}) \mid e^{i[\theta_{\mathcal{O}}^{KT}(\mathbf{u}_1, \Delta\mathbf{u}) + \theta_{\mathcal{S}}^{KT}(\mathbf{u}_1, \Delta\mathbf{u})]}. \tag{95}$$

The difference in phase between points in the object phase-spectrum is encoded in the term, $e^{i\theta_{\mathcal{O}}^{KT}(\mathbf{u}_1, \Delta\mathbf{u})} = e^{i[\psi_{\mathcal{O}}(\mathbf{u}_1) - \psi_{\mathcal{O}}(\mathbf{u}_1 + \Delta\mathbf{u})]}$ of the equation (95). In a single image realization the object phase-difference is corrupted by the random phase-differences due to the atmosphere-telescope OTF, $e^{i\theta_{\mathcal{S}}^{KT}(\mathbf{u}_1, \Delta\mathbf{u})} = e^{i[\psi_{\mathcal{S}}(\mathbf{u}_1) - \psi_{\mathcal{S}}(\mathbf{u}_1 + \Delta\mathbf{u})]}$. If equation (94) is averaged over a large number of frames, the feature $(\Delta\psi_{\mathcal{S}}) = 0$. When $\Delta\mathbf{u}$ is small, $\mid \widehat{\mathcal{O}}(\mathbf{u}_1 + \Delta\mathbf{u}) \mid \approx \mid \widehat{\mathcal{O}}(\mathbf{u}_1) \mid$, etc. and so,

$$< \widehat{\mathcal{I}}(\mathbf{u}_1, \Delta\mathbf{u}) >$$

$$= \mid \widehat{\mathcal{O}}(\mathbf{u}_1) \mid\mid \widehat{\mathcal{O}}(\mathbf{u}_1 + \Delta\mathbf{u}) \mid e^{i[\theta_{\mathcal{O}}^{KT}(\mathbf{u}_1, \Delta\mathbf{u})]} < \widehat{\mathcal{S}}(\mathbf{u}_1)\widehat{\mathcal{S}}^*(\mathbf{u}_1 + \Delta\mathbf{u}) >, \tag{96}$$

from which, together with equation (70), the object phase-spectrum, $\theta_{\mathcal{O}}^{KT}(\mathbf{u}_1, \Delta\mathbf{u})$, can be determined. This technique is found to be sensitive to odd order aberrations, e.g., coma but not defocusing, astigmatism, spherical etc., (Barakat and Nisenson, 1981).

6.4. Triple Correlation Technique (TC)

The triple correlation technique or speckle masking method (Weigelt, 1977, Lohmann et al., 1983) is based on the closure phase (section 4.6) that remains uncorrupted in the presence of atmospheric turbulence and is being widely applied to improve the resolution of night-time objects (Cruzalébes et al., 1996, Falcke et al., 1996, Osterbart et al., 1996, Weigelt et al., 1996, Saha et al., 1999b, 1999c), as well as to the extended objects (Beletic, 1988, Von der Lühe and Pehlemann, 1988, Max, 1994, Denker, 1998, Sridharan and Venkatakrishnan, 1999). The advantages of this technique are: (i) it provides information about the object phases with better S/N ratio from a limited number of frames, and (ii) it serves as the means for recovery with diluted coherent arrays (Reinheimer and Weigelt, 1987) owing to its relationship with the phase closure technique (section 4.6) used in radio astronomy (Roddier, 1986, Cornwell 1987). The disadvantage of this technique is that of demanding very severe constraints on the computing facilities with 2-d data since the calculations are 4-dimensional (4-d) (see equations 98, 100). It requires extensive evaluation-time and data storage requirements, if the correlations are performed by using digitized images on a computer.

Unlike in shift-and-add where, a Dirac impulse at the centre of gravity of each speckle is put to estimate the same, Weigelt, (1977), suggested to multiply the object speckle pattern $\mathcal{I}(\mathbf{x})$ by an appropriately shifted version of this $\mathcal{I}(\mathbf{x}+\mathbf{x}_1)$. The result is correlated with $\mathcal{I}(\mathbf{x})$. (For example, in the case of a close binary star, the shift is equal to the angular separation between the stars, masking one of the two components of each double speckle).

The bispectrum planes are obtained as an intermediate step, contain phase information encoded by correlating $\mathcal{I}(\mathbf{x})$ with $\mathcal{I}(\mathbf{x})$ multiplied by complex exponentials with higher spatial frequencies. The calculation of the ensemble average TC is given by,

$$\mathcal{I}(\mathbf{x}_1, \mathbf{x}_2) = < \int_{-\infty}^{+\infty} \mathcal{I}(\mathbf{x})\mathcal{I}(\mathbf{x}+\mathbf{x}_1)\mathcal{I}(\mathbf{x}+\mathbf{x}_2)d\mathbf{x} >, \tag{97}$$

where, $\mathbf{x}_j = \mathbf{x}_{jx} + \mathbf{x}_{jy}$ are 2-d spatial co-ordinate vectors.

The Fourier transform of the triple correlation is called bispectrum and its ensemble average is given by,

$$\widehat{\mathcal{I}}(\mathbf{u}_1, \mathbf{u}_2) = < \widehat{\mathcal{I}}(\mathbf{u}_1)\widehat{\mathcal{I}}^*(\mathbf{u}_1+\mathbf{u}_2)\widehat{\mathcal{I}}(\mathbf{u}_2) >, \tag{98}$$

where, $\mathbf{u}_j = \mathbf{u}_{jx} + \mathbf{u}_{jy}, \widehat{\mathcal{I}}(\mathbf{u}_j) = \int \mathcal{I}(\mathbf{x})e^{-i2\pi\mathbf{u}_j\mathbf{x}}d\mathbf{x}, \widehat{\mathcal{I}}^*(\mathbf{u}_1+\mathbf{u}_2) = \int \mathcal{I}(\mathbf{x})e^{i2\pi(\mathbf{u}_1+\mathbf{u}_2)\cdot\mathbf{x}}d\mathbf{x}$.

In the second order moment or in the energy spectrum, phase of the object's Fourier transform is lost, but in the third order moment or in the bispectrum it is preserved. The argument of equation (98) can be expressed as,

490 S. K. Saha

$$arg \mid \widehat{\mathcal{I}}^{TC}(\mathbf{u}_1, \mathbf{u}_2) \mid = \theta^{TC}(\mathbf{u}_1, \mathbf{u}_2) = \psi(\mathbf{u}_1) - \psi(\mathbf{u}_1 + \mathbf{u}_2) + \psi(\mathbf{u}_2). \qquad (99)$$

Equation (99) gives the phase-difference. Invoking equation (69) into equation (97), it emerges as,

$$\widehat{\mathcal{I}}(\mathbf{u}_1, \mathbf{u}_2) = \widehat{\mathcal{O}}(\mathbf{u}_1)\widehat{\mathcal{O}}^*(\mathbf{u}_1 + \mathbf{u}_2)\widehat{\mathcal{O}}(\mathbf{u}_2) < \widehat{\mathcal{S}}(\mathbf{u}_1)\widehat{\mathcal{S}}^*(\mathbf{u}_1 + \mathbf{u}_2)\widehat{\mathcal{S}}(\mathbf{u}_2) > . \qquad (100)$$

The relationship implies that the image bispectrum is equal to the object bispectrum times a bispectrum transfer function, $< \widehat{\mathcal{S}}(\mathbf{u}_1)\widehat{\mathcal{S}}^*(\mathbf{u}_1 + \mathbf{u}_2)\widehat{\mathcal{S}}(\mathbf{u}_2) >$. The object bispectrum is given by,

$$\widehat{\mathcal{I}}_{\mathcal{O}}(\mathbf{u}_1, \mathbf{u}_2) = \widehat{\mathcal{O}}(\mathbf{u}_1)\widehat{\mathcal{O}}^*(\mathbf{u}_1 + \mathbf{u}_2)\widehat{\mathcal{O}}(\mathbf{u}_2) = \frac{< \widehat{\mathcal{I}}(\mathbf{u}_1)\widehat{\mathcal{I}}^*(\mathbf{u}_1 + \mathbf{u}_2)\widehat{\mathcal{I}}(\mathbf{u}_2) >}{< \widehat{\mathcal{S}}(\mathbf{u}_1)\widehat{\mathcal{S}}^*(\mathbf{u}_1 + \mathbf{u}_2)\widehat{\mathcal{S}}(\mathbf{u}_2) >}. \qquad (101)$$

The modulus $\mid \widehat{\mathcal{O}}(\mathbf{u}) \mid$ and phase $\psi(\mathbf{u})$ of the object Fourier transform $\widehat{\mathcal{O}}(\mathbf{u})$ can be evaluated from the object bispectrum $\widehat{\mathcal{I}}_{\mathcal{O}}(\mathbf{u}_1, \mathbf{u}_2)$ (Weigelt, 1988). The object phase-spectrum, is encoded in the term, $e^{i\theta_{\mathcal{O}}^{TC}(\mathbf{u}_1, \mathbf{u}_2)} = e^{i[\psi_{\mathcal{O}}(\mathbf{u}_1) - \psi_{\mathcal{O}}(\mathbf{u}_1 + \mathbf{u}_2) + \psi_{\mathcal{O}}(\mathbf{u}_2)]}$, of equation (98).

The S/N ratio of the phase recovery contains S/N ratio for bispectrum, as well as a factor representing improvement due to redundancy of phase-information stored in the bispectrum. Karbelkar and Nityananda, (1987) showed that the calculation of Wirnitzer (1985), in the wave limit true for bright objects, the S/N ratio for the bispectrum over-estimated by a factor of the order of the square root of the number of speckles. The bispectrum method has been tested with a computer simulated image by using a code developed by Saha et al., (1999b). Figure 9 depicts (a) simulated binary system, (b) 2-d representation of a 4-d bispectrum, (c) triple correlation and (d) reconstructed image of the same binary system.

The object phase-difference is corrupted by the random phase-differences due to the atmosphere-telescope OTF, $e^{i\theta_s^{TC}(\mathbf{u}_1, \mathbf{u}_2)} = e^{i[\psi_s(\mathbf{u}_1) - \psi_s(\mathbf{u}_1 + \mathbf{u}_2) + \psi_s(\mathbf{u}_2)]}$, in a single image realization. If a sufficient number of specklegrams are averaged, one can overcome this shortcoming. Let $\theta_{\mathcal{O}}^{TC}(\mathbf{u}_1, \mathbf{u}_2)$ be the phase of the object bispectrum; then,

$$\widehat{\mathcal{O}}(\mathbf{u}) = \mid \widehat{\mathcal{O}}(\mathbf{u}) \mid e^{i\psi(\mathbf{u})}, \qquad (102)$$

and

$$\widehat{\mathcal{I}}_{\mathcal{O}}(\mathbf{u}_1, \mathbf{u}_2) = \mid \widehat{\mathcal{I}}_{\mathcal{O}}(\mathbf{u}_1, \mathbf{u}_2) \mid e^{i\theta_{\mathcal{O}}^{TC}(\mathbf{u}_1, \mathbf{u}_2)}. \qquad (103)$$

Equations (102) and (103) may be inserted into equation (101), yielding the relations,
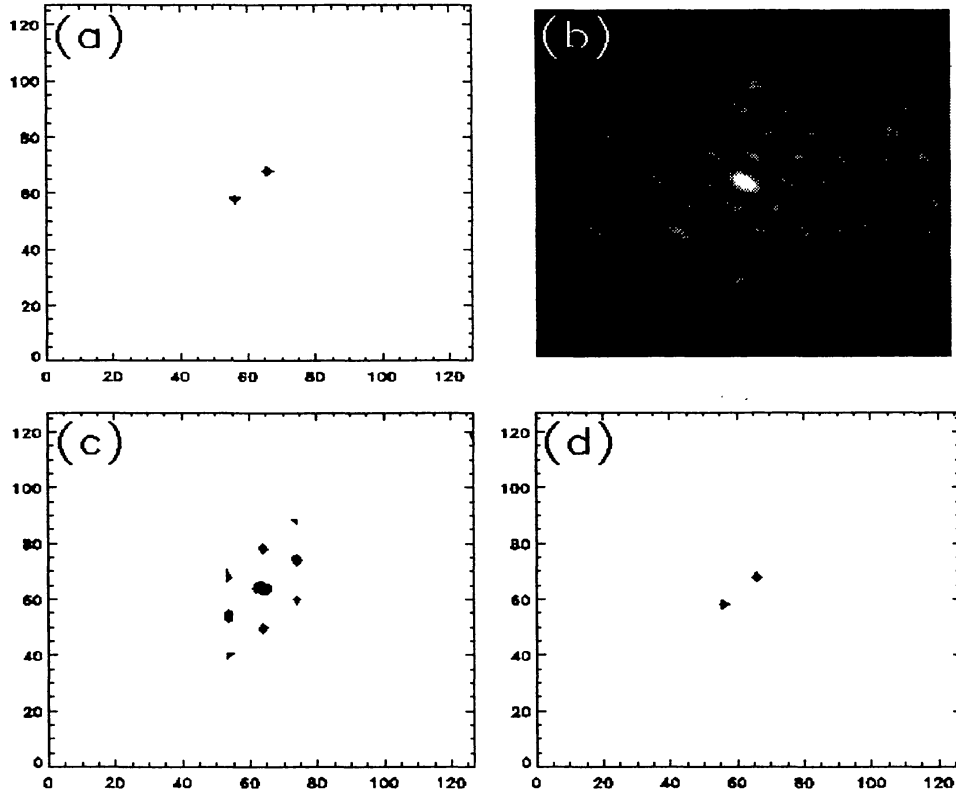
Figure 9. (a) 2-d maps of a simulated binary system, (b) 2-d representation of its 4-d bispectrum, (c) its triple correlation and (d) its reconstructed image.

$$\widehat{\mathcal{I}}_{\mathcal{O}}(\mathbf{u}_1, \mathbf{u}_2)$$

$$=| \ \widehat{\mathcal{O}}(\mathbf{u}_1) \ || \ \widehat{\mathcal{O}}(\mathbf{u}_2) \ || \ \widehat{\mathcal{O}}(\mathbf{u}_1 + \mathbf{u}_2) \ | \ e^{i[\psi_{\mathcal{O}}(\mathbf{u}_1) - \psi_{\mathcal{O}}(\mathbf{u}_1+\mathbf{u}_2) + \psi_{\mathcal{O}}(\mathbf{u}_2)]} \rightarrow, \tag{104}$$

$$\theta_{\mathcal{O}}^{TC}(\mathbf{u}_1, \mathbf{u}_2) = \psi_{\mathcal{O}}(\mathbf{u}_1) - \psi_{\mathcal{O}}(\mathbf{u}_1 + \mathbf{u}_2) + \psi_{\mathcal{O}}(\mathbf{u}_2). \tag{105}$$

Equation (105) is a recursive equation for evaluating the phase of the object Fourier transform at coordinate $\mathbf{u} = \mathbf{u}_1 + \mathbf{u}_2$ (Weigelt, 1988). The reconstruction of the object phase-spectrum from the phase of the bispectrum is recursive in nature. The object phase-spectrum at $(\mathbf{u}_1 + \mathbf{u}_2)$ can be expressed as,

$$\psi_{\mathcal{O}}(\mathbf{u}_1 + \mathbf{u}_2) = \psi_{\mathcal{O}}(\mathbf{u}) = \psi_{\mathcal{O}}(\mathbf{u}_1) + \psi_{\mathcal{O}}(\mathbf{u}_2) - \theta_{\mathcal{O}}^{TC}(\mathbf{u}_1, \mathbf{u}_2). \tag{106}$$

If the object spectrum at $\mathbf{u}_1$ and $\mathbf{u}_2$ is known, the object phase-spectrum at $(\mathbf{u}_1 + \mathbf{u}_2)$ can be computed. The bispectrum phases are mod 2π, therefore, the recursive reconstruction in equation (105) may lead to π phase mismatches between the computed phase-spectrum values along different paths to the same point in frequency space. Northcott

et al., (1988) opined that phases from different paths to the same cannot be averaged to reduce noise under this condition. A variation of the nature of computing argument of the term, $e^{i\psi_O(\mathbf{u}_1+\mathbf{u}_2)}$, is needed to obtain the object phase-spectrum and the equation (106) can be translated to,

$$e^{i\psi_O(\mathbf{u}_1+\mathbf{u}_2)} = e^{i[\psi_O(\mathbf{u}_1)+\psi_O(\mathbf{u}_2)-\theta_O^{TC}(\mathbf{u}_1,\mathbf{u}_2)]}. \tag{107}$$

The values obtained using the unit amplitude phasor recursive re-constructor (see equation 106) are insensitive to the π phase ambiguities and has been used by several investigators in studies of the bispectrum technique (Ayers et al., 1988, Northcott et al., 1988, Meng et al., 1990, Matson, 1991, Lawrence et al., 1992). Saha et al., (1999b, 1999c) have developed a code based on the unit amplitude phasor recursive re-constructor. The algorithm written in Interactive Data Language (IDL) takes about an hour for processing 10 frames of size 128×128 using the SPARC ULTRA workstation. The memory needed for the calculation exceeds 160 MB if the array size is more than the said number. Since the bispectrum is a 4-dimensional function, it is difficult to represent it in a 3-dimensional co-ordinate system. Therefore, they have stored the calculated values in 1-dimensional array and used later to calculate the phase by keeping track of the component frequencies (Saha et al., 1999b). For example, let $\psi(u_1, u_2)$ be the phase corresponding to the frequency, (u_1, u_2) and θ_O^{TC} be the phase of the bispectrum. Assuming $\psi(0,0) = 0, \psi(0,\pm1) = 0$ and $\psi(\pm1, 0) = 0$, the phases are calculated by the unitary amplitude method. Saha et al., (1999b) have successfully determined the phase from the average bispectrum of the specklegrams of a couple of stars.

Like the phase-closure (see section 4.6), the bispectrum is insensitive to the atmospherically induced random phase errors, as well as to random motion of the image centroid; therefore, images are not required to be shifted to common centroid prior to computing the bispectrum. Further development of phase reconstruction from the bispectrum can be seen in the form of (i) a least-square formulation of the phase reconstruction (Meng et al., 1990, Glindemann et al., 1991, 1992), and (ii) a projection-slice theorem of tomography and the Radon transform (Northcott et al., 1988). Matson (1991) has developed two weighted least-squares estimation formulations of the phase reconstructions problem. However, most of the results, using the real data are limited to the recursive phase reconstruction (Weigelt, 1988 and references therein, Weigelt et al., 1996).

6.4.1. Relationship between KT and TC

Ayers et al., (1988) have illustrated the relationship of two of the widely used algorithms, namely, KT and TC methods, which runs as follows.

Substituting $\mathbf{u}_2 = \Delta\mathbf{u}$ in equation (98), the single plane bispectrum can be expressed as,

$$\widehat{\mathcal{I}}^{TC}(\mathbf{u}_1, \Delta\mathbf{u}) = \widehat{\mathcal{I}}(\mathbf{u}_1)\widehat{\mathcal{I}}^*(\mathbf{u}_1 + \Delta\mathbf{u})\widehat{\mathcal{I}}(\Delta\mathbf{u}). \tag{108}$$

In the image space, the expression becomes,

$$\mathcal{I}^{TC}(\mathbf{x}_1, \Delta\mathbf{u}) = \widehat{\mathcal{I}}(\Delta\mathbf{u}) \int_{-\infty}^{+\infty} \mathcal{I}^*(\mathbf{x})\mathcal{I}(\mathbf{x}+\mathbf{x}_1)e^{i2\pi\Delta\mathbf{u}\mathbf{x}}d\mathbf{x}$$

$$= \widehat{\mathcal{I}}(\Delta\mathbf{u})I^{KT}(\mathbf{x}_1, \Delta\mathbf{u}). \tag{109}$$

Between the two equations (92) and (109), it is seen that for a spatial frequency difference, $\Delta\mathbf{u}$, the bispectrum plane corresponds to a weighted version, a signal depending factor, of the KT product in Fourier space. On comparing equations (94) and (99), the shift invariant property of the bispectrum can be expressed as,

$$\theta^{TC}(\mathbf{u}_1, \Delta u) = \theta^{KT}(\mathbf{u}_1, \Delta\mathbf{u}) + \psi(\Delta\mathbf{u}). \tag{110}$$

In the KT method, the transform $\widehat{\mathcal{I}}(\mathbf{u})$ interferes with itself after translation by a small shift vector $\Delta\mathbf{u}$. Figure 10 depicts the diagrammatic representation of pupil sub-apertures of diameter r_o; (a) approximate phase-closure is achieved in KT method, and (b) complete phase-closure in TC method.

(a)

(b)
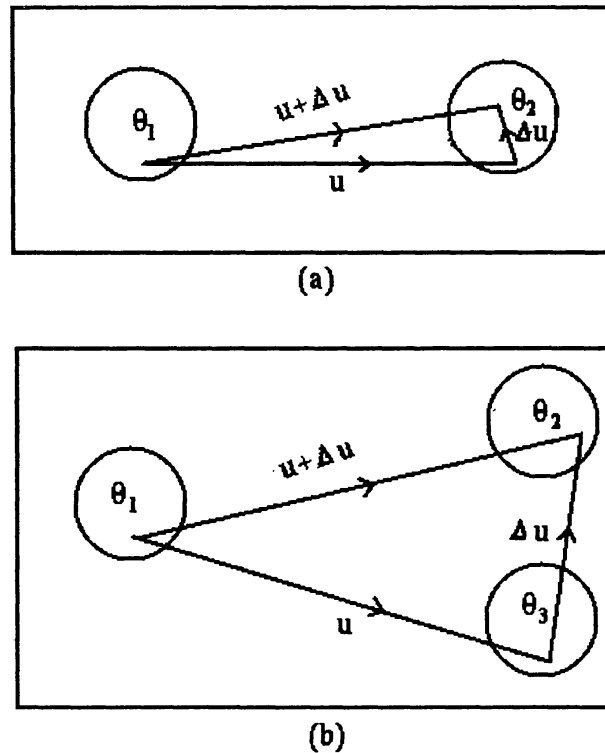
Figure 10. Pupil sub-apertures of diameter r_o, (a) approximate phase-closure achieved in KT method, (b) while complete phase-closure is achieved in TC method.

The approximate phase-closure in this case is achieved by two vectors, $\mathbf{u}$ and $\mathbf{u} + \Delta\mathbf{u}$, assuming that the pupil phase is constant over $\Delta\mathbf{u}$. The major Fourier component of the fringe pattern is averaged with a component at a frequency displaced by $\Delta\mathbf{u}$. If this vector does not force the vector difference $-\mathbf{u} - \Delta\mathbf{u}$ to be outside the spatial frequency bandwidth of the fringe pattern, it preserves the Fourier phase-difference information in the averaged signal. The atmospheric phase effectively forms a closed loop.

$$arg \mid \widehat{\mathcal{I}}(\mathbf{u})\widehat{\mathcal{I}}(-\mathbf{u} - \Delta\mathbf{u}) \mid = \psi(\mathbf{u}) + \theta_1 - \theta_2 + \psi(-\mathbf{u} - \Delta\mathbf{u}) - \theta_1 + \theta_2, \quad (111)$$

$$= \psi(\mathbf{u}) - \psi(\mathbf{u} + \Delta\mathbf{u}), \quad (112)$$

$$< \widehat{\mathcal{I}}(\mathbf{u})\widehat{\mathcal{I}}(-\mathbf{u} - \Delta\mathbf{u}) > \neq 0, \quad \Delta u < r_o/\lambda. \quad (113)$$

Let this system of two apertures be extended to 3 and the $\Delta u > r_o/\lambda$, then,

$$arg \mid \widehat{\mathcal{I}}(\mathbf{u})\widehat{\mathcal{I}}(-\mathbf{u} - \Delta\mathbf{u}) \mid = \psi(\mathbf{u}) + \theta_1 - \theta_2 - \psi(-\mathbf{u} - \Delta\mathbf{u}) - \theta_1 + \theta_3$$

$$= \psi(\mathbf{u}) - \psi(\mathbf{u} + \Delta\mathbf{u}) - \theta_2 + \theta_3, \quad (114)$$

$$< \widehat{\mathcal{I}}(\mathbf{u})\widehat{\mathcal{I}}(-\mathbf{u} - \Delta\mathbf{u}) > = 0, \quad \Delta u < r_o/\lambda. \quad (115)$$

The atmospheric phase contribution is not closed in this case. KT is limited to frequency differences $\Delta u < r_o/\lambda$. In the bispectrum method, a third vector, $\Delta\mathbf{u} > r_o/\lambda$, is added to form phase-closure. When $\lambda\Delta\mathbf{u} > r_o$, the third vector is essential; the KT method fails with this arrangement. If the bispectrum average is performed, the phase is closed and Fourier phase-difference information is preserved.

$$arg \mid \widehat{\mathcal{I}}(\mathbf{u})\widehat{\mathcal{I}}(\Delta\mathbf{u})\widehat{\mathcal{I}}(-\mathbf{u} - \Delta\mathbf{u}) \mid$$

$$= \psi(u) + \theta_1 - \theta_2 + \psi(\Delta\mathbf{u}) + \theta_2 - \theta_3 + \psi(-\mathbf{u} - \Delta\mathbf{u}) - \theta_1 + \theta_3$$

$$= \psi(\mathbf{u}) - \psi(\mathbf{u} + \Delta\mathbf{u}) + \psi(\Delta\mathbf{u}). \quad (116)$$

Thus, the bispectrum method can give phase information for phase-differences $\Delta u > r_o/\lambda$. TC method is similar to the phase-closure technique. Closure phases are insensitive to the atmospherically induced random phase errors, as well as to the permanent phase errors introduced by telescope aberrations. Any linear phase term in the object phase cancels out in the closure phase. In the case of a TC method, the information resides within isolated patches in Fourier space, while the KT method is not applicable under these conditions.

A comparative study was made by Weitzel et al., (1992) with the real data and concluded that KT and TC (bispectrum) give the same results for a binary system with a separation greater than the diffraction limit of the telescope. But they found some improvement for a binary system at a separation about the telescope diffraction limit in applying bispectrum method.

6.5. Blind iterative deconvolution technique (BID)

The blind iterative deconvolution (BID) technique combines constrained iterative techniques (Gerchberg and Saxton, 1972, Fienup, 1978) with blind deconvolution (Lane and Bates, 1987). Essentially, it consists of using very limited information about the image, like positivity and image size, to iteratively arrive at a deconvolved image of the object, starting from a blind guess of either the object or both the convolving function. The iterative loop is repeated enforcing image-domain and Fourier-domain constraints until two images are found that produce the input image when convolved together (Bates and McDonnell, 1986, Ayers and Dainty, 1988, Bates and Davey, 1988). The image-domain constraints of non-negativity is generally used in iterative algorithms associated with optical processing to find effective supports of the object and or PSF from a specklegram. The implementation of the algorithm of BID developed by Nisenson, (1992) runs as follows.

The algorithm has the degraded image, $\mathcal{I}(\mathbf{x})$, as the operand. An initial estimate of the PSF, $\mathcal{S}(\mathbf{x})$, has to be provided. The degraded image is deconvolved from the guess PSF by Wiener filtering, which is an operation of multiplying a suitable Wiener filter (constructed from the Fourier transform, $\widehat{\mathcal{S}}(\mathbf{u})$, of the PSF) with the Fourier transform, $\widehat{\mathcal{I}}(\mathbf{u})$, of the degraded image. The technique of Wiener filtering damps the high frequencies and minimizes the mean square error between each estimate and the true spectrum. The Wiener filtering spectrum, $\widehat{\mathcal{O}}(\mathbf{u})$, takes the form:

$$\widehat{\mathcal{O}}(\mathbf{u}) = \widehat{\mathcal{I}}(\mathbf{u}) \frac{\widehat{\mathcal{S}}^*(\mathbf{u})}{\widehat{\mathcal{S}}(\mathbf{u})\widehat{\mathcal{S}}^*(\mathbf{u}) + \widehat{\mathcal{N}}(\mathbf{u})\widehat{\mathcal{N}}^*(\mathbf{u})}. \tag{117}$$

The noise term, $\widehat{\mathcal{N}}(\mathbf{u})$ can be replaced with a constant estimated as the rms fluctuation of the high frequency region in the spectrum where the object power is negligible. The result, $\widehat{\mathcal{O}}(\mathbf{u})$, is transformed back to image space, the negatives in the image and the positives outside a prescribed domain (called object support) are set to zero. The average of negative intensities within the support are subtracted from all pixels. The process is repeated until the negative intensities decrease below the noise. A new estimate of the PSF is next obtained by Wiener filtering the original image, $\mathcal{I}(\mathbf{x})$, with a filter constructed from the constrained object, $\mathcal{O}(\mathbf{x})$; this completes one iteration. This entire process is repeated until the derived values of $\mathcal{O}(\mathbf{x})$ and $\mathcal{S}(\mathbf{x})$ converge to sensible solutions.

The comparative analysis of the recovery reveals that both the morphology and the relative intensities are present in the retrieved diffraction-limited image and PSF. The results are vulnerable to the choice of various parameters like the support radius, the level of high frequency suppression during the Wiener filtering, etc. The availability of prior knowledge on the object through autocorrelation of the degraded image is very useful for specifying the object support radius (Saha and Venkatakrishnan, 1997, Saha, 1999). Jefferies and Christou, (1993), have developed an algorithm which requires more than a single speckle frame for improving the convergence.

A major advantage of the BID compared with the rest of the methods described above is the ability to retrieve the diffraction-limited image of an object from a single specklegram without the reference star data. Often, it may not be possible to gather a sufficient number of images within the time interval over which the statistics of the atmospheric turbulence remains stationary.

Though BID requires high S/N ratios in the data, it appears to be a powerful tool for image restoration. The restoration for speckle data at the 12th magnitude level assuming 15% photo-cathode sensitivity of the detector had been demonstrated (Nisenson et al., 1990). Nisenson, (1992) opined that the technique can be improved by using multiple frames simultaneously as convergence constraints which may help in extending the magnitude level to fainter ($m_v > 12$). This technique is indeed an ideal one to process the degraded images of extended objects, viz., (i) Planets (Saha et al., 1997c), and (ii) Sun (Nisenson 1992).

7. Speckle imaging of extended objects

Thus far, the discussions revolved around obtaining diffraction-limited informations of the stellar point sources. Reconstructions of high resolution features on the extended objects, viz., (i) Jupiter, (ii) Sun, were also made with interferometric techniques. The techniques for obtaining deconvolved images with sub-arc-second resolution of these extended objects are illustrated below.

7.1. Jupiter

Speckle interferometric technique was used to record the images of Jupiter during the collision of the fragments of comet Shoemaker-Levy 9 (1993e) with the former during July 16-22, 1994. At Lick observatory, the 3 m telescope equipped with speckle camera based on a bare CCD (roughly 1000×1000) with a pixel scale of $0.066''$/pixel was used to image (each with 100 - 500 ms exposures) the said planet through several filters during the said period (Max, 1994). They used the bispectral reconstruction technique to retrieve the deconvolved image so as to achieve about $0.2 - 0.4''$ resolution.

Large number of specklegrams of Jupiter in the visible band were recorded by Saha et al., (1997c), during the said period, at the Nasmyth focus of the 1.2 m telescope of Japal-Rangapur Observatory (JRO), Hyderabad. The interferometer developed for this purpose (Saha et al., 1997c) is depicted in figure 11. The image scale at the Nasmyth focus (f/13.7) of this telescope was enlarged by a Barlow lens arrangement, with a sampling of $0.11''$/pixel of the CCD. A set of 3 filters were used to image Jupiter, viz., (i) centred at 550 nm, with FWHM of 30 nm, (ii) centred at 611 nm, with FWHM of 9.9 nm and (iii) RG 9 with a lower wavelength cut-off at 800 nm (Saha et al., 1997c). A water-cooled bare 1024×1024 CCD was used as detector to record specklegrams of entire planetary disk of Jupiter with exposure times of 100 - 200 ms.
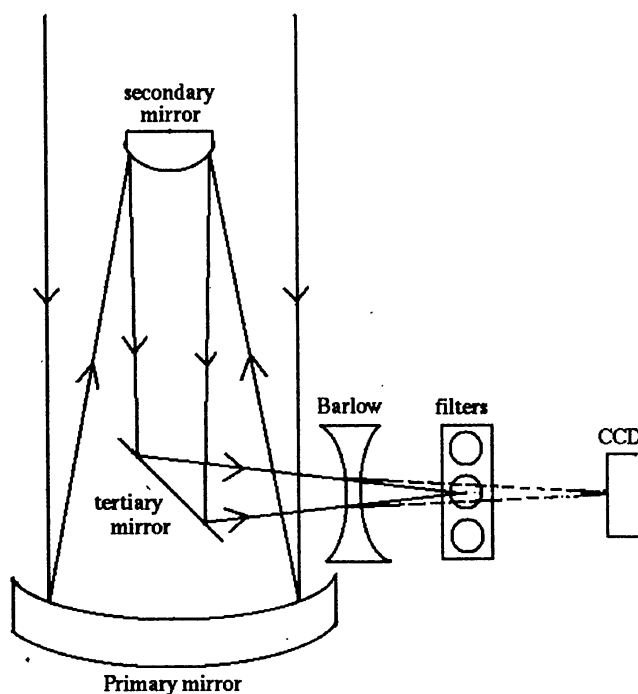
Figure 11. Experimental set-up of the interferometer to record the images of Jupiter (Saha et al., 1997c).

Saha et al., (1997c) have identified the complex spots due to impacts by the fragments using the technique of BID. The reconstructed image of Jupiter is shown in figure 12. The chief results of the construction is the enhancement in the contrast of spots. The complex spots in the East are due to impacts by fragments Q, R, S, D, G and the spots close to the centre are due to K and L impacts.

7.2. Sun

Interferometric techniques can bring out the high resolution informations of the fundamental processes on the Sun that take place on sub-arc-second scales concerning with convection and with magnetic fields (Von der Lühe and Zirker, 1988). Several investigators (Harvey, 1972, Harvey and Breckinridge, 1973, Harvey and Schwarzchild, 1975, Kinahan, 1975) found the existence of solar features with sizes of the order of 100 km or smaller by applying the interferometric technique to solar observation. Subsequently, solar granulation has been studied extensively with the said technique by many others (Aime et al., 1975, 1977, 1978, Aime, 1976, Ricort and Aime, 1979, Von der Lühe and Dunn, 1987). Solar small scale structure evolves fast and changes its position by about $0.1''$ within a fraction of a minute or so (Von der Lühe, 1989). The rapid evolution of

S. K. Saha
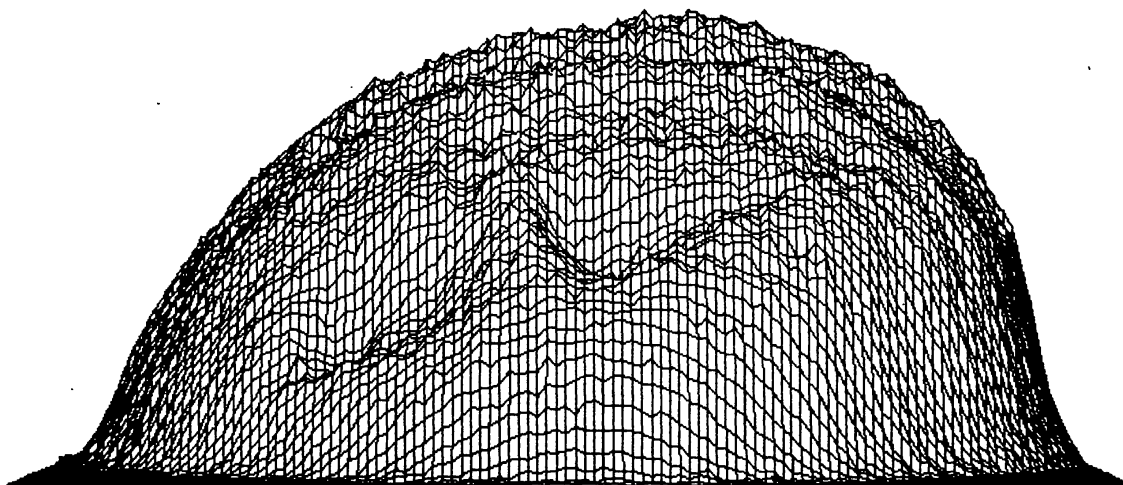
Figure 12. The deconvolved image of Jupiter (Saha et al., 1997c).

solar granulation prevents the detection of the long sequence of specklegrams for reconstruction, and therefore, the amount of time available for data accumulation is limited. Another limitation comes from the lack of efficient detectors to record a large amount of frames within the stipulated time before the structure changes.

From the observations of photospheric granulation from disc centre to limb at $\lambda = 550\pm5\,nm$, by means of speckle interferometric technique, at the Vacuum Tower Telescope (VTT), at the Observatorio del Teide (Tenerife), Wilken et al., (1997) found the decrease of the relative rms-contrast of the centre-to-limb of the granular intensity. Time series of high spatial resolution observations with the same telescope reveal the highly dynamical evolution of sunspot fine structures, namely, umbral dots, penumbral filaments, facular points (Denker, 1998). The small-scale brightenings in the vicinity of sunspots, were also observed in the wings of strong chromospheric absorption lines (Denker et al., 1995, Denker, 1998). These structures which are associated with strong magnetic fields show brightness variations close to the diffraction limit of the telescope ($\sim 0.16''$ at 550 nm).

To study the intensity enhancement in the inner line wings of Hα (656.28 nm), Denker et al (1995) used a speckle interferometer to obtain images of the solar chromosphere. The set-up consists of a field stop at the prime focus of the afore-mentioned telescope reducing stray-light, two achromats sampling $0.08''$/pixel of the detector, an interference filter with FWHM of 3 nm and the Universal Birefringes filter with FWHM of 0.1 nm or 0.05 nm (transparency amounts to 11% at Hα). A beam splitter was inserted in the light path to feed 90% light to the slow-scan CCD camera for speckle imaging and remaining light to the video CCD camera for guiding.

Magnetic fields in the solar photosphere are usually detected by measuring the polarization in the wing of a Zeeman spectral line. Keller and Von der Lühe (1992a, 1992b) applied differential speckle interferometric technique to solar polarimetry. This technique was used to image the quiet granulation, as well as to make polarimetric measurements of

a solar active region. The set-up used at the Swedish Vacuum Solar Telescope, La palma, consists of (i) an achromatic quarter-wave plate that transforms circularly polarized into linearly polarized light, (ii) two calcite plates rotated 90° relative to each other to ensure that two beams have identical path lengths, and (iii) a quarter-wave plate balancing the intensity in the two beams. The two beams are split up by a non-polarizing beam-splitter cube; one passes through a 8.2 nm FWHM interference filter centred at 520 nm and the other passes through a Zeiss tunable filter centred in the blue wing of FeI 525.02 nm with FWHM of about 0.015 nm. The former is used to determine the instantaneous PSF; CCD video cameras were used to detect these channels.

Keller and Johannesson (1995) have developed another method to obtain diffraction-limited spectrograms of sun consisting of speckle polarimetry technique (Keller and Von der Lühe, 1992b) and a rapid spectrograph (with a reflecting slit) scanning system (Johannesson et al., 1992). Two cameras record the spectrograms and 2-d slit-jaw images simultaneously. The slit of the spectrograph scans the solar surface during the observing run.

To reconstruct solar images, various image processing algorithms, viz., (i) Knox-Thomson technique, (ii) speckle masking method, (iii) the technique of BID, have been applied (Stachnik et al., 1977, 1983, Beletic, 1988, Von der Lühe and Pehlemann, 1988, Nisenson, 1992, Max, 1994, Denker et al., 1995, Keller and Johannesson, 1995, Wilken et al., 1997, Denker, 1998). But the major problem comes from estimating PSF in the case of Sun due to the lack of a reference point source, unlike stellar objects where this parameter can be determined from a nearby reference star. Von der Lühe (1984) proposed the spectral ratio technique based on a comparison between long and short-exposure images and this was employed by the observers (Denker et al., 1995, Wilken et al., 1997) to derive the Fried's parameter. The models of speckle transfer function (Korff, 1973) and of average short-exposure modulation transfer function (Fried, 1966) were applied to compare the observed spectral ratios with theoretical values. In this respect, the technique of BID, (see section 6.5), where a direct measurement of calibrating speckle transfer function is not required (Nisenson, 1992) has clear advantage over other techniques in retrieving the solar image.

7.2.1. Solar speckle observation during eclipse

The limb of the moon eclipsing the sun provides a sharp edge as a reference object during solar eclipses, and therefore, helps in estimating the seeing effects (Callados and Vàzquez, 1987). The intensity profile falls off sharply at the limb; the departure of this fall off gives an indirect estimate of the atmospheric PSF. Callados and Vàzquez, (1987) reported the measurement of PSF during the observation of solar eclipse of 30 May, 1984 using the 40 cm Newton Vacuum telescope at Observatorio dei Teide. Saha et al., (1997b) developed an exper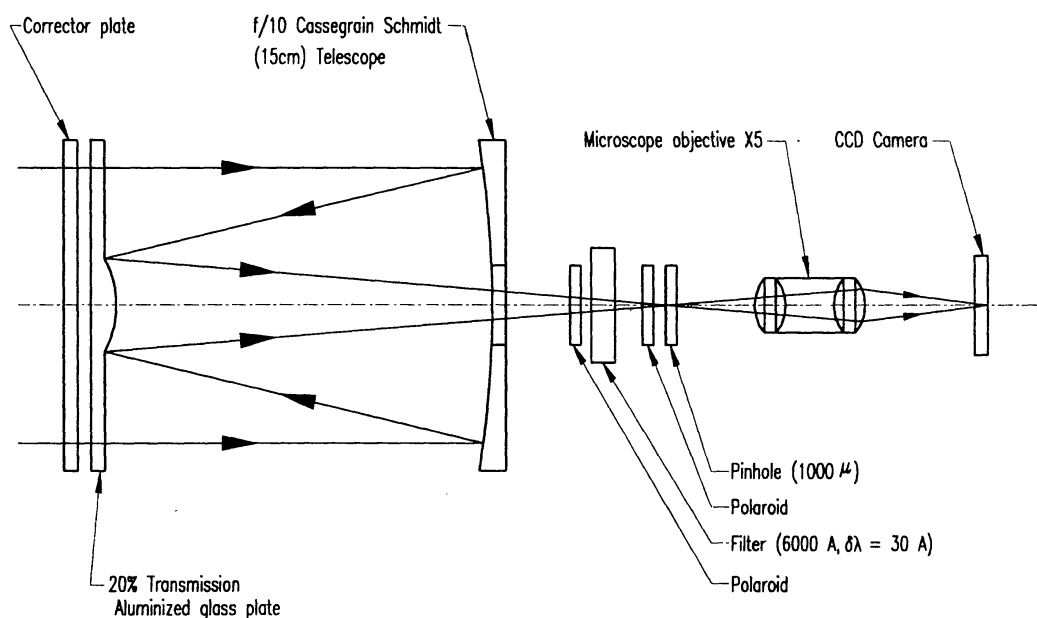iment for the speckle reconstruction of solar features during the partial eclipse of Sun as viewed from Bangalore on 24 October, 1995. The set-up is described as below.

A Carl-Zeiss 15 cm Cassegrain-Schmidt reflector was used as telescope fitted with an aluminised glass plate in front that transmits 20% and reflects the rest back. A pair of polaroids were placed in the converging beam ahead of the focal plane. A 3 nm passband filter centred at 600 nm was inserted between these polaroids. One of the polaroids was mounted on a rotatable holder (see figure 13), so as to adjust the amount of light falling onto the camera. A pin-hole of 1 mm diameter was set at the focal plane for isolating a small field-of-view. A microscope objective ($\times 5$) re-imaged this pin-hole onto the EEV CCD camera operated in the TV mode. The images were planned to be acquired with exposure time of 20 ms using a Data Translation^{TM} frame-grabber card DT-2861. Unfortunately, unfavourable weather conditions at Bangalore prevented in recording any data.

Figure 13. Schematic layout of the set-up for the speckle reconstruction of solar features during the partial eclipse of Sun as viewed from Bangalore on October 24th, 1995 (Saha et al., 1997b).

The image reconstruction involves the treatment of both amplitude errors, as well as phase errors. The 20 ms exposure time is small enough to preserve phase errors. Any of the schemes for phase reconstruction that satisfactorily reproduces the lunar limb would be valid for solar features close to the limb (within iso-planatic patch). Also, the limb reconstruction would be valid only for phase distortions along one direction (in a direction normal to the lunar limb). In spite of these shortcomings, the limb data would have provided additional constraints for techniques, like BID.

Another novel experiment was conducted by Koutchmy et al., 1994 using the modern 3.6 m CFHT telescope at Mauna-Kea during total solar eclipse of 11 July, 1991 to probe the solar corona. In this venture, several cameras combining fast photographic 70 mm

cameras and the video-CCD cameras were employed during the totality to acquire sub-arc-second spatial resolution white light images. Two video-CCD cameras, viz., (i) one fitted with a broad-band filter with $\times 2.5$ magnification ratio to record video frames during the totality so as to enable them to perform speckle interferometry image processing over the faintest coronal structures, and (ii) a second one with a 581×756 pixels CCD (size of the pixel = 11 μm) fitted with a narrow-band filter (λ = 637 nm, FWHM = 7 nm) to detect coronal radiation, were used. Fine-scale irregularities along coronal loops of very large aspect ratio were observed in a time series, confirming the presence of plasmoid-like activity in the inner corona.

Intensive computations are generally required in post-detection image restoration techniques in solar astronomy. The introduction of adaptive optics systems (see section 8) may, therefore, will be useful for spectroscopic observations, as well as for photon-starved imaging with future very large solar telescope. A few higher order solar adaptive optics systems are in use or under development (Beckers, 1999 and references therein). Images of sunspots on the solar surface were obtained with Lockheed adaptive optics system (Acton and Smithson, 1992) at the Sacramento Peak Vacuum telescope.

8. Adaptive optics

Adaptive optics (AO) removes the turbulence induced wave-front distortions by introducing an optical imaging system in the light path that performs two main functions: (i) sense the wave-front perturbations, and (ii) compensate for them in real time (Beckers, 1993, Roggemann et al., 1997). In other words, this system can introduce controllable counter wave-front distortion which both spatially and temporally follows that of the atmosphere. Although this technique was first proposed by Babcock (1953), it could not be implemented until recently due to the lack of technological advancement.

The components required to perform these functions are wave-front sensing, wave-front phase error computation and a flexible mirror whose surface can be electronically controlled in real time to create a conjugate surface enabling to compensate the wave-front distortion. Figure 14 depicts a schematic of the adaptive optics system. The principle of the AO system runs as follows. The beam from the telescope is collimated and fed to the tilt mirror to remove low frequency tilt errors. It travels further and is reflected from the deformable mirror after eliminating high frequency wave-front errors. This beam is split into two by introducing a beam-splitter; one is directed to the wave-front sensor and the other is focused to form an image. The former measures the residual error in the wave-front and provides information to the actuator control computer to compute the deformable mirror actuator voltages. This process should be at speeds commensurate with the rate of change of the corrugated wave-front phase errors.

The utility of the AO system is greatly enhanced by use of the laser guide star source (Foy and Labeyrie, 1985) as a reference to measure the wave-front errors by means of a wave-front sensor, as well as to map the phase on the entrance pupil. A pulsed laser is used to cause a bright compact glow in the upper atmosphere, which can serve as the
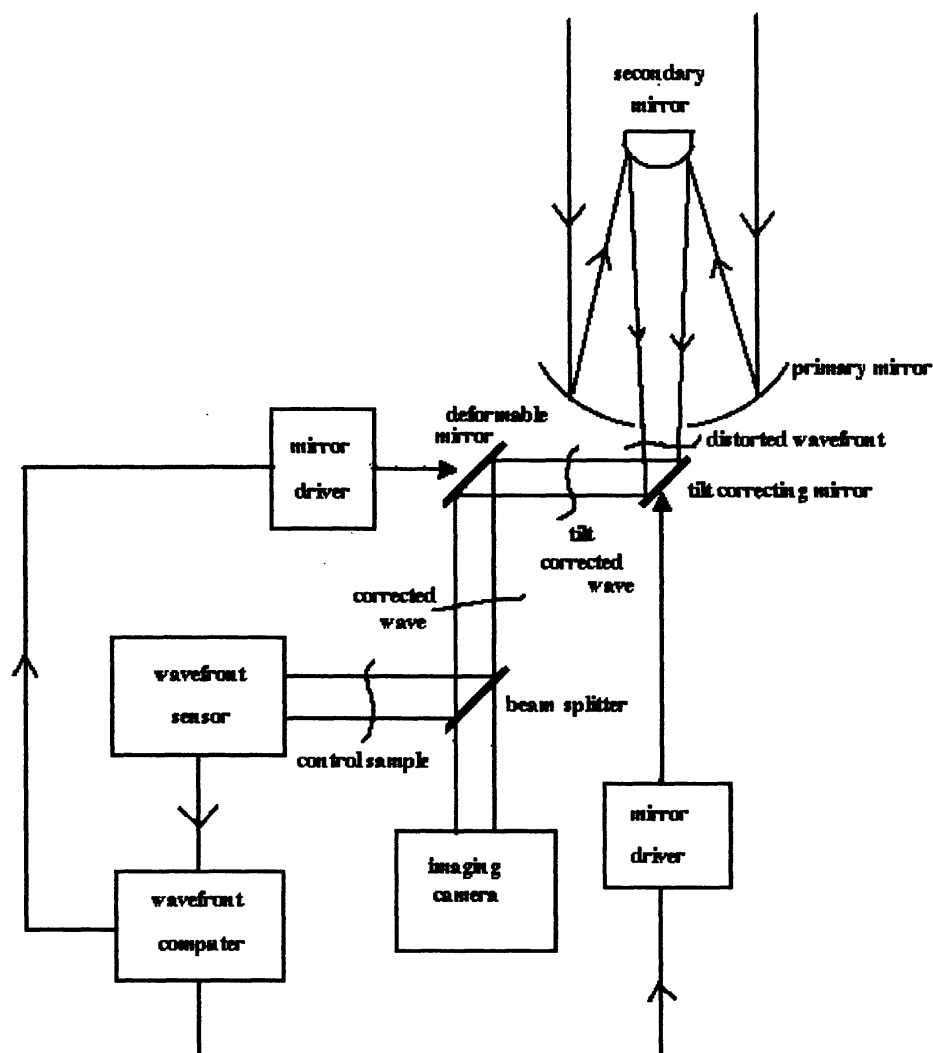
S. K. Saha

Figure 14. Schematic of the adaptive optics system.

source of measuring the turbulence of the atmosphere (Foy, 1996). Concerning the flux backscattered by a laser shot, Thompson and Gardnek (1988) stressed the importance of investigating two basic problems: (i) the cone effect which arises due to the parallax between the remote astronomical source and artificial source (located 90 km high in the case Na 1D laser), and (ii) the angular anisoplanatic effects. This can be restored by imaging the various turbulent layers of the atmosphere onto different adaptive mirrors (Foy and Labeyrie, 1985, Beckers, 1988, Tallon et al., 1988).

In the low order AO systems, the fast tip-tilt correctors or image stabilization devices are able to correct turbulence-induced image motions; the residual telescope tracking error also needs to be corrected. These systems are limited to two Zernicke modes (x

and y tilt), while higher order system compensating many Zernicke mode is required to remove high frequency errors. Glindemann, (1997) discussed the analytic formulae for the aberrations of the tip-tilt corrected wave-front as a function of the tracking algorithm and of the tracking frequency. A tip-tilt tertiary mirror system has been developed for the Calar Alto 3.5 m telescope, Spain, that corrects the rapid image motion (Glindemann et al., 1997). The following paragraphs are dedicated to the various types of wave-front sensors.

(i) The lateral shearing interferometer is used in AO system as wave-front sensor (Hardy et al., 1977, Sandler et al., 1994). The experimental details of the system can be found in section 4.5. The shearing interferometer based on BC (Saxena and Jayarajan, 1981, Saxena and Lancelot, 1981) was reported to be very compact and rugged to use. It is planned to use this as the sensor for the AO programmes at IIA, Bangalore (Chinnappan et al., 1998).

(ii) The Shack-Hartman sensor measures directly the angles of arrival, and therefore, works well with incoherent white light extended sources (Rousset, 1999 and references therein); it divides the pupil into sub-pupils (Wyant and Koliopoulos, 1981). This type of sensors have already been used in AO systems (Fugate et al., 1991, Primmerman et al., 1991). Tallon et al., (1988) have developed same type of set-up to record wave-front surface, where the beam at the focal plane of the telescope is transmitted through a nearly field lens to a collimating doublet objective and imaged the exit pupil of the former on to a lens-let mosaic which form an array of images on the detector. Each lens-let defines a sub-aperture in the telescope pupil. The position of the centre of gravity of this spot is directly related to the phase mean slope over the sub-aperture. Their positions are measured to give the full vectorial wave-front tilt in the areas of the pupil covered by each lens-let.

The dimensions of the lens-lets are often taken to correspond approximately to r_0, though Tallon and Foy (1990) suggested that depending on the number of turbulent layers, the size of the sub-pupils in this type of sensor can be made significantly larger than the latter. The value of r_0 varies over the duration of observation, therefore, a minimal number of lens-let array for a given aperture size is required. The test consists of recording the ray impacts in a plane slightly before the focal plane. If optics were perfect, the recorded spots would be exactly distributed as the position of lens-lets but on a smaller scale. Due to aberrations, light rays are deviated from their ideal direction, producing spot displacements; the amount of displacement is a measure of the deviation of the ray which, in turn, the deviation of the local wave-front slope.

(iii) The curvature sensor measures a signal proportional to the second derivative of the wave-front phase (Roddier, 1988c, 1990) and works well with incoherent white light (Rousset, 1999). This technique is a differential Hartman technique in which the spot displacement can be inverted. It is easy to see that if the ray impacts are recorded on the other side of the focal plane, the displacement occurs in the opposite direction. Hence, by comparing spot displacement on each side of the focal plane, one can double the test sensitivity. The difference between the two spot displacements is a measure of wave-front

slope independent of the mask irregularities. Both the local wave-front slope and local wave-front curvature can be mapped with the same optical setup, doubling the number of reconstructed points on the wave front. The first astronomical images obtained from a low-order adaptive optical imaging system using a curvature sensor was reported by Roddier (1994). The CFHT adaptive optics bonnette (AOB), PUEO (Arsenault et al., 1994), is based on the variable curvature mirror (Roddier et al., 1991) and has a 19-zone bimorph mirror (Rigaut et al., 1998).

The real-time computation of the wave-front error, as well as correction of wave-front distortion involves digital manipulation of wave-front sensor data in the wave-front sensor processor, the re-constructor and the low-pass filter, and converting to analog drive signals for the deformable-mirror actuators. The functions are to (i) compute sub-aperture gradients, (ii) compute phases at the corners of each sub-aperture, (iii) compute low-pass filter phases, and (iv) provide actuator offsets to compensate the fixed optical system errors and real-time actuator commands for wave-front corrections.

The phase reconstruction method finds the relationship between the measured values and unknown wave-fronts and can be categorized as being either zonal or modal, depending on whether the estimate is either a phase value in a local zone or a coefficient of an aperture function. In the case of curvature sensing, the recorded two out-of-focus images are subtracted and the sensor signal is computed. Subsequently, the Poisson equation is solved numerically and the first estimate of the aberrations is obtained by least squares fitting Zernicke polynomials to the reconstructed wave-front. A conjugate shape is created using this data by controlling a deformable mirror, which typically compose of many actuators in a square or hexagonal array.

Deformable mirrors using discrete actuators are used in astronomical AO systems at various observatories (Shelton and Baliunas, 1993, Wizinovitch et al., 1994). In the operational deformable mirrors, the actuators use the ferroelectric effect, in the piezoelectric or electrostrictive form (Séchaud, 1999 and references therein). The primary parameters of deformable mirror based AO system are the number of actuators (usually more than 50), the control bandwidth and the maximum actuator stroke. The mirrors can be either segmented mirror or continuous faceplate mirrors. Actuators are normally push-pull type; though for curvature sensing actuators are used, these are difficult to fabricate and cost effective. Since the number of actuators are large, there is a need for controlling all the actuators almost simultaneously; the frequency of control is about 1 KHz.

The present generation piezoelectric actuators are no longer discrete, but ferroelectric wafers are bounded together and treated to isolate the different actuators (Lillard and Schell, 1994). Flexible, mirrors micro-machined in silicon is being manufactured for use in AO system. An integrated electrostatically controlled adaptive mirror has the advantage of integrated circuit compatibility with high optical quality; then exhibit no hysteresis and hence are easy to control (Mali et al., 1997).

A new concept of using adaptive secondary mirror to eliminate the optical components required to conjugate a deformable mirror at a reimaged pupil, as well as to minimize

thermal emission has been proposed recently (Bruns et al., 1996). Among the new technologies developed for display components, liquid crystal devices seem to be promising (Love et al., 1994) as an alternative to deformable mirrors.

The performance of the wave-front sensing depends on the characteristics of the detector, viz., (i) the spectral bandwidth, (ii) the quantum efficiency, (iii) the detector noise that includes dark current, read-out and amplifier noise, (iv) the time lag due to the read-out of the detector, (v) the array size and the spatial resolution (Rousset, 1999). Among the various types of detectors available till date, the cameras based on (i) photo-multiplier tubes (Hardy et al., 1977), (ii) MAMA (section 5.2.4), (iii) ICCD (section 5.1), as well as new generation electron bombarded CCD (Cuby et al., 1990), (iv) avalanche photo-diodes (Zappa et al., 1996), (v) Back-illuminated bare CCD (Twichell et al., 1990, Beletic, 1996), (vi) infra-red photo-diode arrays (Rigaut et al., 1992) may be implemented in the wave-front sensing (Rousset, 1999). For reducing the data obtained with AO systems may be processed with the methods developed for high resolution imaging, speckle interferometry and other image processing algorithms (Léna and Lai, 1999a).

9. Diluted aperture interferometry

The marked advantage of using independent telescopes is the increase in resolving capabilities, the greater the distance between the two sub-apertures, the higher the angular resolution. Modern technology has by and large solved the problems encountered by Michelson and Pease (see sub-section 2.2.). Several ground-based long baseline two- or multi-aperture interferometers are in operation, producing excessive scientific results both at optical, as well as at IR wavelengths. Building of different kinds of interferometers are in progress at several places. The following sub-sections dwell upon the salient features of the intensity interferometry, as well as descriptions of the direct interferometers in use at various places.

9.1. Intensity interferometry

An amplitude interferometer, say Michelson's stellar interferometer, measures the covariance $< \Psi_1 \Psi_2 >$ of the complex amplitudes Ψ_1, Ψ_2, at two different points of the wave-fronts, while the intensity interferometer computes the fluctuations of the intensities $\mathcal{I}_1, \mathcal{I}_2$ at these points. The fluctuations of the electrical signals from the two detectors are compared by a multiplier. The current output of each photo-electric detector is proportional to the instantaneous intensity $\mathcal{I}$ of the incident light, which is the squared modulus of the amplitude Ψ. The fluctuation of the current output is proportional to $\Delta \mathcal{I} = | \Psi |^2 - <| \Psi |^2>$. The covariance of the fluctuations, according to Goodman (1985), can be expressed as,

$$< \Delta \mathcal{I}_1 \Delta \mathcal{I}_2 > = <| \Psi_1 \Psi_2^* |^2> .$$

(118)

This expression depicts that the covariance of the intensity fluctuations is the squared modulus of the covariance of the complex amplitude.

Soon after the successful completion of the intensity interferometer in radio wavelengths (Brown et al., 1952), in which the signals at the antennae are detected separately and the angular diameter of the source is obtained by measuring the correlation of the intensity fluctuations of the signals as a function of antenna separation, Brown and Twiss (1956) demonstrated its potential at optical wavelengths by measuring the angular diameter of α CMa (Brown and Twiss, 1958). The advantages of such a system over Michelson's interferometer are that of not requiring high mechanical stability and of being unaffected by seeing. In this arrangement, light from a star collected by two concave mirrors is focused on to two photo-electric cells and the correlation of fluctuations in the photo-currents is measured as a function of mirror separation.

The same technique was applied later by Brown et al., (1967) in the construction of the intensity interferometer at Narrabri, Australia, which has a pair of 6.5 m light collectors on a circular railway track spanning 188 m. The interferometer produced accurate measurement of the diameters of 32 southern bright stars with an angular resolution limit of 0.5 mas (Brown, 1974). The correlator and the control system are housed in a room at the centre.

The degree of correlation depends on the detector spacing in comparison with the size of speckle. In other words, the correlated fluctuations are obtained if the two detectors are spaced by less than a speckle width. Therefore, it is necessary to increase the speckle life time by reducing the spectral band width (Labeyrie, 1985). In this experiment, narrow bandwidth filters were used. The sensitivity of this method is limited by the narrow spectral band used. Theoretical calculations (Roddier, 1988b) show that the limiting visual magnitude of a star that can be observed with the intensity interferometry having a 6.5 m aperture is of the order of 2.

9.2. Amplitude and phase interferometry

In contrast with the intensity interferometer, amplitude or phase interferometry provides a better sensitivity at short wavelengths. The light collected by an array of separated telescopes could be coherently combined. Each pair of telescopes in the array yields a measure of the amplitude of the spatial coherence function of the object at a spatial frequency $\mathbf{B}/\lambda$, where $\mathbf{B}$ is the baseline vector and λ the wavelength. According to the van Cittert-Zernicke theorem (Born and Wolf, 1984), if the number of samples of the coherent function can be made large, the spatial frequency spectrum of the object can be reconstructed. Figure 15 depicts the concept of the amplitude interferometer using two independent telescopes.
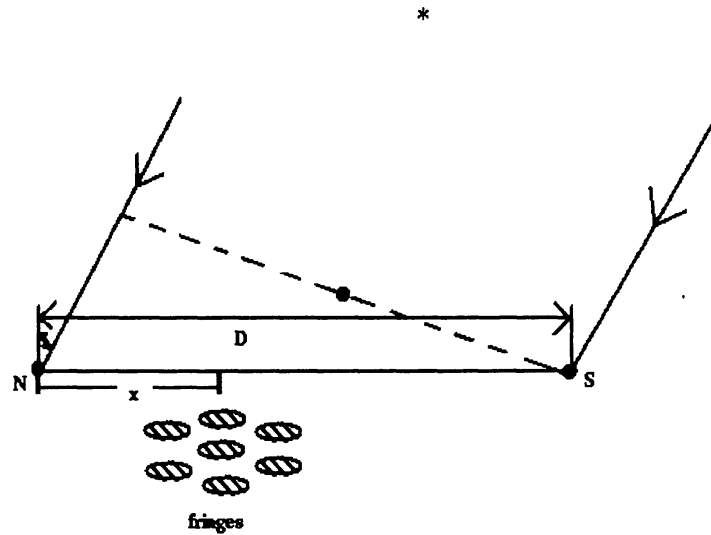
*

Figure 15. Concept of two telescopes interferometer

9.2.1. Interferometers at Plateau de Calern

Labeyrie, (1975) had succeeded in obtaining interference fringes produced by a pair of independent telescopes at Observatoire de Nice, France, in 1974. Subsequently, the interferometer — Interféromètre à Deux Télescope (I2T) — was shifted to a relatively better site, Plateau de Calern, Observatoire de la Cote d'Azur (formerly CERGA). It combines the features of the Michelson design and the radio interferometers and consists of a pair of 26 cm telescopes on altitude-altitude mounts (Labeyrie, 1975) having a long coudé focus. These telescopes track the same source (star) and send the collected light to the central laboratory where the star images are superposed at the foci in order to produce Young's fringes similar to those observed by Michelson and Pease (1921). Both the telescopes are run on tracks for variable North-South baseline (5 - 67 m). Each telescope is a Cassegrain afocal system providing an angular magnification of 23 and the coudé beam is obtained by means of a single reflection on a rotating flat mirror.

The beam-recombining optical device lies on a computer controlled motor driven carriage parallel to the baseline in order to correct the zero optical path length drift induced by the diurnal rotation of the tracked star. The recombining optics are: (i) a plane parallel plate for compensation of the chromatic phase effect induced by the un-equal air travel, (ii) a collimator, (iii) removable optics for control of the pupils' separation, (iv) an anamorphosor to lengthen and narrowing the slit image so as to make full use of the camera target area, and (v) a dispersion grating allowing to observe fringes simultaneously in

several adjoining spectral channels. A pair of photon counting cameras serve for guiding and fringe monitoring (Blazit et al., 1977b). Apart from observing in visible band, this interferometer has also been used for the near IR observation (DiBenedetto and Conti 1983).

Following the success of the operation of I2T, Labeyrie (1978) undertook a project of building a large interferometer — Grand Interféromètre à Deux Télescope (GI2T) — at the same site. The basic principle of this interferometer is similar to that of I2T; it comprises a pair of 1.52 m spherical telescopes (independent Cassegrain-Coudé telescopes) movable on North-South tracks (variable between 12 and 65 m), and an optical recombining system feeding with 2 afocal beams housed in a central laboratory (Labeyrie et al., 1986). Figure 16 shows the GI2T at Plateu de Calern.

Figure 16. Grand interféromètre à deux télescope (GI2T) at Plateu de Calern, France (Courtesy: P. Stee).

As described in the preceding paragraph, here too, the recombiner can be translated between these telescopes in order to compensate for the optical delay. The domeless, 3.5 m diameter spherical telescope made of concrete with a surface accuracy of 1 mm, has three mirrors directing the horizontal afocal Coudé beam to the recombiner optics. The driving system of this sphere consists of a pair of rings; each ring is motorized by 3 actuators acting in 3 orthogonal directions within 2 different tangential planes (Mourard et al., 1994a). The two rings alternately carry the sphere, which in turn, produce continuous motion. Each telescope is equipped with 2 sets of 3 small DC-motors and 3 linear

encoders. The resolution obtained here is of the order of 1 μm - equivalent to 0.1″ on the sky. The clutching of the rings is performed by computer-controlled electro-valves and hydraulic pistons, which carry each of the 60 mm balls that raise the rings by 2 mm to carry the sphere. The main drawback comes from the slow pointing of the telescopes; 4 or 5 stars can be tracked during the night (Mourard et al., 1994a).
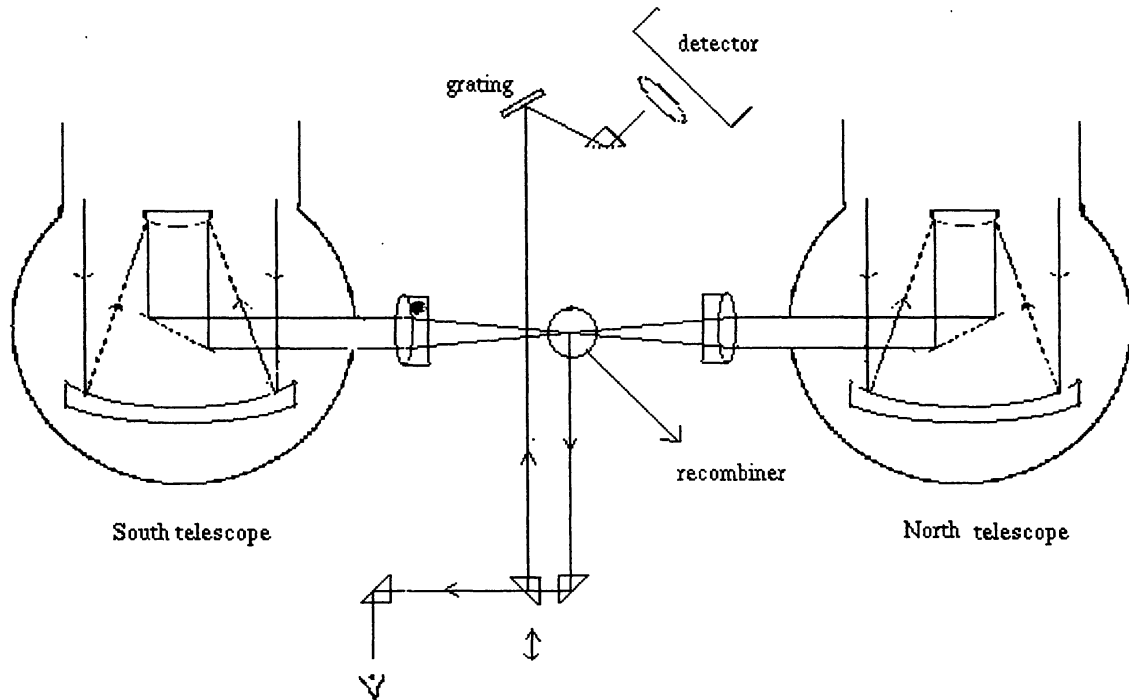

Figure 17. Concept of acquiring fringes of an object using GI2T.

Figure 17 depicts the concept of acquiring fringes of an object using GI2T. The beams from these telescopes are recombined in an image plane after reconfiguring the pupils; the fringed speckles are dispersed and the spectra are recorded at short-exposure using a photon counting detector (Labeyrie et al 1986). [Fringed speckle can be visualized when a speckle from one telescope is merged with the speckle from other telescope]. The optical table carrying the focal point instruments moves along the North-South direction to maintain constant zero optical path different (OPD) within the coherence length between the two beams (OPD changes due to the diurnal motion). The instruments consist of (i) a recombining element for reconfiguring the pupil and fixing the fringe spacing, (ii) an imager slicer (a series of 10 wedges of different angles stuck on a field lens slices the image), (iii) the compensating system of the atmospheric dispersion, (iv) gratings (maximum spectral resolution 0.15 nm), (v) detectors to record the fringes, etc. A new addition is an implementation of a fringe tracker based on photon counting detector and real-time image processing unit on the said interferometer (Koechlin et al., 1996).

The slicing of the image at the entrance of the spectrograph is required to obtain better visibility since the large aperture (1.5 m telescope) produces more than 100 speckles in the

image and the fringe pattern within each speckle is randomly phased (Bosc, 1988). The advantages of the dispersion mode are the capabilities to (i) allow continuous observation of fringes across the spectral bandwidth, (ii) record the fringes with longer integration time, and (iii) select different spectral channels for differential visibility measurements (continuum and spectral line). The continuum channel is supposed to originate from the unresolved region of a star, say photosphere and the other one centred on a part of the spectra created in an extended region, say circumstellar medium. The modulus of the fringe visibility is estimated as the ratio of high frequency to low frequency energy in the average spectral density of the short exposure. The calibration of the resulting visibility is performed with a reference star, for example, $\mathcal{V}^2_{cal} = \mathcal{V}^2/\mathcal{V}^2_{ref}$ (Mourard et al., 1994b, Thureau et al., 1998). Two different types of detectors, (i) CP40 (Blazit, 1986), and (ii) RENICON (Clampin et al., 1988) are being used for data acquisition.

9.2.2. Mount Wilson stellar interferometer

Since 1978, an interferometer with two independent small apertures was in operation (Shao and Staelin, 1980) at Mt. Wilson, USA. Improvements of this interferometer have taken place in two stages, viz., mark II (Shao et al., 1986a, 1986b, Shao and Colavita, 1987), and mark III (Shao et al., 1988). The fringes of the objects are obtained with automated operation. The basic programme of this interferometer, among others, is wide-angle astrometry (Shao et al., 1990).

Unlike the interferometers described above (see section 9.2.1), this interferometer uses (i) siderostats and star trackers to point the instrument at a star, (ii) an optical delay line to control the internal optical path lengths, and (iii) a laser metrology system to monitor the position of the siderostat mirrors. The 25 mm optical flat (siderostat mirror), is attached to a polished hemisphere. A set of 4 laser interferometers measure the position of the sphere relative to a set of 4 corner cubes embedded in a reference plate (Shao, 1988). The delay line has a peak to peak range of 20 m with a small signal bandwidth. For the astrometric observations, the measurement of the central fringe is performed in two colours to correct for the error caused by atmospheric turbulence, while for stellar diameter programmes, it is done through narrow band filters.

9.2.3. Sydney University stellar interferometer (SUSI)

After the successful venture of Narrabri intensity interferometer (Brown, 1974), the Sydney University had built a prototype diluted aperture amplitude interferometer with a 11 m baseline using two coelostats as light collector (Davis and Tango, 1985a, 1985b) and determined the angular diameter of α CMa (Davis and Tango, 1986). Subsequently, they have built an optical interferometer with a baseline ranging from 5 m to 640 m on North-South direction (Davis, 1994). The required baselines are achieved with an array of 11 input stations, each equipped with a siderostat and relay optics, located to give a minimal baseline redundancy (Davis et al., 1998, 1999a); the intermediate baseline forms a geometric progression increasing in steps of $\sim 40\%$. The size of each aperture is 14 cm

(single r_0). The wave-front tilt correction and dynamic path length equalization are the two main features of this system.

Starlight is steered by two siderostats of 20 cm diameter using an Altitude/Azimuth mount placed upon large concrete piers, via relay mirrors into the evacuated pipe system that carries the light to the central laboratory (Davis et al., 1992). At the central laboratory, the light enters a beam reducing telescope followed by the atmospheric refraction correctors systems consisting of the pairs of counter-rotating Risley prisms. Then the beam either enters the optical path length compensator (OPLC) or is diverted towards the acquisition camera. On leaving OPLC, the beams from the two arms of this interferometer is switched to one of the optical tables (blue or red) for recombination.

9.2.4. Cambridge optical aperture synthesis telescope (COAST)

As discussed earlier in section 6.4, the corrupted phase of the spatial coherence function due to the instrumental and atmospheric phase errors can be corrected by using data processing algorithms. But the direct measurements of closure phase (see section 4.6) of any object using three or more independent telescopes in visible band have been made feasible at Cambridge by Baldwin et al., (1998).

Four telescopes, each comprises a 50 cm siderostat flat feeding a fixed horizontal 40 cm Cassegrain telescope (f/5.5) with a magnification of 16 times, are arranged in a Y-layout with one telescope on each arm, movable to a number of fixed stations and one telescope at the centre of the Y. Light from each siderostat passes through pipes containing air at ambient pressure into the beam combining laboratory. The laboratory accommodates the optical path compensation delay lines, the beam combining optics, the detectors, the fringe acquisition systems etc. (Baldwin, 1992, Baldwin et al., 1994). The laboratory is a tunnel (32 m length $\times$ 6 m width $\times$ 2.4 m height), covered sufficiently with earth having thick insulating end walls that provides a stable thermal environment internally for the path compensator delay lines, combining optics and detectors.

Each of the four telescope beams is provided with a variable delay line (maximum delay is 37 m); the equalization of the path delays for each of them is carried out by a movable trolley, carrying a roof mirror running on a rail track (Baldwin et al., 1994). The four beams emerging from the path compensator are each split at a dichroic; the longer wavelength ($\lambda >650$ nm) of the visible band passes into the beam combining optics and the shorter ones are used for acquisition and autoguiding. A cooled CCD detector system is used for both acquisition and guiding. The 4-way beam combiner accepts four input beams, one from each telescope provides four output beams, each having equal contributions from the light from the four telescopes. Each output beam passes through an iris diaphragm and is focused by a long focus lens on to a fibre fed single-element avalanche photo-diode detector (Nightingale, 1991) for fringe detection (Baldwin et al., 1994). A similar beam combiner is added recently for the near IR capability (Young et al., 1998).

9.2.5. Infrared-optical telescope array (IOTA)

The IR-optical telescope array at Mt. Hopkins, Arizona, USA, consists of two 45 cm collector assembly; each assembly comprises a siderostat, an afocal Cassegrain telescope and an active relay mirror. The collectors can be located at various stations on the L-shaped baseline, to achieve baselines between 5 to 38 m. The tip-tilt corrected afocal star light beams (4.5 cm diameter) from the telescopes are brought to the beam combining table. Optical differences are compensated by fixed and variable delays and the beams are recombined onto a beam splitter, producing two complementary interference signals (Carleton et al., 1994). These are focused onto a pair of InSb photovoltaic detectors through a K-band filter. Fast autoguiding system is used to correct the atmospheric wave-front tilt errors and a precise optical delay line is employed to compensate the effect of earth's rotation. Two active delay lines for three telescopes are provided. A scanning piezo mirror is used to modulate the optical path difference between the two telescopes. A thinned back-illuminated SITs 512×512 CCD with a quantum efficiency 90%, is used as sensor for IOTA's visible light detector.

In addition to the afore-mentioned interferometers, several long baseline interferometers and imaging interferometric array at optical/IR bands, viz., (i) European Southern Observatory's (ESO) very large telescope interferometer (VLTI) at Cerro Paranal, Chile (Mariotti et al., 1998), (ii) Palomar testbed interferometer (Malbet et al., 1998), (iii) Keck interferometer with a pair of 10 m telescopes on a 85 m baseline at Mauna Kea, Hawaii (Colavita et al., 1998, van Belle et al., 1998), (iv) US Navy prototype optical interferometer (Armstrong, 1994, Hutter, 1994), (v) CHARA array (McAlister et al., 1998) etc. are at various stages of development. The VLTI comprises of four 8.2 m telescopes and three movable 1.8 m auxiliary telescopes, situated at Cerro Paranal peak, Chile. Beams are supposed to be received from these movable telescopes in the central laboratory for recombination and are to be made to interfere after introducing suitable optical delay lines (Léna and Lai, 1999a); it is planned to use AO systems at the telescopes for efficient interferences.

10. Astrophysical results

The single aperture interferometry has made impacts in several important fields in astrophysics, viz., (a) in studying the separation and orientation of close binary stars, (b) in measuring diameter of giant stars, (c) in resolving the heavenly dance of Pluto-Charon system (Bonneau and Foy, 1980, Baier and Weigelt, 1987, Beletic et al., 1989), (d) in determining shapes of asteroids (Drummond et al., 1988), (e) in mapping the finer features of extended objects (section 7), (f) in estimating sizes and mapping certain types of circumstellar envelopes, (g) in revealing structures of active galactic nuclei, and of compact clusters of a few stars like R136a complex, (h) in resolving the gravitationally lensed QSO's, etc.

The results obtained with diluted aperture interferometry in the visible wavelength are from the area of stellar angular diameters with implications for emergent fluxes, effective

temperatures, luminosities and structure of the stellar atmosphere, dust and gas envelopes, binary star orbits with impact on cluster distances and stellar masses, relative sizes of emission-line stars and emission region, stellar rotation, limb darkening, astrometry. Some of the results mentioned above can be found in various articles (Labeyrie, 1985, McAlister, 1988, Ridgway, 1988, 1992, Roddier, 1988b, Foy, 1992, and references therein). In what follows, the important astrophysical results barring extended objects (noted already in section 7), obtained in the visible band in the recent past are addressed.

10.1. Results obtained with single aperture interferometry

I. Studies of close binary stars are of paramount importance in stellar astrophysics, and play a fundamental role in measuring stellar masses, providing a benchmark for stellar evolution calculations; a long term benefit of interferometric imaging is a better calibration of the main-sequence mass-luminosity relationship (McAlister, 1988). An important parameter in obtaining masses of stars involves combining the spectroscopic orbit with the astrometric orbit as projected on the sky from the interferometric data (Torres et al., 1997). The atmosphere of the component of a close binary system is distorted mainly by physical effects, viz., (i) rotation of the component, (ii) the tidal effect due to the presence of its component. The modelling of the radiative transfer concerning the effects of irradiation on the line formation in the expanding atmospheres of the components of close binary systems (Peraiah and Rao, 1998) can be studied.

Speckle interferometric observations of close binary stars have been carried out using telescopes of various sizes by several groups. Major contributions in resolving close binary systems came from the Center for High Angular Resolution Astronomy (CHARA) at Georgia State University, USA. In a span of a little more than 20 yr, this group had observed more than 8000 objects; 75% of all published interferometric observations are of binary stars (Hartkopf et al., 1996, 1997a, 1997b, McAlister et al., 1996, Mason et al., 1998). The separation of most of the new components discovered by interferometric observations are found to be less than 0.25″ (McAlister et al., 1993). During the period of 1989 - 1994, Hartkopf et al., (1996) reported observations of 694 binary star systems using said technique with the 4 m Cerro Tololo telescope. From an inspection of the interferometric data obtained with the cameras at CHARA and US naval observatories (USNO), Mason et al., (1999) have confirmed the binary nature of 848 objects, discovered by the Hipparcos satellites.

In order to derive accurate orbital elements and masses, luminosities and distances, emphasis laid down in their programmes was the continuous observation of spectroscopic binaries. A survey of chromospheric emission (H and K lines of Ca II) in more than 800 southern stars (solar type) reveals that about 70% of them are inactive (Henry et al., 1996). In a programme of bright Galactic O stars for duplicity, Mason et al., (1998) could resolve 15 new components. They opined that at least one-third of the O stars, especially those among the members of clusters and associations, have close companions; a number of them, may even have a third companion. Among a speckle survey of several Be stars, Mason et al., (1997) were able to resolve 5 binaries including a new discovery.

S. K. Saha

From a survey for duplicity among white dwarf stars, McAlister et al., (1996) reported faint red companions to GD 319 and HZ 43.

Survey of visual and interferometric binary stars with orbital motions have also been reported by other groups (Balega et al., 1984, 1994, Balega and Balega, 1985, Bonneau et al., 1986, Blazit et al., 1987, Horch et al., 1996, 1999, Douglass et al., 1997). Leinert et al., (1997) have resolved 11 binaries by means of near IR speckle interferometry, out of 31 Herbig Ae/Be stars, of which 5 constitute sub-arc-second binaries. In a recent article, Germain et al., (1999) have reported position angles and separations of 547 binaries using 66 cm refractor at USNO in Washington.

Reconstructing the phase of binary stars using various image processing algorithms have been made (Karovska et al., 1986a, Miura et al., 1992, Horch et al., 1997, 1999, Saha and Venkatakrishnan, 1997, Saha et al., 1999b, 1999c). Speckle interferometric observations in the IR band have detected the close companions of Θ^1 Ori A and Θ^1 Ori B (Petr et al., (1998). Subsequently, Simon et al., (1999) have found an additional faint companion of the latter. Recently, Weigelt et al., (1999) have detected a close companion of Θ^1 Ori C with a separation of $\sim$ 33 mas. These Trapezium system, Θ^1 Ori ABCD, are massive O-type and early B-type stars and are located at the centre of the Orion nebula. The speckle masking reconstruction of a close binary star, 41 Dra was carried out (Balega et al., 1997a, 1997b); the separation of the binary components was found to be about 25 mas, the resolution at the wavelength of 656 nm was 23 mas (λ/D). Figure 18 demonstrates the reconstructed image of said binary star 41 Dra.
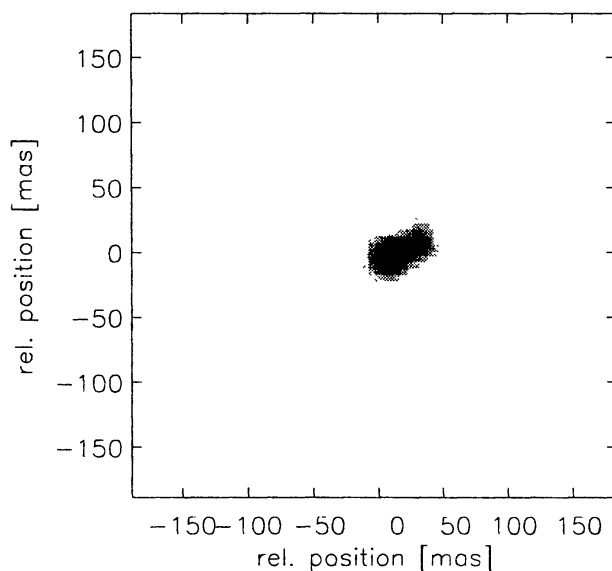
Figure 18. The speckle masking reconstruction 41 Dra (Balega et al., 1997a, 1997b). The separation of the binary was about 25 mas (Courtesy: R. Osterbart).

Various investigators have also calculated the orbital characteristics of many close binary stars (Duquennoy et al., 1996, Gies et al., 1997, Torres et al., 1997, Mason et al., 1998, 1999, Aristidi et al., 1999). Torres et al., (1997) derived individual masses for θ^1 Tau using the distance information from θ^2 Tau. They found the empirical mass-luminosity relation from the data in good agreement with the theoretical models. Orbital motions of DF Tauri from the speckle imaging have also been reported (Thiébaut et al., 1995). Gies et al., (1997) measured the radial velocity for the massive binary 15 Monocerotis. Discovery of two binary stars, viz., (a) MOAI 1 (Carbillet et al., 1996), (b) ν Cyg (Hipparcos catalogue, 1997) have been reported recently. Nisenson et al., (1985) have resolved a faint optical source close to T Tauri with a separation of 0.27″. The visual magnitude difference was found to be 4.33.

Kuwamura et al., (1992) obtained a series of spectra using objective speckle spectrograph with the bandwidth spanning from 400 nm - 800 nm and applied shift-and-add algorithm for retrieving the diffraction-limited object prism spectra of ζ Tauri and ADS16836. They have resolved spatially two objective prism spectra corresponding to the primary and the secondary stars of ADS16836 with an angular separation of $\approx 0.5''$ using speckle spectroscopy. Reconstructing emission and absorption lines of several single stars have been carried out by Kuwamura et al., (1993a, 1993b). Using imaging spectroscopic (Baba et al., 1994a) method, Baba et al., (1994b) have observed a binary star, ϕ And (separation 0.53″) at the Cassegrain focus of the 1.88 m telescope of the Okayama Astrophysical Observatory; the reconstructed spectra using algorithm based on cross-correlation method revealed that the primary star (Be star) has an Hα emission line while the secondary star has an Hα absorption line. Grieger and Weigelt, (1992) used a wide-band speckle spectrograph to record interferograms of a binary star (Grieger and Weigelt, 1992) with the ESO 2.2 m telescope, La Silla, Chile. These authors have reconstructed the diffraction-limited image and spectrum of a binary star with speckle masking technique (section 6.4).

The high angular polarization measurements of the pre-main sequence binary system Z CMa at 2.2 μm have been reported recently by Fischer et al., (1998). They have found that both the components are polarized; the secondary showed an unexpected large polarization degree. Measurements of the close binary systems have also been carried out by means of aperture masking technique (Nakajima et al., 1989, Busher et al., 1990, Bedding et al., 1992). Recently, Robertson et al., (1999) reported from the measurements with aperture masking technique at 3.9 m AAO telescope that β Cen, a β Cephei star is a binary systems with components separated by 0.015″.

Another interesting programme, occultation binary star survey, is being carried out by CHARA group (Mason, 1995). When any planetary body of notable size passes in front of a star, the light coming from the latter is occulted. The method is sensitive enough to detect the presence of an atmosphere on Ganymede − a Jovian satellite, from its occultation of SAO 186800 (Carlson et al., 1973), and will remain useful because of the extraordinary geometric precision it provides. More recently, Tej et al., (1999) have reported the measurements of the angular diameter of the Mira variables R Leonis in near IR bands at the 1.2 m telescope, Mt. Abu, India.

The notable advantage of occultation of binary stars is that of determining relative intensities and measure the separations comparable to those measured by long baseline interferometers. The contribution of speckle survey of occultation binaries till date, at the smallest separation region, is of the order of $< 0.025''$. Further, this method provides a means of determining the limiting magnitude difference of speckle interferometry. The shortcomings of this technique can be noted as its singular nature; the object may not occult again until one Saros cycle later (18.6 yr), and limited to a belt of the sky (10% of the celestial sphere). The direct speckle interferometric measurement of more than 2 dozens new occultation binaries have been reported (Mason, 1995, 1996).

II. Several multiple stars (Tokovinin, 1997) were observed by means of speckle interferometric method (Cole et al., 1992, Hartkopf et al., 1992, Goecking et al., 1994, Aristidi et al., 1997, 1999). The star-like object, Luminous Blue Variable (LBV), η Carina, was found to be a multiple object (Weigelt and Ebersberger, 1986, Hofmann and Weigelt, 1988). Image reconstruction with speckle masking method of the same object showed 4 components with separations $0.11''$, $0.18''$ and $0.21''$ (Weigelt, 1988, Hofmann and Weigelt, 1993). Falcke et al., (1996) recorded speckle polarimetric images of the same object with the ESO 2.2 m telescope. The polarimetric reconstructed images with $0.11''$ resolution in the Hα line exhibit a compact structure elongated in consistent with the presence of a circumstellar equatorial disk. Károvska et al., (1986b) detected two close optical companions to the supergiant α Orionis using photon counting PAPA detector. The reconstructed image depicted that the separations of the closest and the furthest companions from the said star are $0.06''$ and $0.51''$ respectively. The respective magnitude differences with respect to the primary at Hα were found to be 3.4 and 4.6.

Ground-based conventional observations of another important luminous central object, R136 (HD38268), of the 30 Doradus nebula in the LMC depict three components R136; a, b, and c, of which R136a was thought to be the most massive star with a solar mass of $\sim 2500 M_\odot$ (Cassinelli et al., 1981). Later, it was found to be a dense cluster of stars with speckle interferometric observations (Weigelt and Baier, 1985, Neri and Grewing, 1988). The reconstructed image with speckle masking technique depicts more than 40 components in the $4.9'' \times 4.9''$ field; the closest binaries were found to be $0.03''$ and $0.05''$ (Pehlemann et al., 1992). Observations of R64, HD32228, the dense stellar core of the OB association LH9 in the LMC, revealed 25 stellar component within a $6.4'' \times 6.4''$ field of view (Scherti et al., 1996). Specklegrams of this object were recorded through the Johnson V spectral band, as well as in the strong Wolf-Rayet emission lines between 450 and 490 nm. Several sets of speckle data through different filters, viz., (a) RG 695 nm, (b) 658 nm, (c) 545 nm, and (d) 471 nm of the central object HD97950 in the giant HII region starburst cluster NGC3603 at the 2.2 m ESO telescope, were also recorded (Hofmann et al., 1995). The speckle masking reconstructed images depict 28 stars within the field of view of $6.3'' \times 6.3''$, down to the diffraction-limited resolution of $\sim 0.07''$ with m_v in the range from 11.40 - 15.6.

III. Speckle interferometric observations carried out at large telescopes depict that the diameters of red supergiants α Orionis and Mira are wavelength dependent (Bonneau

and Labeyrie, 1973, Labeyrie et al., 1977, Balega et al., 1982, Bonneau et al., 1982, Karovska et al., 1991, Weigelt et al., 1996). A recent study by means of bispectrum image reconstructions of the former star, based on the data obtained at the Nasmyth focus of William Herschel Telescope, Klückers et al., (1997) established the evidence of asymmetry on its surface. Prior to this, Karovska and Nisenson (1992) also found in the reconstructed image of the same object, the evidence for the presence of a large bright feature on the surface. The reconstructed images of Mira variable R Cas (Weigelt et al., 1996) showed that the disk of the star a non-uniform and elongated along the position angle 52° ± 7° and 57° ± 7° in the 700 nm (moderate TiO band absorption), as well as in the 714 nm (strong TiO band absorption) respectively.

Many supergiants have extended gaseous atmosphere which can be imaged in their chromospheric lines. By acquiring specklegrams in the continuum and in the chromospheric emission lines simultaneously, differential image can be constructed. Hebden et al., (1987) used differential speckle interferometric technique to study the chromospheric envelope of α Orionis in the Hα wavelength. The rotation shear interferometer (Roddier and Roddier, 1988) had also been applied in the visible band to map the visibility of fringes produced by the star, and the reconstruction of the image revealed the presence of light scattered by a highly asymmetric dust envelope.

Apart from measuring the angular diameters of cool stars (Busher et al., 1990, Bedding et al., 1992, 1997a, Haniff et al., 1995), surface imaging of long period variables stars (Tuthill et al., 1999a), aperture synthesis using non-redundant masking technique at various large telescopes too depicted the presence of hotspots and other asymmetries on the surface of red supergiants and Mira variables (Busher et al., 1990, Haniff et al., 1992, Wilson et al., 1992, Bedding et al., 1997a, Tuthill et al., 1997).

Observations carried out at 4.2 m William Herschel telescope, La Palma, Wilson et al., (1997) have detected a complex bright structure in the surface intensity distribution of Betelgeuse that changes in the relative flux and positions of the spots over a period of eight weeks; a new circularly symmetric structure around the star with a diameter of $\geq 0.3''$ is found. As far as Mira variables are concerned, Haniff et al., (1995) have reported that the derived linear diameters of the same are not compatible with fundamental mode of pulsation. Bedding et al., (1997a) have found that the diameter of R Doradus (57±5 mas) exceeded that of Betelgeuse; an asymmetric brightness distribution has also been detected from non-zero closure phases measurement. The diameter of a small amplitude Mira, W Hya, are reported to be 44±4 mas (Bedding et al., 1997a).

The reconstructed images in the optical, as well as near IR speckle interferometric observations of another interesting object, the red super giant VY CMa, an unusual star that displays large amplitude variability in the visible and strong dust emission and high polarization respectively in the mid and near IR, Wittkowski et al., (1998a) found to have non-spherical circumstellar envelope. They opined that the star was an immediate progenitor of IRC+10420, a post red supergiant during its transformation into a Wolf-Royet (WR) star. The visibility function in the 2.11 μm band image reconstruction depicted the contribution to the total flux from the dust shell to be $\sim 40\%$, and the rest

from the unresolved central object (Blöcker et al., 1999). From the reconstructed images of the non-redundant masking of 21-hole aperture observations of VY CMa carried out at the 10 m Keck telescope in the IR wave bands, Monnier et al., (1999) have found emission to be one-sided, inhomogeneous and asymmetric in the near IR. They were able to derive the line-of-sight optical depths of circumstellar dust shell; the results allow the bolometric luminosity of VY CMa to be estimated independent of dust shell geometry. Haas et al., (1997) have detected a halo of Elias I with near IR speckle interferometry.

IV. High resolution interferometric imagery may depict the spatial distribution of circumstellar matter surrounding objects which eject mass, particularly young compact planetary nebulae (YPN) or newly formed stars in addition to T Tau stars, late type giants or supergiants. The large, older and evolved planetary nebulae (PN) show a great variety of structure (Balick, 1987) that are (a) spherically symmetric (A39), (b) filamentary (NGC6543), (c) bipolar (NGC6302), and (d) peculiar (A35). The structure may form in the very early phases of the formation of the nebulae itself which is very compact and unresolved. Due to the poor spatial resolution of the conventional imaging (section 3.4), the first $\sim 10^3$ years of a PN are spent in a phase that remains obscured for structural details. In order to understand the processes that determine the structure and dynamics of the nebular matter in the PN, one needs to resolve and map the same when they are young and compact. By making maps at many epochs, as well as by following the motion of specific structural features, it would enable one to understand the dynamical processes at work. The structures could be different in different spectral lines e.g., ionisation stratification in NGC6720 (Hawley and Miller, 1977), and hence maps can be made in various atomic and ionic emission lines too.

The angular diameters of several young PNs in the Magellanic Clouds were determined with speckle interferometric technique (Barlow et al., 1986, Wood et al., 1986, 1987). The high spatial resolution images of Red Rectangle (AFGL 915), a reflection nebula around the star HD44179, were recorded by several groups (Leinert and Haas, 1989, Cruzalébes et al., 1996, Osterbart et al., 1996, 1997). These observations exhibit two lobes with the separation of $\sim 0.15''$. Osterbart et al., (1996) argued that the dark lane between the lobes is due to an obscuring dust disk and the central star is a close binary system. Figure 19 depicts the speckle masking reconstruction of the evolved object Red Rectangle; observations were carried out with NICMOS3 NIR-camera at the 6 m telescope, Special Astrophysical Observatory (SAO), Russia (Osterbart et al., 1996). The resolution of this object is 75 mas for the H band.

Osterbart et al., (1996) reported from the reconstructed speckle images of the carbon star IRC+10216 (CW Leo) obtained at the SAO 6 m telescope, about a resolved central peak surrounded by patchy circumstellar matter. They found that the separation between bright clouds was $0.13'' - 0.21''$, implying a stochastic behaviour of the mass outflow in pulsating carbon stars. Weigelt et al., (1998) found that five individual clouds were resolved within a $0.21''$ radius of the central object in their high resolution K$'$ band observation at the afore-mentioned telescope. They argued that the structures were produced by circumstellar dust formation. Figure 20 depicts the speckle masking reconstruction of
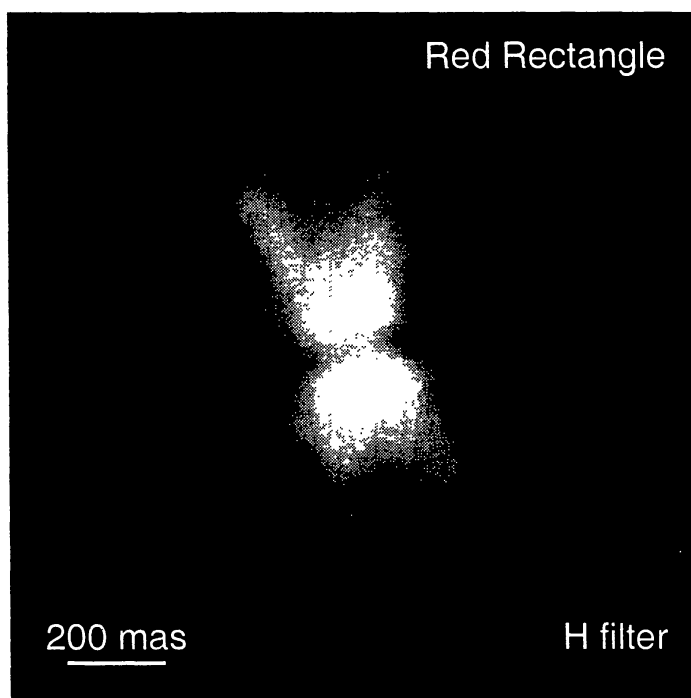
Figure 19. Speckle masking reconstruction of the evolved object Red Rectangle (Courtesy: R. Osterbart); observations were carried out with NICMOS3 NIR-camera at the Russian SAO 6 m telescope (Osterbart et al., 1996).

IRC+10216; The resolution of this object is 76 mas for the K' band. Recently, Tuthill et al., (1999b) recorded high resolution IR (1.65 μm and 2.27 μm) images of WR104 by means of aperture masking technique at the 10 m Keck telescope, Hawaii. The reconstructed images of the same at two epochs depict a spiral pinwheel in the dust around the star with a rotation period of 220 ± 30 days. They opined that the circumstellar dust and its rotation are the consequence of a binary companion. The aspherical dust shell of the oxygen-rich AGB star AFGL 2290 (Gauger et al., 1999) has also been reported.

The detailed information that is needed for the modelling of the 2-d radiative transfer concerning the symmetry − spherical, axial or lack of clouds, plumes etc. − can also be determined (Peraiah, 1999). Recently, 1-d, as well as 2-d radiative transfer modelling of AFGL 2290 (Gauger et al., 1999), Red Rectangle (Men'shchikov and Henning, 1997) have been carried out and used for the interpretation of the observation. The radiative transfer calculations in the case of the latter depicted that the dust properties are spatially inhomogeneous (Men'shchikov et al., 1998). In the radiative transfer calculation, using the code DUSTY developed by Ivezić et al., (1997), Blöcker et al., (1999) noticed the ring like shell's intensity distribution of the rapidly evolved hypergiant object IRC+10420.

V. Both nova and supernova (SN) have complex nature of shells viz., multiple, secondary and asymmetric; high resolution mapping may depict the events near the star and the interaction zones between gas clouds with different velocities. Soon after the explosion

S. K. Saha
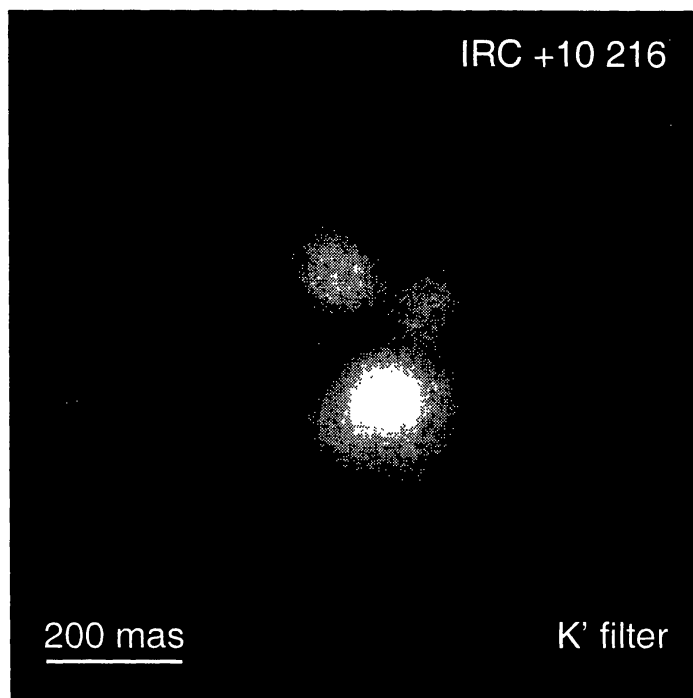
Figure 20. Speckle masking reconstruction of IRC+10216 (Courtesy: R. Osterbart); observations were carried out with NICMOS3 NIR-camera at the Russian SAO 6 m telescope (Osterbart et al., 1996).

of the supernova SN1987A, various groups of observers monitored routinely the expansion of the shell in different wavelengths by means of speckle imaging (Nisenson et al., 1987, Papaliolios et al., 1989, Wood et al., 1989). Karovska et al., (1989, 1991) measured the increasing diameter of the SN in several spectral lines and the continuum and Nulsen et al., (1990) have derived the velocity of the expansion. These observers found that the size of this object was strongly wavelength dependent at the early epoch — pre-nebular phase indicating stratification in its envelope. A bright source at 0.06″ away from the said SN with a magnitude difference of 2.7 at Hα had been detected 30 and 38 days after the explosion by Nisenson et al., (1987) and 50 days after by Meikle et al., (1987). Chalabaev et al., (1989) detected asymmetries in IR speckle observations that were in the same direction as the bright object. Papaliolios et al., (1989) reported the asymmetry of the shell too. Based on the KT algorithm, that preserves the phase of the object Fourier transform, Karovska and Nisenson (1992) reported the presence of knot-like structures. They opined that the knot-like structure might be due to a light echo from material located behind the supernova. Recent studies by Nisenson and Papaliolios (1999) with a image reconstruction algorithm based on iterative transfer algorithm (Fienup, 1984) reveal a second spot, a fainter one (4.2 magnitude difference) on the opposite side of the SN with 160 mas separation. Figure 21 depicts the recent image reconstruction based on modified iterative transfer algorithm of SN1987A (Nisenson and Papaliolios, 1999).

VI. Another important field of observational astronomy is the study of the physical processes, viz., temperature, density and velocity of gas in the active regions of the active
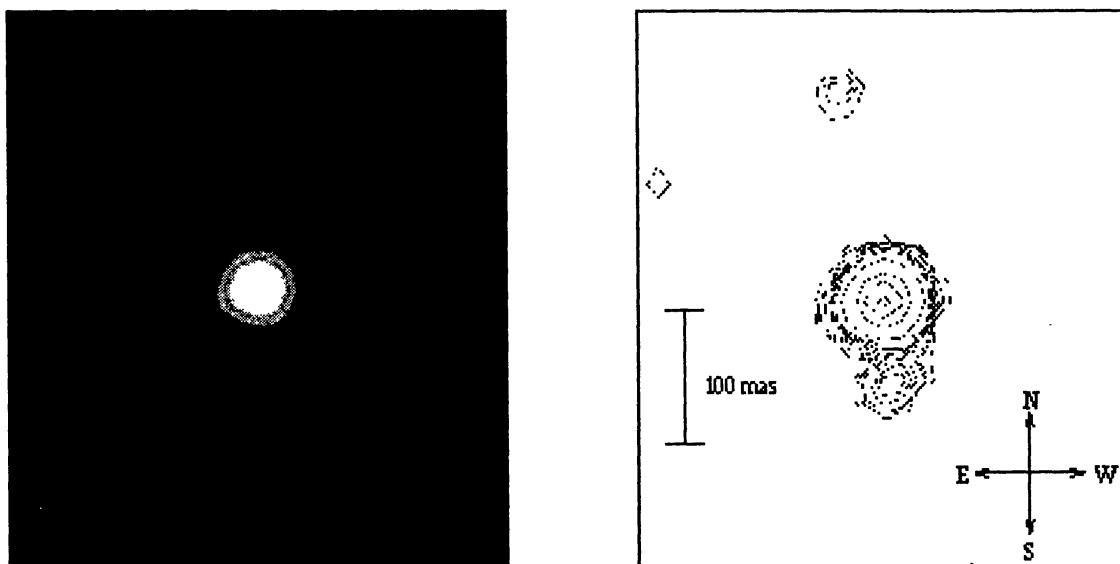
Figure 21. The reconstructed image and contour plot of SN1987A (Nisenson and Papaliolios, 1999, Courtesy: P. Nisenson).

galactic nuclei (AGN); optical imaging in the light of emission lines on sub-arc-second scales can reveal the structure of the narrow-line region. The scale of narrow-line regions is well resolved by the diffraction limit of a moderate-sized telescope (Afanas'jev et al., 1988, Ulrich, 1988). The time variability of AGNs ranging from minutes to decades (Krishan and Witta, 1994) is an important phenomena, which can also be studied with high resolution interferometric technique.

Two of the brightest Seyfert galaxies, (i) NGC1068, and (ii) NGC4151, have strong emission lines. In the case of latter, Shields (1999) points out the relative prominence of narrow forbidden lines in comparison with the former. The high resolution IR observation of NGC1068 depicted a compact core (Chelli et al., 1987, Weinberger et al., 1996, Young et al., 1996). Wittkowski et al., (1998b) have resolved this compact source with the diameter of 0.03″ in the K-band.

Figures 22 and 23 depict respectively the azimuthally averaged visibilities and the diffraction-limited speckle masking reconstruction of NGC1068. From the high resolution mapping of the object in the optical band, O III emission line, Ebstein et al., (1989), found a bipolar structure, extending over 0.4″. Hofmann et al., (1992) resolved the extension into 5 components. With the speckle spectroscopic method, Afanasiev et al., (1992) determined the radial velocity of both NE and SW clouds located at 0.34″ and 0.33″ respectively from the centre. Ebstein et al., (1989) have resolved NGC4151 in O III lines and from the reconstructed image they found the diameter to be 0.4″. Zeidler et al., (1992) have resolved the 2.3″ central region of another AGN, NGC1346, into 4 clouds, distributed along the position angle of 20°.

S. K. Saha
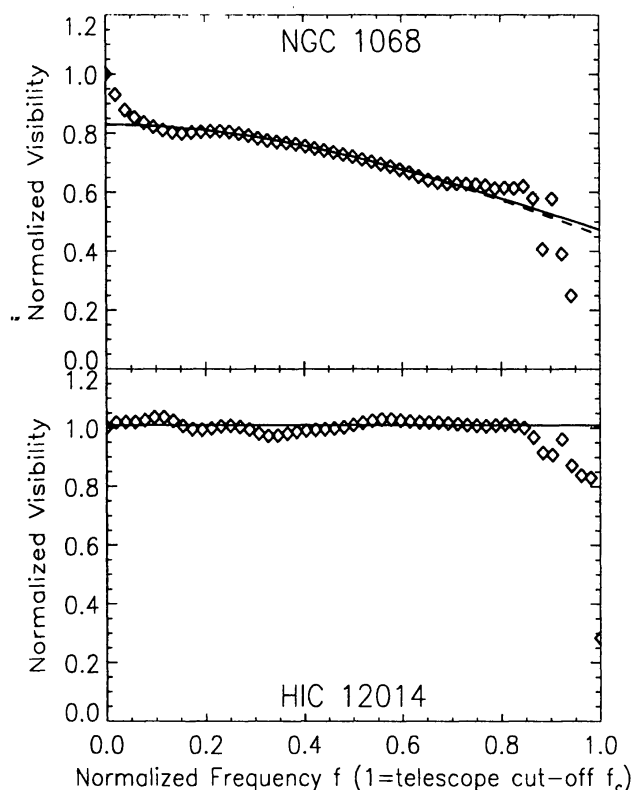
Figure 22. Azimuthally averaged visibilities of NGC1068 (top) and of unresolved reference star HIC12014 (bottom). The diamonds indicate the observed visibilities, the solid lines the Gaussian fits, and the dashed line is UD fit (Courtesy: M. Wittkowski).

VII. Quasars (QSO) may be gravitationally lensed by stellar objects, viz., stars, galaxies, clusters of galaxies etc., located along the line of sight. The aim of the high angular imagery of these QSO's is to find their structure and components; their number and structure as a probe of the distribution of the mass in the Universe (Ulrich, 1988). Capability of resolving these objects in the range of 0.2″ to 0.6″ would allow the discovery of many more lensing events (Foy, 1992). With the speckle interferometric technique, the gravitational image of the multiple QSO PG1115+08 was resolved (Hege et al., 1981, Foy et al., 1985). Foy et al., (1985) have found one of the bright components, discovered to be double by Hege et al., (1981), was elongated. The possible causes of the structure, according to them, was due to a fifth component of the gravitational image of the QSO.

10.2. Results obtained with adaptive optics

The noted advantages of the adaptive optics (AO) system over the conventional techniques are the ability to recover near diffraction-limited images and to improve the point source sensitivity; but these need excellent seeing conditions; an exact knowledge of point spread function is necessary. Amplitude fluctuations are generally small and their effect on image degradation remains limited, and therefore, their correction is not needed, except for detection of exo-solar planets (Stahl and Sandler, 1995, Love and Gourlay, 1996).
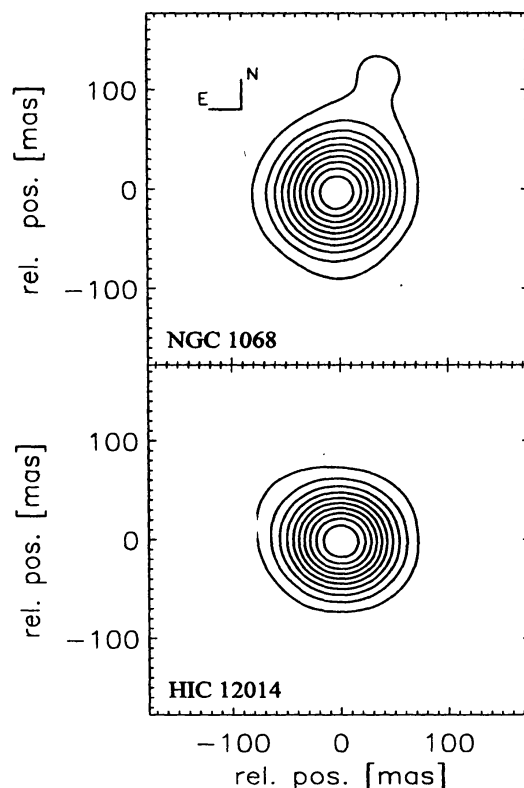
Figure 23. The speckle masking reconstruction of NGC1068 (top) and the unresolved star HIC12014 (bottom). The contours are from 6% to 100% of peak intensity (Courtesy: M. Wittkowski).

AO system lacks capability of restoring wave-front and of retrieving fully diffraction-limited images of the objects (Léna and Lai, 1999a), nevertheless, the system began to produce a wide variety of astrophysical results, viz., (i) studying of the planetary meteorology (Poulet and Sicardy, 1996, Marco et al., 1997, Roddier et al., 1997); images of Neptune's ring arcs are obtained (Sicardy et al., 1999) that are interpreted as gravitational effects by one or more moons, (ii) imaging of the nucleus of M31 (Davidge et al., 1997a), (iii) surveying of young stars and multiple star systems (Bouvier et al., 1997), (iv) resolving the galactic centre (Davidge et al., 1997b), (v) imaging of Seyfert galaxies, QSO host galaxies (Hutchings et al., 1998a, 1998b), and (vi) mapping of the circumstellar environment (Roddier et al., 1996) etc. Most of the results obtained so far are from the arena of near IR band (Léna, 1997, Léna and Lai, 1999b); the results from the area of visible wave length are continued to be sparse.

In a recent article, Rouan (1996, and references therein) addressed many interesting results obtained with the AO systems at CFHT, as well as with the systems at 3.6 m ESO telescope; the results obtained in the near IR images of (a) NGC3690, one component of the Ultra Luminous system of merging galaxies Arp 299 (allowing to separate the nucleus and several compact sources), (b) the starburst/AGN galaxy NGC863, NGC7469, NGC1365, NGC1068, and (c) R136 in the 30 Doradus complex of the LMC depict the spectacular resolutions. From the diffraction-limited near IR images of the nucleus of

NGC1068 obtained with the AO system, PUEO, at CFHT, Rouan et al., (1998), found several components that include: (i) an unresolved conspicuous core, (ii) an elongated structure, and (iii) large and small scale spiral structures.

By means of AO imaging technique, Roddier et al., (1996) have detected a binary system consisting of a K7-MO star with an M4 companion that rotates clockwise. According to them, the system might be surrounded with a warm unresolved disk. High resolution AO imagery of the massive star Sand-66°41 in the LMC enabled Heydari and Beuzit (1994) to resolve it into 12 components. In order to perform differential photometry on close binary stars, Brummelaar et al., (1996) used a medium size 1.5 m telescope equipped with a laser guide star and AO system; the effective temperatures and the spectral types were determined for the secondaries of seven systems. Brandner et al., (1995) have resolved the close companion (sep. 0.128″) to NX Pup using the AO system at ESO 3.6 m telescope and opined that the NX Pup B might be a pre-main sequence star, which is exhibiting strong IR excess.

Brandl et al., (1996) have reported 0.15″ resolution near IR imaging of the R136 star cluster in 30 Doradus (LMC), an unusual high concentration of massive and bright O, B, Wolf-Rayet stars, with ESO 3.6 m telescope equipped with the AO system, ADONIS. Over 500 stars are detected within the field of view 12.8″ × 12.8″ covering a magnitude range of 11.2; ∼ 110 are reported to be red stars.

The improved resolution of crowded fields like globular clusters using AO systems would enable to derive luminosity functions and spectral types, to analyse proper motions in their central area etc. Simon et al., (1999) have detected 292 stars in the dense Trapezium star cluster of the Orion nebula and resolved pairs to the diffraction limit of the 2.2 m University of Hawaii telescope using University of Hawaii (UH) AO system. Using both the speckle masking technique and AO system, respectively at ESO 2.2 m and ESO 3.6 m telescopes, quasi-simultaneous observations of the close Herbig Ae/Be binary star NX Pup, associated with the cometary globular cluster I, in the optical and near IR bands, Schöller et al., (1996) estimated the mass and age of both the components, NX Pup A and B. The circumstellar matter around the former, according to them, could be described by a viscous accretion disk.

Bedding et al., (1997b) have applied AO systems to study the resolved stellar populations in galaxies with the ESO 3.6 m telescope using ADONIS systems; observations of several systems including the Sgr window in the bulge of the milky way were made. In spite of small area covered, they were able to produce a infrared luminosity function and colour-magnitude diagram for 70 stars down to ≃ 19.5. These are the deepest yet measured for the galactic bulge, reaching beyond the turn-off. The marked advantage over traditional approach is the usages of near IR region, where the peak of the spectral energy distribution for old populations is found by them. Figure 24 depicts the ADONIS K′ image of the Sgr window.
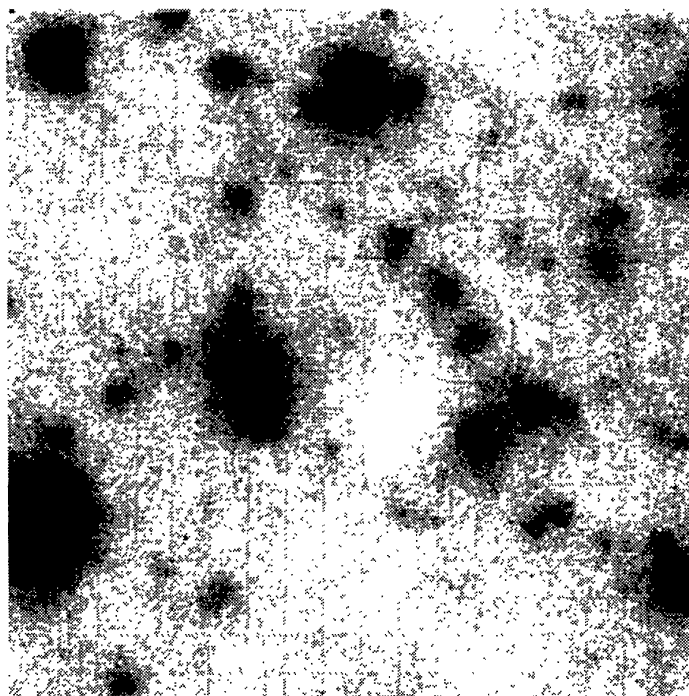
Figure 24. The ADONIS K' image of the Sgr window in the bulge of the milky way (Bedding et al., 1997b). The image is $8'' \times 8''$ (Courtesy: T. Bedding).

AO systems have been used to observe extragalactic objects; imaging of central area of active galaxies where cold molecular gas and star formation occur is an important programme. High spatial resolution images of star forming region Messier 16 (Currie et al., 1996), the reflection nebula NGC2023 in Orion (Rouan et al., 1997) have been obtained with the ESO 3.6 m telescope equipped with ADONIS AO system. Observations of the latter revealed small scale structure in the associated molecular cloud, close to the exciting star. Close et al., (1997) have mapped near IR polarimetric observations of the reflection nebula R Monocerotis using UH AO system of CFHT. They have detected a faint source, $0.69''$ away from R Mon and identified it as a T Tauri star. Lai et al., (1998) have recorded images of Markarian 231, a galaxy 160 Mpc away with PUEO AO system at the said telescope, demonstrating the limits of achieving in terms morphological structures on distant objects. The same system has also been used to image the nuclear region of NGC3690 in the interacting galaxy Arp 299 (Lai et al., 1999).

Aretxaga et al., (1998) reported the unambiguous detection of the host galaxy of a normal radio-quiet QSO at high-redshift in K-band using the AO system at the ESO 3.6 m telescope. Observations of the $z = 3.87$, broad absorption line quasar APM08279+5255 (Irwin et al., 1998) with the AOB of the CFHT, Ledoux et al., (1998) found the object to be a double source (separation $= 0.35'' \pm 0.02''$; intensity ratio $= 1.21 \pm 0.25$ in H band). They opined in favour of gravitational lensing hypothesis which came from the uniformity of the quasar spectrum as a function of the spatial position in the image obtained with the spectrograph, OASIS, at the same telescope. Search for molecular gas in high red-shift

normal galaxies in the foreground of the gravitationally lensed quasar Q1208+1011 has also been made (Sams et al., 1996).

From the observations with ADONIS adaptive optics system with infrared cameras on the 3.6 m ESO telescope, Monnier et al., (1999) found a variety of dust condensations that include a large scattering plume, a bow shaped dust feature around the red supergiant VY CMa. A bright knot of emission $1''$ away from the star is also reported. In view of the afore-mentioned findings, the authors argued in favour of the presence of chaotic and violent dust formation processes around the star. The AO system at CFHT has also been used for searching brown dwarfs and giant planets (Walker et al., 1998). AO imaging of proto-planetary nebulae (PPN), Frosty Leo and the Red Rectangle were also reported by Roddier et al., (1995). In both cases, they found a binary star at the origin of these PPNs and argued in favour of the mechanism proposed by Morris (1987) for the formation of bipolar PPN.

Another novel method of using coronographic mode has been tried recently with the AO system at the 3.6 m ESO telescope to observe α CMa (Malbet, 1995). The noted advantages of the on-line occulting mask system (Labeyrie, 1975, Bhattacharyya and Rajamohan, 1990, Roddier and Roddier, 1997, Prieur et al., 1998) are the reduction of the light coming from the central star, and filtering out of the light at low spatial frequency; the remaining light at the edge of the pupil corresponds to high frequencies. The high resolution imagery of a few interesting objects by means of the AO coronographic method detected a very low mass companion to the astrometric binary Gliese 105 A (Golimowski et al., 1995).

Mouillet et al., (1997) have applied the same technique to record the images of proto-planetary disk around the star β Pictoria at the 3.6 m ESO telescope; a warp of the disc is detected. Images of the nebula around LBV AG Carina, with the John Hopkins AO coronograph at the 1 m telescope, in the Hα and N II revealed the presence of highly asymmetric features in AG Carina's circumstellar environment (Nota et al., 1992). Imaging of the bipolar nebula around the LBV R127 has also been reported by Clampin et al., (1993). Nakajima and Golimowski, (1995) have obtained very high contrast images of several pre-main sequence stars and noticed the remnant envelope of star formation.

A new technique has been proposed by Labeyrie, (1995), called dark speckles method exploiting the light cancelation effect in random field (highly destructive interferences may occur occasionally depicting near black spots in the speckle pattern). The technique, which features the combination of both speckle interferometry and AO system, may improve the possibility of detecting faint companions of stars. Recently, Boccaletti et al., (1998a) have found from the laboratory simulations the capability of detecting a stellar companion of relative intensity 10^6 at 5 Airy radii from the star using an avalanche photodiode as detector. They also have recorded dark speckle data at the 1.52 m telescope of Haute-Provence using an AO system and detected a faint component of the spectroscopic binary star HD144217 ($\Delta m = 4.8$, separation $= 0.45''$). Subsequently, Boccaletti et al., (1998b) have applied the same technique at the said telescope to observe the relatively

faint companions of δ Per and η Psc and were able to estimate of their position and magnitude difference.

10.3. Results obtained with diluted aperture interferometry

Considerable amount of astrophysical results, viz., (i) diameters (Labeyrie, 1985) (ii) effective temperatures of giant stars (Faucherre et al., 1983), (iii) resolving the gas envelope of the Be star γ Cassiopeiae in the Hα line (Thom et al., 1986), (iv) diameters of cool bright giants and their effective temperature at 2.2 μm (DiBenedetto and Rabbia, 1987) etc., have been obtained from interference fringes recorded using I2T interferometer at Observatoire de Calern (section 9.2.1). The angular diameter for more than 50 stars have been measured (DiBenedetto and Rabbia, 1987, Mozurkewich et al., 1991, Dyck et al., 1993) with accuracy better than 1% in some cases with the long baseline amplitude interferometers at optical and IR wavelengths.

The scientific programmes using GI2T are restricted by the low limiting magnitude down to 5 (seeing and visibility dependent) that include the Be stars, Luminous Blue variables, spectroscopic and eclipsing binaries, wavelength dependent objects, bright stars (measuring diameters), circumstellar envelope etc., (Mourard et al., 1992, Thureau et al., 1998). The reason for concentrating on low magnitude object is mainly due to the visual detection and tracking of the fringes. The noted results obtained so far in recent time with the said interferometer include the diameter of δ Cephei (Mourard et al., 1997), subtle structures in circumstellar environment such as, jets in the binary system β Lyrae (Harmanec et al., (1996), clumpiness in the wind of P Cygni (Vakili et al., 1997, 1998a); a rotating arm in ζ Tau (Vakili et al., 1998b).

The measurements of spectrally resolved visibilities of the emission-line star, γ Cassiopeiae (HD5394), with GI2T by Mourard et al., (1989) distinguish the hydrogen emission in the envelope from the continuum photospheric emission. With the central star as a reference (unresolved), they determined the relative phase of the shell visibility and showed clearly the rotation of the envelope. From the subsequent observations on later dates with the interferometer, Stee et al., (1995, 1998) derived the radiative transfer model for the star based on the spectroscopic and interferometric data. Figure 25 depicts the intensity maps from the model of the Be star γ Cassiopeiae of different Doppler shifts across the Hα emission line (Stee et al., 1995). Each map is computed within a spectral band of 0.4 nm; theoretical visibilities are computed from these maps and compared to GI2T data. Figure 26 depicts the global picture of circumstellar environment of the said star.

Using high spatial resolution data at Hα and He I (667.8 nm) emission lines, Vakili et al., (1997) resolved the extended envelope of the LBV, P Cygni, with the GI2T. Detection of a localized asymmetry at 0.8 mas to the south of the same star's photosphere has also been reported (Vakili et al., 1998a). Harmanec et al., (1996) reported the results on the interacting binary star β Lyr. Figure 27 depicts the jet-like structure of the said star (Stee, 1999).
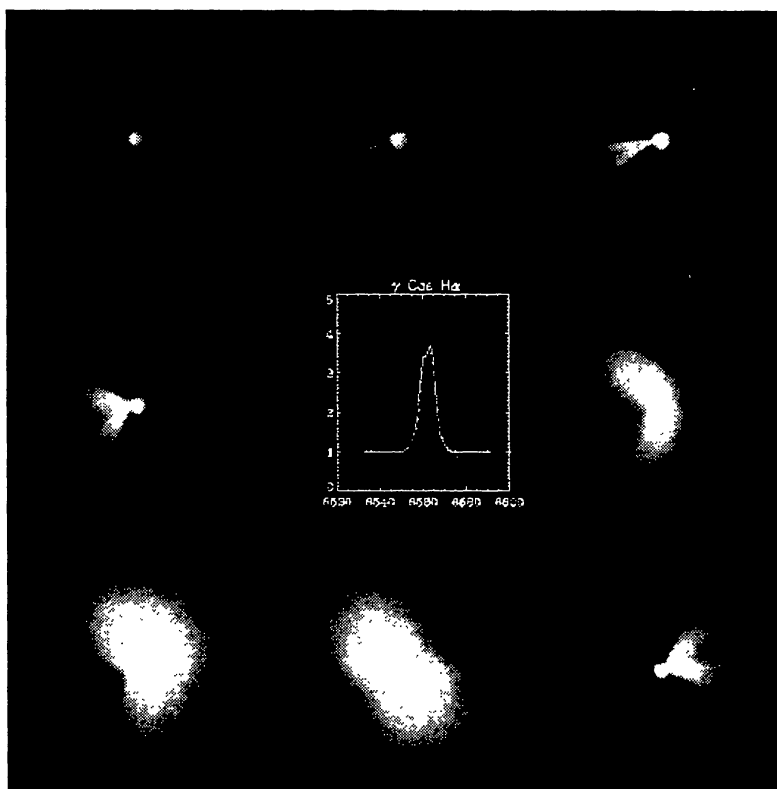
Figure 25. Intensity maps from the model of γ Cassiopeiae of different Doppler shifts across the Hα emission line (Courtesy: P. Stee).

Measurements of precise stellar positions and motions of the stars have been carried out with the mark III interferometer at Mt. Wilson. It was designed with the internal metrology to support its operation to obtain astrometric observations of several stars. Shao et al., (1990) have determined astrometric positions of 12 stars with 1σ errors 6 mas in declination and 10 mas in right ascension. Hummel (1994) reported the measurement of the position of 11 FK5 stars. This set up has also been used to derive the fundamental stellar parameters, like the orbits for spectroscopic binaries (Armstrong et al., 1992a, Pan et al., 1992), structure of circumstellar shells (Bester et al., 1991) etc. Armstrong et al., (1992a, 1992b) have determined the orbit of the double-lined spectroscopic binary stars, α Equulei, ϕ Cygni, as well as derived their masses and absolute magnitudes for its components. Observations of 5 eclipsing binary stars, β Aur, α CrB, β Per, ζ Aur, ϵ Aur, have been reported (Shao and Colavita, 1994).

The results obtained recently from the other long baseline amplitude interferometers can also be recorded here. With SUSI interferometer Davis et al., (1998, 1999b) have determined the diameter of δ CMa with an accuracy of $\pm 1.8\%$. Malbet et al., (1998) have resolved the young stellar object FU Orionis using the long baseline Palomar testbed interferometer in the near infrared with a projected resolution better than 2 AU. Observations of the young binary stars, ι Peg have been conducted by Pan et al., (1996)

A model for γ Cassiopeiae (B0.5IVe)

Optically thick lines

Fast radiative wind (2000km/s)

U.V lines

Keplerian
rotation

$T(r) \propto r$

Optically thin lines

Slow radiative
wind (200km/s)

Balmer lines

$e = 0.72$

Photosphere

Hα

Hβ   650 nm
continuum

480 nm
continuum

He 6678
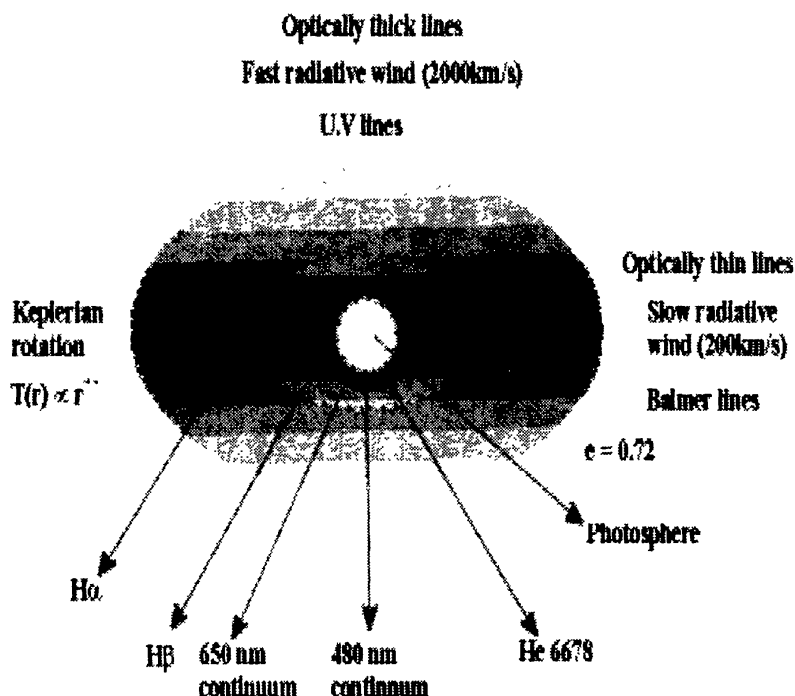
Figure 26. The global picture of circumstellar environment of γ Cassiopeiae (Courtesy: P. Stee).

with the testbed interferometer. They have determined its visual orbit with separation of 1 mas in R. A., having a circular orbit with a radii of 9.4 mas.

The measurements of closure phase together with the measurements of visibility amplitude allow one to reconstruct an image of the object. With the Cambridge optical aperture synthesis telescope (COAST), using a coherent array of 4 telescopes with 6 baselines (maximum baseline was 10 m), Baldwin et al., (1998) have resolved α Tau. Aperture synthesis maps of the double-lined spectroscopic binary α Aurigae obtained by Baldwin et al., (1996) with three elements of the same interferometer showed the milliarcsecond orbital motion of the system over a 15 day interval. Images of the resolved stellar disk of α Orionis depicting the presence of a circularly symmetric data with an unusual flat-topped and limb darkening profile have been reported (Burns et al., 1997). The variations of the cycle of pulsation of the angular size of the Mira variable R Leonis have also been measured with this interferometer directly (Burns et al., 1998). Pauls et al., (1998) have measured the limb darkened angular diameters of late-type giant stars using the Navy prototype interferometer with three optical elements; measurement of non-zero closure phase has been performed on a single star.

Though the visible light measurements from the IOTA long baseline interferometer have been reported (Coldwell et al., 1998), most of the results obtained so far are from the IR wave bands, particularly at near IR bands. They are in the form of measuring the
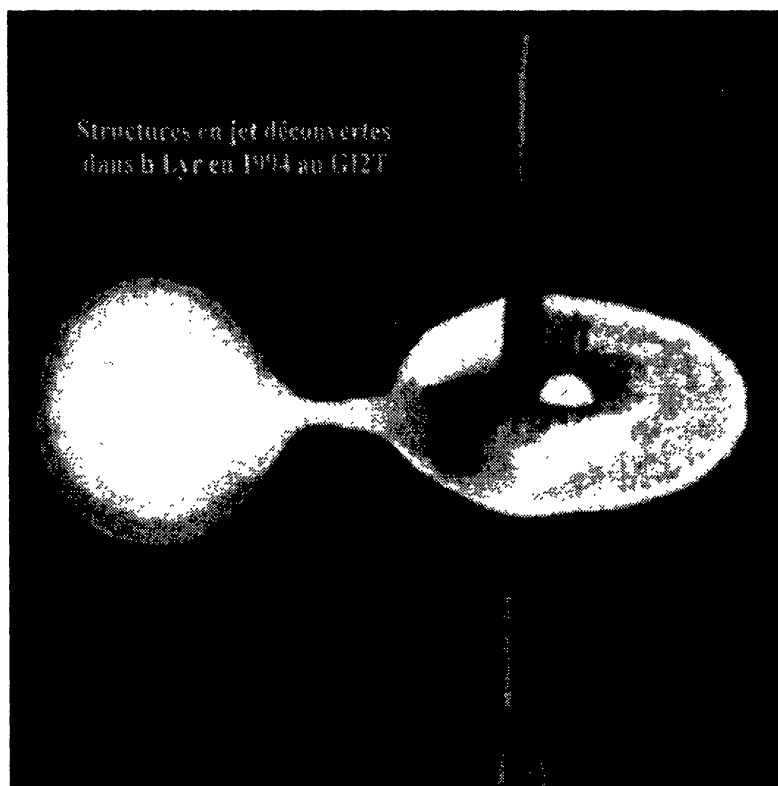
Figure 27. Jet-like structure of β Lyr (Stee, 1999, Courtesy: P. Stee).

angular diameters and effective temperatures of carbon stars (Dyck et al., 1996a), carbon Miras and S types (van Belle et al., 1997), K and M giants and supergiants (Dyck et al., 1996b, 1998, Perrin et al., 1998), Mira variables (van Belle et al., 1996), and cool giant stars (Dyck et al., 1995). Evidence of circumstellar dust and gas shell around two stars, RS Cnc, RX Boo, were also reported (Dyck et al., 1995).

11. Epilogue

Turbulence in the atmosphere restricts the resolution of optical telescopes to about $1''$, irrespective of their sizes ($D > 10$ cm). The deployment of space-bound telescopes may improve the resolving power to its diffraction limit but the size and the cost of such a venture is its shortcoming. The understanding of the basic random interference phenomenon − speckle − is of paramount importance to observational astronomy. In recent years the uses of speckle pattern and a wide variety of applications have been found in many other branches of physics and engineering. Though the statistical properties of speckle pattern is complicated, detailed analysis of this is useful in information processing.

The single aperture speckle interferometric technique has made a major break-through in observational astronomy by counteracting the deleterious effect of the atmosphere on the structure of stellar images. A host of basic problems need high angular resolution for

their solution. This may be in the form of measuring the separation of the components of close binaries, mapping the finer features of certain types of circumstellar envelopes, resolving the central core of AGNs and gravitationally lensed QSOs etc. Studies of the morphology of stellar atmospheres, the circumstellar environment of nova or supernova, YPN, long period variables (LPV), rapid variability of AGNs etc. are of paramount importance in astrophysics. Details of the structure of a wide range of stellar objects at scales of $0.015''$ - $0.03''$ are routinely observed. The physical properties of red dwarfs in the vicinity of sun can also be looked into; some dwarfs may often be close binaries. Speckle interferometric technique has been extended to IR domain too. With the photon counting detector system which is an essential tool in the application of optical interferometric imaging that allows the accurate photon centroiding, as well as provides dynamic range needed for measurements of source characteristics, one can record the specklegrams of the object of faintest limiting magnitude.

With the image reconstruction algorithms, which preserve the phase in the object Fourier transform permits true image restoration. Recently, phase-diversity technique (Gonsalves, 1982, Paxman et al., 1992) that uses two simultaneous short-exposure images taken at different focus/defocus positions near the focal plane has found to be promising . method in astronomy (Baba et al., 1994c, Seldin and Paxman, 1994). The single aperture interferometry by means of various other techniques too brought considerable amount of results.

Adaptive optics technology has become an affordable tool at all new large astronomical telescopes. This technique has been able to bring many new results not only in the field of observational astronomy, but in other branches of physics as well. Liang et al., (1997) have constructed a fundus camera equipped with adaptive optics allowing the imaging of microscopic size of single cell in the living human retina. They have exhibited that eyes with adaptive optics correction can resolve fine gratings that were invisible under normal viewing conditions. Observations using AO system on large telescopes of 10 m class could surpass the resolution achievable with the present day orbital telescope.

Though the stellar speckle interferometry is capable of detecting relatively faint objects ($\sim$ 16th. magnitude), the angular resolution is limited by the diameter of the telescope. On the other hand, the angular resolution of any stellar object in the visible wavelength can vastly be improved by using long baseline interferometry. Among others, this technique can detect the morphological details, viz., (i) granulations, (ii) oblateness etc. of giant stars. Eclipsing binaries (Algol type) which show evidence of detached gas rings around the primary are also good candidates for long baseline interferometry. The potential of this type of interferometer can be envisaged in determining the fundamental astrophysical informations of circumstellar envelopes such as, the diameter of inner envelope, colour, symmetry, radial profile etc.

Several long baseline interferometers are either in operation or under development at various stages. Rapid increase in the scientific output at optical, as well as at infrared wave bands using these interferometers can be foreseen at the fall of the next millennium. With improved technology, the long baseline interferometric arrays of large telescopes fitted

with high level adaptive optics system that applies dark speckle coronograph (Boccaletti et al., 1998b) may provide snap-shot images at their recombined focus using the concept of densified-pupil imaging (Pedretti and Labeyrie, 1999), and yield improved images and spectra of objects. One of the key areas where the new technology would make significant contributions is the astrometric detection and characterisation of exo-planets.

References

Acton D. S., Smithson R. C., 1992, Appl. Opt., 31, 3161.

Afanas'jev V. S., Balega I. I., Balega Y. Y., Vasyuk V. A., Orlov V. G., 1988, Proc. ESO-NOAO conf. 'High Resolution Imaging Interferometry', ed., F. Merkle, Garching bei München, FRG, 127.

Afanasiev V. L., Balega Y. Y., Orlov V. G., Vasyuk V. A., 1992, Proc. ESO-NOAO conf. 'High Resolution Imaging Interferometry', ed., J. M. Beckers & F. Merkle, Garching bei München, FRG, 53.

Aime C., 1976, A & A, 47, 5.

Aime C., Petrov R., Martin F., Ricort G., Borgnino J., 1985, Proc. SPIE., 556, 297.

Aime C., Ricort G., Grec G., 1975, A & A, 43, 313.

Aime C., Ricort G., Grec G., 1977, A & A, 54, 505.

Aime C., Ricort G., Harvey J. W., 1978, Ap J, 221, 362.

Anderson J. A., 1920, Ap J, 51, 263.

Aretxaga I., Mignant D. L., Melnick J., Terlevich R. J., Boyle B. J., 1998, astro-ph/9804322, MNRAS.

Aristidi É., Carbillet M., Prieur J. -L., Lopez B., Bresson Y., 1997, A & AS, 126, 555.

Aristidi É., Prieur J. -L., Scardin M., Koechlin L., Avila R., Carbillet M., Lopez B., Rabbia Y., Nisenson P., Gezari D., 1999, A & AS, 134, 545.

Armstrong J. T., 1994, Proc. SPIE., 2200, ed. J. B. Breckinridge, 62.

Armstrong J. T., Hummel C. A., Mozurkewich D., 1992a, Proc. ESO-NOAO conf. 'High Resolution Imaging Interferometry', ed., J. M. Beckers & F. Merkle, Garching bei München, FRG, 673.

Armstrong J. T., Mozurkewich D., Vivekanand M., Simon R. S., Denison C. S., Johnston K. J., Pan X. -P., Shao M., Colavita M. M., 1992b, A J, 104, 241.

Arsenault R., Salmon D. A., Kerr J., Rigaut F., Crampton D., Grundmann W. A., 1994, SPIE conf., 2201, 883.

Ayers G. R., Dainty J. C., 1988, Opt. Lett., 13, 457.

Ayers G. R., Northcott M. J., Dainty J. C., 1988, J. Opt. Soc. Am. A., 5, 963.

Baba N., Kuwamura S., Miura N., Norimoto Y., 1994b, Ap J, 431, L111.

Baba N., Kuwamura S., Norimoto Y., 1994a, App. Opt., 33, 6662.

Baba N., Tomita H., Miura N., 1994c, App. Opt., 33, 4428.

Babcock H. W., 1953, PASP, 65, 229.

Bagnuolo Jr. W. G., Mason B. D., Barry D. J., Hartkopf W. I., McAlister H. A., 1992, A J, 103, 1399.

Baier G., Weigelt G., 1987, A & A, 174, 295.

Baldwin J. E., 1992, Proc. ESO-NOAO conf. 'High Resolution Imaging Interferometry', ed., J. M. Beckers & F. Merkle, Garching bei München, FRG, 747

Baldwin J. E., Beckett R. C., Boysen R. C., Burns D., Buscher D. F., Cox G. C., Haniff C. A., Mackay C. D., Nightingale N. S., Rogers J., Scheuer P. A. G., Scott T. R., Tuthill P. G., Warner P. J., Wilson D. M. A., Wilson R. W., 1996, A & A, 306, L13.

Baldwin J. E., Boysen R. C., Cox G. C., Haniff C. A., Rogers J., Warner P. J., Wilson D. M. A., Mackay C. D., 1994, Proc. SPIE., on 'Amplitude and Intensity Spatial Interferometry II', 2200, 112.

Baldwin J. E., Boysen R. C., Haniff C. A., Lawson P. R., Mackay C. D., Rogers J., St-Jacques D., Warner P. J., Wilson D. M. A., Young J. S., 1998, Proc. SPIE., on 'Astronomical Interferometry', 3350, 736.

Baldwin J. E., Haniff C. A., Mackay C. D., Warner P. J., 1986, Nature, 320, 595.

Balega I. I., Balega Y. Y., Belkin I. N., Maximov A. E., Orlov V. G., Pluzhnik E. A, Shkhagosheva Z. U., Vasyuk V. A., 1994, A & AS, 105, 503.

Balega I. I., Balega Y. Y., Falcke, H., Osterbart R., Reinheimer T., Schöeller M., Weigelt G., 1997a, Astron. Letters, 23, 172.

Balega I. I., Balega Y. Y., Falcke, H., Osterbart R., Schöeller M., Weigelt G., 1997b, in Visual Double Stars: Formation, dynamics and evolutionary tracks, eds. J. A. Docobo, A. Elipe, H. McAlister, Astrophysics and Space Science Library, Kluwer Acad. Publ. Dordrecht, Boston, London, 223, 73.

Balega Y. Y., Balega I. I., 1985, Sov. Astron., 11, 47.

Balega Y., Blazit A., Bonneau D., Koechlin L., Foy R., Labeyrie A., 1982, A & A, 115, 253.

Balega Y., Bonneau D., Foy R., 1984, A & AS, 57, 31.

Balick B., 1987, A J, 94, 671.

Barakat R., Nisenson P., 1981, J. Opt. Soc. Am., 71, 1390.

Barletti R., Ceppatelli G., Paterno L., Righini A., Speroni N., 1976, J. Opt. Soc. Am., 66, 1380.

Barlow M. J., Morgan B. L., Standley C., Vine H., 1986, MNRAS, 223, 151.

Barr L. D., Fox J., Poczulp G. A., Roddier C. A., 1990, Proc. SPIE, 1236, 492.

Bates R. H. T., Davey B. L. K., 1988, Proc. NATO-ASI, 'Diffraction Limited Imaging with Very Large Telescopes', ed. D. M. Alloin & J. -M. Mariotti, Cargése, France, 293.

Bates R.H.T., McDonnell M.J., 1986, 'Image Restoration and Reconstruction', Oxford Engineering Science, Clarendon Press, Oxford.

Beckers J. M., 1982, Opt. Acta., 29, 361.

Beckers J. M., 1988, ESO Conf. on 'Very Large Telescopes and their Instrumentation', ed. M.-H. Ulrich, 693.

Beckers J. M., 1993, Annual Rev. A & A, 31, 13.

Beckers J. M., 1999, 'Adaptive Optics in Astronomy', ed. F. Roddier, Cambridge Univ. Press, 235.

Beckers J. M., Hege E. K., Murphy H. P., 1983, Proc. SPIE, 444, 85.

Bedding T. R., 1999, astro-ph/9901225, PASP (to appear).

Bedding T. R., Minniti D., Courbin F., Sams B., 1997b, A & A, 326, 936.

Bedding T. R., Robertson J. G., Marson R. G., 1994, A & A, 290, 340.

Bedding T. R., Robertson J. G., Marson R. G., Gillingham P. R., Frater R. H., O'Sullivan J. D., 1992, Proc. ESO-NOAO conf. 'High Resolution Imaging Interferometry', ed., J. M. Beckers & F. Merkle, Garching bei München, FRG, 391.

Bedding T. R., Zijlstra A. A., Von der Lühe O., Robertson J. G., Marson R. G., Barton J. R., Carter B. S., 1997a, MNRAS, 286, 957.

Beletic J. W., 1988, Proc. ESO-NOAO conf. 'High Resolution Imaging Interferometry', ed., F. Merkle, Garching bei München, FRG, 357.

Beletic J. W., 1996, 'Adaptive Optics' OSA Technical Digest series, 13, 216.

Beletic J. W., Goody R. M., Tholen D. J., 1989, Icarus, 79, 38.

Berio P., Vakili F., Mourard D., Bonneau D., 1998, A & AS, 129, 609.

Bester M., Danchi W. C., Degiacomi C. G., Townes C. H., 1991, Ap J, 367, L27.

Bhattacharyya J. C., Rajamohan R., 1990, VBT News, No. 4., 1.

Blazit A., 1986, Proc., 'Image Detection and Quality' - SFO, ed., SPIE, 702, 259.

Blazit A., Bonneau D., Foy R., 1987, A & AS, 71, 57.

Blazit A., Bonneau D., Koechlin L., Labeyrie A., 1977a, Ap J, 214, L79.

Blazit A., Bonneau D., Jose M., Koechlin L., Labeyrie A., Onéto J. L., 1977b, Ap J, 217, L55.

Close L. M., Roddier F., Hora J. L., Graves J. E., Northcott M. J., Roddier C., Hoffman W. F., Doyal A., Fazio G. G., Deutsch L. K., 1997, Ap J, 489, 210.

Cognet M., 1973, Opt. Communication, 8, 430.

Colavita M., Shao M., Staelin D. H., 1987, App. Opt., 26, 4106.

Colavita M., Boden A. F., Crawford S. L., Meinel A. B., Shao M., Swanson P. N., van Belle G. T., Vasisht G., Walker J. M., Wallace J. K., Wizinowich P. L., 1998, Proc. SPIE conf. on 'Astronomical Interferometry', 3350, 776.

Coldwell C. M., Papaliolios C. D., Traub W. A., 1998, Proc. SPIE conf. on 'Astronomical Interferometry', 3350, 424.

Cole W. A., Fekel F. C., Hartkopf W. I., McAlister H. A., Tomkin J., 1992, A J, 103, 1357.

Cornwell T. J., 1987, A & A, 180, 269.

Coulman C. E., 1969, Solar Phys., 7, 122.

Coulman C. E., 1974, Solar Phys., 34, 491.

Coulman C. E., 1985, Ann. Rev. A & A, 23, 19.

Cruzalébes P., Tessier E., Lopez B., Eckart A., Tiphéne D., 1996, A & AS, 116, 597.

Cuby J. -G., Richard J. -C., Lemonier M., 1990, Proc. SPIE., 1235, 294.

Currie D. Kissel K., Shaya E., Avizonis P., Dowling D., Bonnacini D., 1996, The Messenger, no. 86, 31.

Dainty J. C., 1975, 'Laser Speckle and Related Phenomena', ed., J. C. Dainty, Springer-Verlag, N Y., 255.

Davidge T. J., Rigaut F., Doyon R., Crampton D., 1997a, A J, 113, 2094.

Davidge T. J., Simons D. A., Rigaut F., Doyon R., Becklin E. E., Crampton D., 1997b, A J, 114, 2586.

Davis J., 1994, Proc. IAU Symposium No., 158, 135.

Davis J., Tango W. J., 1985a, Proc. Astr. Soc. Australia, 6(1), 34.

Davis J., Tango W. J., 1985b, Proc. Astr. Soc. Australia, 6(1), 38.

Davis J., Tango W. J., 1986, Nature, 323, 234.

Davis J., Tango W. J., 1996, PASP., 108, 456.

Davis J., Tango W. J., Booth A. J., Minard R. A., Brummelaar t. T. A., Shobbrook R. R., 1992, Proc. ESO-NOAO conf. 'High Resolution Imaging Interferometry', ed., J. M. Beckers & F. Merkle, Garching bei München, FRG, 741.

Davis J., Tango W. J., Booth A. J., O'Byrne J. W., 1998, Proc. SPIE conf. on 'Astronomical Interferometry', 3350, 726.

Davis J., Tango W. J., Booth A. J., Brummelaar t. T. A., Minard R. A., Owens S. M., 1999a, MNRAS, 303, 773.

Davis J., Tango W. J., Booth A. J., Thorvaldson E. D., Giovannis J., 1999b, MNRAS, 303, 783.

Denker C., 1998, Solar Phys., 81, 108.

Denker C., de Boer C. R., Volkmer R., Kneer F., 1995, A & A, 296, 567.

DiBenedetto G. P., Conti G., 1983, Ap J, 268, 309.

DiBenedetto G. P., Rabbia Y., 1987, A & A, 188, 114.

Douglass G. G., Hindsley R. B., Worley C. E., 1997, Ap JS, 111, 289.

Drummond J., Eckart A., Hege E. K., 1988, Icarus, 73, 1.

Duquennoy A., Tokovinin A. A., Leinert CH., Glindemann A., Halbwachs J. L., Mayor M., 1996, A & A, 314, 846.

Durand D., Hardy E., Couture J., 1987, Astron. Soc. Pacific, 99, 686.

Dyck H. M., Benson J. A., Carleton N. P., Coldwell C. M., Lacasse M. G., Nisenson P., Panasyuk A. V., Papaliolios C. D., Pearlman M. R., Reasenberg R. D., Traub W. A., Xu X., Predmore R., Schloerb F. P., Gibson D., 1995, A J, 109, 378.

Dyck H. M., Benson J. A., Ridgway S. T., 1993, PASP, 105, 610.

Dyck H. M., Benson J. A., van Belle G. T., Ridgway S. T., 1996b, A J, 111, 1705.

Dyck H. M., van Belle G. T., Benson J. A., 1996a, A J, 112, 294.

Dyck H. M., van Belle G. T., Thomson R. R., 1998, A J, (to appear).

Ebstein S., Carleton N. P., Papaliolios C., 1989, Ap J, 336, 103.

Falcke H., Davidson K., Hofmann K. -H., Weigelt G., 1996, A & A, 306, L17.

Faucherre M., Bonneau D., Koechlin L., Vakili F., 1983, A & A, 120, 263.

Fienup J. R., 1978, Opt. Lett., 3, 27.

Fienup J. R., 1984, Proc. SPIE., 373, 147.

Fischer O., Stecklum B., Leinert Ch., 1998, A & A, 334, 969.

Fizeau H., 1868, C. R. Acad. Sci. Paris, 66, 934.

Foy R., 1988, Proc., 'Instrumentation for Ground Based Optical Astronomy - Present and Future', ed., L. Robinson, Springer Verlag, New York, 345.

Foy R, 1992, Proc. ESO-NOAO conf. 'High Resolution Imaging Interferometry', ed., J. M. Beckers & F. Merkle, Garching bei München, FRG, 5.

Foy R, 1996, Proc. NATO-ASI, 'High Resolution in Astrophysics', Les Houches, France, ed. A. M. Lagrange, D. Mourard & P. Léna, 193.

Foy R., Bonneau D., Blazit A., 1985, A & A, 149, L13.

Foy R., Labeyrie A., 1985, A & A, 152, L29.

Fried D. C., 1966, J. Opt. Soc. Am., 56, 1972.

Fugate R. Q., Fried D. L., Ameer G. A., Boeke B. R., Browne S. L., Roberts P. H., Roberti P. H., Ruane R. E., Tyler G. A., Wopat L. M., 1991, Nature, 353, 144.

Gauger A., Balega Y. Y., Irrgang P., Osterbart R., Weigelt G., 1999, A & A, 346, 505.

Gerchberg R. W., Saxton W. O., 1972, Optik, 35, 237.

Germain M. E., Douglass G. G., Worley C. E., 1999, A J, 117, 1905.

Gies R. D., Mason B. D., Bagnuolo W. G. (Jr.), Haula M. E., Hartkopf W. I., McAlister H. A., Thaller M. L., McKibben W. P., Penny L. R., 1997, Ap. J., 475, L49.

Gillingham P. R., 1984a, in 'Very Large Telescopes, their Instrumentation and Programs', IAU Colloq. no. 79, ESO, ed., M. -H. Ulrich & Kjär, Garching bei München, FRG, 415.

Gillingham P. R., 1984b, 'Advanced Technology Optical Telescopes II', ed., L. D. Barr & B. Mark, Proc. SPIE, 444, 165.

Glindemann A., 1997, PASP, 109, 682.

Glindemann A., Lane R. G., Dainty J. C., 1991, Proc. 'Digital Signal Processing', ed., V. Cappellini & A. G. Constantinides, 59.

Glindemann A., Lane R. G., Dainty J. C., 1992, Proc. ESO-NOAO conf. 'High Resolution Imaging Interferometry', ed., J. M. Beckers & F. Merkle, Garching bei München, FRG, 243.

Glindemann A., McCaughrean M. J., Hippler S., Birk C., Wagner K., Rohloff R. -R., 1997, PASP, 109, 688.

Goecking K. D., Duerbeck H. W., Plewa T., Kaluzny J., Scherti D., Weigelt G., Flin P., 1994, A & A, 289, 827.

Golimowski D. A., Nakajima T., Kulkarni S. R., Oppenheimer B. R., 1995, Ap J, 444, L101.

Gonsalves S. A., 1982, Opt. Engr., 21, 829.

Goodman J. W., 1968, 'Introduction to Fourier Optics', McGraw Hill, N. Y.

Goodman J. W., 1975, in 'Laser Speckle and Related Phenomena', ed., J. C. Dainty, Springer-Verlag, Berlin, 9.

Goodman J. W., 1985, 'Statistical Optics', Wiley, N. Y.

Graves J. E., Northcott M. J., Roddier C., Roddier F., Anuskiewicz J., Monet G., Rigaut F., Madec P. Y., 1993, Proc. ICO-16 Satellite Conf. on "Active and Adaptive Optics" ed. F. Merkle, Garching bei München, Germany, 47.

Grieger F., Fleischman F., Weigelt G. P., 1988, Proc. ESO-NOAO conf. 'High Resolution Imaging Interferometry', ed. F. Merkle, Garching bei München, FRG, 225.

Grieger F., Weigelt G., 1992, Proc. ESO-NOAO conf. 'High Resolution Imaging Interferometry', ed., J. M. Beckers & F. Merkle, Garching bei München, FRG, 481.

Haniff C. A., Busher D. F., 1992, J. Opt. Soc. Am. A., 9, 203.

Haniff C. A., Busher D. F., Christou J. C., Ridgway S. T., 1989, MNRAS, 241, 694.

Haniff C. A., Ghez A. M., Gorham P. W., Kulkarni S. R., Mathews K., Neugebauer G., 1992, A J, 103, 1662.

Haniff C. A., Mackay C. D., Titterington D. J., Sivia D., Baldwin J. E., Warner P. J., 1987, Nature, 328, 694.

Haniff C. A., Scholz M., Tuthill P. G., 1995, MNRAS, 276, 640.

Harding G. A., Mack B., Smith F. G., Stokoe J. R., 1979, MNRAS, 188, 241.

Hardy J. W., Lefebvre J. E., Koliopoulos C. L., 1977, J. Opt. Soc. Am., 67, 360.

Hardy J. W., MacGovern A. J., 1987, Proc. SPIE, 816, 180.

Harmanec P., Morand F., Bonneau D., Jiang Y., Yang S., Guinan E. P., Hall D. S., Mourard D., Hadrava P., Bozic H., Sterken C., Tallon-Bosc I., Walker G. A. B., McCook P. M., Vakili F., Stee P., 1996, A & A, 312, 879.

Hartkopf W. I., Mason B. D., McAlister H. A., Turner N. H., Barry D. J., Franz O. G., Prieto, C.M. 1996, A J, 111, 936.

Hartkopf W. I., McAlister H. A., Mason B. D., 1997a, CHARA Contrib. No. 4, 'Third Catalog of Interferometric Measurements of Binary Stars', W.I.

Hartkopf W. I., McAlister H. A., Mason B. D., Brummelaar t. T., Roberts Jr., L. C., Turner N. H., Wilson J. W., 1997b, A J, 114, 1639.

Hartkopf W. I., McAlister H. A., Yang X., Fekel F. C., 1992, A J, 103, 1976.

Hartley M., Mcinnes B., Graham Smith F., 1981, Q. J. Astr. Soc., 22, 272.

Harvey J. W., 1972, Nature, 235, 90.

Harvey J. W., Breckinridge J. B., 1973, Ap J, 182, L137.

Harvey J. W., Schwarzschild M., 1975, Ap J, 196, 221.

Haas M., Leinert C., Richichi A., 1997, A & A, 326, 1076.

Hawley S. A., Miller J. S., 1977, Ap J, 212, 94.

Hebden J. C., Eckart A., Hege E. K., 1987, Ap J, 314, 690.

Hebden J. C., Hege E. K., Beckers J. M., 1986, Opt. Eng., 25, 712.

Hege E. K., Hubbard E. N., Strittmatter P. A., Worden S. P., 1981, Ap J, 248, 1.

Henry T. J., Soderblom D. R., Donahue R. A., Baliunas S. L., 1996, A J, 111, 439.

Hess S. L., 1959, Introduction to Theoretical Meteorology (Holt, New York).

Heydari M., Beuzit J. L., 1994, A & A, 287, L17.

The Hipparcos catalogue, 1997, ESA, SP-1200.

Hofmann K. -H., Mauder W., Weigelt G., 1992, Proc. ESO-NOAO conf. 'High Resolution Imaging Interferometry', ed., J. M. Beckers & F. Merkle, Garching bei München, FRG, 61.

Hofmann K. -H., Seggewiss W., Weigelt G., 1995, A & A, 300, 403.

Hofmann K. -H., Weigelt G., 1988, A & A, 203, L21.

Hofmann K. -H., Weigelt G., 1993, A & A, 278, 328.

Hogbom J., 1974, Ap. JS, 15, 417.

Horch E. P., Dinescu D. L., Girard T. M., van Altena W. F., López C. E., Franz O. G., 1996, A J, 111, 1681.

Horch E. P., Morgan J. S., Giaretta G., Kasle D. B., 1992, PASP, 104, 939.

Horch E. P., Ninkov Z., Slawson R. W., 1997, A J, 114, 2117.

Horch E. P., Ninkov Z., van Altena W. F., 1998, Proc. SPIE on 'Optical Astronomical Instrumentation', 3355, 777.

Horch E. P., Ninkov Z., van Altena W. F., Meyer R. D., Girard T. M., Timothy J. G., 1999, A J, 117, 548.

Horwitz B. A., 1990, Opt. Eng., 29, 1223.

Hummel C. A., 1994, IAU Symp. 158, 'Very high resolution imaging' ed., J. G. Robertson and W. J. Tango, 448.

Hutchings J. B., Crampton D., Morris S. L., Durand D., Steinbring E., 1998a, astro-ph/9812159 (to appear A J).

Hutchings J. B., Crampton D., Morris S. L., Steinbring E., 1998b, PASP, 110, 374.

Hutter D. J., 1994, Proc. SPIE., 2200, ed. J. B. Breckinridge, 81.

Irwin M. J., Ibata R. A., Lewis G. F., Totten E. J., 1998, Ap J, 505, 529.

Ishimaru A., 1978, 'Wave Propagation and Scattering in Random Media', Academic, N. Y.

Ivezić Z., Nenkova M., Elitzur M., 1997, User Manual for DUSTY, http://www.pa.uky.edu/moshe/dusty.

Iye M., Nishihara E., Hayano Y., Okada T., Takato N., 1992, PASP, 104, 760.

Iye M., Noguchi T., Torti Y., Mikami Y., Ando H., 1991, PASP, 103, 712.

Jaynes E. T., 1982, Proc. IEEE, 70, 939.

Jefferies S. M., Christou J. C., 1993, Ap J, 415, 862.

Jennison R. C., 1958, MNRAS, 118, 276.

Johanneson A., Bida T., Lites B. W., Scharmer G. B., 1992, A & A, 258, 572.

Kallistratova M. A., Timanovskiy D. F., 1971, Izv. Akad. Nauk. S S S R., Atmos. Ocean Phys., 7, 46.

Kaplan G. H., Hershey J. L., Hughes J. A., Hutter D. J., Johnston K. J., Mozurkewich D., Simon R. S., Colavita M. M., Shao M., Hines B. E., Staelin D. H., 1988, Proc. ESO-NOAO conf. 'High Resolution Imaging Interferometry', ed., F. Merkle, Garching bei München, FRG, 841.

Karbelkar S. N., Nityananda R., 1987, J A A, 8, 271.

Karovska M., Koechlin L., Nisenson P., Papaliolios C., Standley C., 1989, Ap J, 340, 435.

Karovska M., Nisenson P., 1992, Proc. ESO-NOAO conf. 'High Resolution Imaging Interferometry', ed., J. M. Beckers & F. Merkle, Garching bei München, FRG, 141.

Karovska M., Nisenson P., Noyes R., 1986b, Ap J, 308, 260.

Karovska M., Nisenson P., Papaliolios C., Boyle R. P., 1991, Ap J, 374, L51.

Karovska M., Nisenson P., Stachnik R. V., 1986a, A J, 92, 4.

Kasle D. B., Morgan J. S., 1991, Proc. SPIE on 'EUV, X-Ray and Gamma Ray Instrumentation for Astronomy II', 1549, 52.

Keller C. U., Johannesson A., 1995, A & A Suppl. Ser., 110, 565.

Keller C. U., Von der Lühe O., 1992a, Proc. ESO-NOAO conf. 'High Resolution Imaging Interferometry', ed., J. M. Beckers & F. Merkle, Garching bei München, FRG, 453.

Keller C. U., Von der Lühe O., 1992b, A & A, 261, 321.

Kinahan B. F., 1976, Ap J, 209, 282.

Klückers V. A., Edmunds G., Morris R. H., Wooder N., 1997, MNRAS, 284, 711.

Knox K. T., 1976, J. Opt. Soc. Am., 66, 1236.

Knox K. T., Thompson B. J., 1974, Ap J, 193, L45.

Koechlin L., Lawson P. R., Mourard D., Blazit A., Bonneau D., Morand F., Stee P., Tallon-Bosc I., Vakili F., 1996, App. Opt., 35, 3002.

Koechlin L., Morel S., 1998, A & A, (to appear).

Kolmogorov A., 1941a, in 'Turbulence', ed., S. K. Friedlander & L. Topper, 1961, Wiley-Inerscience, N. Y., 151.

Kolmogorov A., 1941b, in 'Turbulence', ed., S. K. Friedlander & L. Topper, 1961, Wiley-Inerscience, N. Y., 156.

Kolmogorov A., 1941c, in 'Turbulence', ed., S. K. Friedlander & L. Topper, 1961, Wiley-Inerscience, N. Y., 159.

Korff D., 1973, J. Opt. Soc. Am., 63, 971.

Koutchmy S., Belmahdi M., Coulter R. L., Démoulin P., Gaizauskas V., MacQueen R. M., Monnet G., Mouette J., Noëns J. C., November I. J., Noyes R. W., Sime D. G., Smartt R. N., Sovka J., Vial J. C., Zimmermann J. P., Zirker J. B., 1994, A & A, 281, 249.

Krishan V., Witta P. J., 1994, Ap J, 423, 172.

Kuwamura S., Baba N., Miura N., Hege E. K., 1993a, A J, 105, 665.

Kuwamura S., Baba N., Miura N., Noguchi M., Norimoto Y., 1993b, A J, 106, 2532.

Kuwamura S., Baba N., Miura N., Noguchi M., Norimoto Y., Isobe S., 1992, Proc. ESO-NOAO conf. 'High Resolution Imaging Interferometry', ed., J. M. Beckers & F. Merkle, Garching bei München, FRG, 461.

Labeyrie A., 1970, A & A, 6, 85.

Labeyrie A., 1974, Nouv. Rev. Optique, 5, 141.

Labeyrie A., 1975, Ap J, 196, L71.

Labeyrie A., 1978, AR A & A, 16, 77.

Labeyrie A., 1980, Proc. K P N O conf., 786.

Labeyrie A., 1985, 15th. Advanced Course, Swiss Society of Astrophys. and Astron., ed. A. Benz, M. Huber & M. Mayor, 170.

Labeyrie A., 1988, Proc. NATO-ASI, 'Diffraction Limited Imaging with Very Large Telescopes', ed. D. M. Alloin & J. -M. Mariotti, Cargése, France, 327.

Labeyrie A., 1995, A & A, 298, 544.

Labeyrie A., 1996, A & AS, 118, 517.

Labeyrie A., 1998a, 'Exo-earth discoverer, a free-flyer interferometer for snapshot imaging and coronography', Proc. Conf., 'Extrasolar planets: formation, detection and modeling', 27 April-1 May, 1998, Lisbon, Portugal, (to appear), http://www.obs-hp.fr.

Labeyrie A., 1998b, 'Direct searches: imaging, dark speckle and coronography', Proc. NATO-ASI, 'Planets outside the solar system', 5-15 May, 1998, Cargése, France, http://www.obs-hp.fr.

Labeyrie A., Koechlin L., Bonneau D., Blazit A., Foy R., 1977, Ap J, 218, L75.

Labeyrie A., Schumacher G., Dugué M., Thom C., Bourlon P., Foy F., Bonneau D., Foy R., 1986, A & A, 162, 359.

Lai O., Rouan D., Rigaut F., Arsenault R., Gendron E., 1998, A & A, 334, 783.

Lai O., Rouan D., Rigaut F., Doyon F., Lacombe F., 1999, A & A, (to appear).

Lampton M., Carlson C. W., 1979, Rev. Sci. Instrum., 50, 1093.

Lampton M., Siegmund O., Raffanti R., 1987, Rev. Sci. Instrum., 58, 2298.

Lane R. G., Bates R. H. T., 1987, J. Opt. Soc. Am. A, 4, 180.

Lawrence R. S., Ochs G. R., Clifford S. F., 1970, J. Opt. Soc. Am., 60, 826.

Lawrence T. W., Goodman D. M., Johansson E. M., Fitch J. P., 1992, App. Opt. 31, 6307.

Lawson P. R., 1994, App. Opt., 33, 1146.

Ledoux C., Théodore B., Petitjean P., Bremer M. N., Lewis G. F., Ibata R. A., Irwin M. J., Totten E. J., 1998, astro-ph/9810140, A & A. (to appear).

Leinert C., Haas M., 1989, A & A, 221, 110.

Leinert C., Richichi A., Haas M., 1997, A & A, 318, 472.

Lemonier M., Richard J. -C., Riou D., Fouassier M, 1988, Proc. SPIE., 'Underwater Imaging', 980, 27.

Léna P., 1997, Experimental Astr., 7, 281.

Léna P., Lai O., 1999a, 'Adaptive Optics in Astronomy', ed. F. Roddier, Cambridge Univ. Press, 351.

Léna P., Lai O., 1999b, 'Adaptive Optics in Astronomy', ed. F. Roddier, Cambridge Univ. Press, 371.

Liang J., Williams D. R., Miller D. T., 1997, J. Opt. Soc. Am. A, 14, 2884.

Lillard R. L., Schell J. D., 1994, Proc. SPIE, on 'Adaptive Optics in Astronomy', 2201, 740.

Liu Y. C., Lohmann A. W., 1973, Opt. Comm., 8, 372.

Lohmann A. W., Weigelt G. P., Wirnitzer B., 1983, App. Opt., 22, 4028.

Lopez B., 1991, 'Last Mission at La Silla, April 19 – May 8, on the Measure of the Wave-front Evolution Velocity', E S O Internal Report.

Love G. D., Major J. V., Purvis A., 1994, Opt. Lett., 19, 1170.

Love G. D., Gourlay J., 1996, Opt. Lett., 21, 1496.

Lowne C. M., 1979, MNRAS, 188, 249.

Lynds C. R., Worden S. P., Harvey J. W., 1976, Ap J, 207, 174.

Malbet F., 1995, astro-ph/9509072, A & AS.

Malbet F., Berger J. -P., Colavita M. M., Koresko C. D., Beichman C., Boden A. F., Kulkarni S. R., Lane B. F., Mobley D. W., Pan X. -P., Shao M., van Belle G. T., Wallace J. K., 1998, astro-ph/9808326, Ap. JL. (accepted).

Mali R. K., Bifano T. G., Vandelli N., Horenstein M. N., 1997, Opt. Eng., 36, 542.

Marco O., Encrenaz T., Gendron E., 1997, Planet Sp. Sci., 46, 547.

Mariotti J. -M., Denise C., Déric F., Ferrari M., Glindemann A., Koehler B., Levèque S., Paresce F., Schöller M., Tarenghi M., Verola M., 1998, Proc. SPIE on 'Astronomical Interferometry', Hawaii, 3350, 800.

Martin C., Jelinsky P., Lampton M., Malina R. F., Anger H. O., 1981, Rev. Sci. Instrum., 52, 1067.

Masciadri E., Vernin J., Bougeault P., 1999, A & AS, 137, 203.

Mason B. D., 1995, PASP, 107, 299.

Mason B. D., 1996, A J, 112, 2260.

Mason B. D., Douglass G. G., Hartkopf W. I., 1999, A J, 117, 1023.

Mason B. D., Gies D. R., Hartkopf W. I., Bagnuolo W. G., (Jr.), Brummelaar t. T., McAlister H. L., 1998, A J, 115, 821.

Mason B. D., Martin C., Hartkopf W. I., Barry D. J., Germain M. E., Douglass G. G., Worley C. H., Wycoff G. L., Brummelaar t. T., Franz O. G., 1999, A J, 117, 1890.

Mason B. D., McAlister H. L., Hartkopf W. I., Bagnuolo W. G., (Jr.), 1993, A J, 105, 220.

Mason B. D., Brummelaar t. T., Gies D. R., Hartkopf W. I., Thaller M. L., 1997, A J, 114, 2112.

Matson C. L., 1991, J. Opt. Soc. Am. A, 8, 1905.

Max C., 1994, Private communication.

McAlister H. A., 1988, Proc. ESO-NOAO conf. 'High Resolution Imaging Interferometry', ed. F. Merkle, Garching bei München, FRG, 3.

McAlister H. A., Bagnuolo W. G., Brummelaar t. T., Hartkopf W. I., Shure M. A., Sturmann L., Turner N. H., Ridgway S. T., 1998, Proc. SPIE on 'Astronomical Interferometry', Hawaii, 3350, 947.

McAlister H. A., Hartkopf W. I., Hutter D. J, Franz O. G., 1987, A J, 93, 688.

McAlister H. A., Hartkopf W. I., Franz O. G., 1990, A J, 99, 965.

McAlister H. A., Hartkopf W. I., Sowell J. R., Dombrowski E. G., Franz O. G., 1989, A J, 97, 510.

McAlister H. A., Hartkopf W. I., Mason B. D., Roberts L. C. (Jr.), Shara M. M., 1996, A J, 112, 1169.

McAlister H. A., Mason B. D., Hartkopf W. I., Shara M. M., 1993, A J, 106, 1639.

Meikle W. P. S., Matcher S. J., Morgan B. L., 1987, Nature, 329, 608.

Meng J. G., Aitken J. M., Hege E. K., Morgan J. S., 1990, J. Opt. Soc. Am. A, 7, 1243.

Men'shchikov A. B., Balega Y. Y., Osterbart R., Weigelt G., 1998, New Astr., 3, 601.

Men'shchikov A. B., Henning Th., 1997, A & A, 318, 879.

Mertz L., 1970, 'Transformations in Optics', ed. J. Wiley & Sons, 16.

Metcalf J. L., 1975, J. Atmos. Sci., 32, 362.

Michelson A. A., 1920, Ap J, 51, 257.

Michelson A. A., Pease F. G., 1921, Ap J, 53, 249.

Miura N., Baba N., Isobe S., Noguchi M., Norimoto Y., 1992, J. Modern Opt., 39, 1137.

Monnier J. D., Tuthill P. G., Lopez B., Cruzalébes P., Danchi W. C., Haniff C. A., 1999, Ap J, 512, 351.

Morel S., Koechlin L., 1998, Proc. SPIE on 'Astronomical Interferometry', Hawaii, 3350, 257.

Morris M., 1987, PASP, 99, 1115.

Mouillet D., Larwood J. D., Papaloizou J. C., Lagrange A. M., 1997, MNRAS, 292, 896.

Mourard D., Bonneau D., Koechlin L., Labeyrie A., Morand F., Stee P., Tallon-Bosc I., Vakili F., 1997, A & A, 317, 789.

Mourard D., Bosc I., Labeyrie A., Koechlin L., Saha S., 1989, Nature, 342, 520.

Mourard D., Blazit A., Bonneau D., Koechlin L., Labeyrie A., Morand F., Percheron I., Tallon-Bosc I., Vakili F., 1992, Proc. ESO-NOAO conf. 'High Resolution Imaging Interferometry', ed., J. M. Beckers & F. Merkle, Garching bei München, FRG, 707.

Mourard D., Tallon-Bosc I., Blazit A., Bonneau D., Merlin G., Morand F., Vakili F., Labeyrie A., 1994a, A & A, 283, 705.

Mourard D., Tallon-Bosc I., Rigal F., Vakili F., Bonneau D., Morand F., Stee P., 1994b, A & A, 288, 675.

Mozurkewich D., Johnston K. J., Simon R., Hutter D. J., Colavita M. M., Shao M., Pan X. -P., 1991, A J, 101, 2207.

Nakajima T., Golimowski D. A., 1995, A J, 109, 1181.

Nakajima T., Kulkarni S. R., Gorham P. W., Ghez A. M., Neugebauer G., Oke J. B., Prince T. A., Readhead A. C. S., 1989, A J, 97, 1510.

Neri R., Grewing M., 1988, A & A, 196, 338.

Nightingale N. S., 1991, Experimental Astr., 1, 6.

Nightingale N. S., Buscher D. F., 1991, MNRAS, 251, 155.

Nisenson P., 1988, Proc. NATO-ASI, 'Diffraction Limited Imaging with Very Large Telescopes', ed. D. M. Alloin & J. -M. Mariotti, Cargése, France, 157.

Nisenson P., 1992, Proc. ESO-NOAO conf. 'High Resolution Imaging Interferometry', ed., J. M. Beckers & F. Merkle, Garching bei München, FRG, 299.

Nisenson P., 1997, Private communication.

Nisenson P., Papaliolios C., 1999, Ap J, 518, L29.

Nisenson P., Papaliolios C., Karovska M., Noyes R., 1987, Ap J, 320, L15.

Nisenson P., Stachnik R. V., Karovska M., Noyes R., 1985, Ap J, 297, L17.

Nisenson P., Standley C., Gay D., 1990, Proc. Space Telescope Science Institute Workshop on HST Image Processing, Baltimore, Md.

Northcott M. J., Ayers G. R., Dainty J. C., 1988, J. Opt. Soc. Am. A, 5, 986.

Nota A., Leitherer C., Clampin M., Greenfield P., Golimowski D. A., 1992, A J, 398, 621.

Nulsen P. E. J., Wood P. R., Gilliangham P. R., Bessel M. S., Dopita M. A., McCowage C., 1990, Ap J, 358, 266.

O'Byrne J. W., 1988, PASP, 100, 1169.

Ochs G. R., Lawrence R. S., 1972, N O A A Tech. Rep. E R L 251, W P L, 22.

Osterbart R., Balega Y. Y., Weigelt G., Langer N., 1996, Proc. IAU symp. 180, on 'Planetary Nabulae', ed., H. J. Habing & G. L. M. Lamers, 362.

Osterbart R., Langer N., Weigelt G., 1997, A & A, 325, 609.

Pan X. -P., Shao M., Colavita M. M., 1992, IAU Colloq. 135., ASP Conf. Proc. 32, 'Complementary Approaches to Double and Multiple Star Research', ed. H. A. McAlister and W. I. Hartkopf, 502.

Pan X. -P., Kulkarni S. R., Colavita M. M., Shao M., 1996, Bull. Am. Astron. Soc., 28, 1312.

Papaliolios C., Karovska M., Koechlin L., Nisenson P., Standley C., Heathcote S., 1989, Nature, 338, 565.

Papaliolios C., Nisenson P., Ebstein, S., 1985, App. Opt., 24, 287.

Paresce F., Clampin M., Cox C., Crocker J., Rafal M., Sen A., Hiltner W. A., 1988, Proc., 'Instrumentation for Ground Based Optical Astronomy - Present and Future', ed., L. Robinson, Springer Verlag, New York, 542.

Pauls T. A., Mozurkewich D., Armstrong J. T., Hummel C. A., Benson J. A., Hajian A. R., 1998, Proc. SPIE on 'Astronomical Interferometry', 3350, 467.

Paxman R. G., Schulz T. J., Fienup J. R., (1992), J. Opt. Soc. Am., 9, 1072.

Pedretti E., Labeyrie A., 1999, A & A, (to appear).

Pehlemann E., Hofmann K. -H., Weigelt G., 1992, A & A, 256, 701.

Peraiah A., 1999, Private communication.

Peraiah A., Rao M. S., 1998, A & AS, 132, 45.

Perrin G., du Foresto V. C., Ridgway S. T., Mariotti J. -M., Traub W. A., Carleton N. P., Lacasse M. G., 1998, A & A, 331, 619.

Petr M. G., Du Foresto V., Beckwith S. V. W., Richichi A., McCaughrean M. J., 1998, Ap J, 500, 825.

Petrov R. G., Balega Y. Y., Blazit A., Borgnino, J., Foy R., Lagarde S., Martin F., Vasyuk V. V., 1992, Proc. ESO-NOAO conf. 'High Resolution Imaging Interferometry', ed., J. M. Beckers & F. Merkle, Garching bei München, FRG, 435.

Petrov R., Roddier F., Aime C., 1986, J. Opt. Soc. Am. A, 3, 634.

Poulet F., Sicardy B., 1996, Bull. Astr. Am. Soc., 28, 1124.

Prieur J. -L., Koechlin C., André C., Gallou G., Lucuix C., 1998, Experimental Astr., 8, 297.

Primmerman C. A., Murphy D. V., Page D. A., Zollars B. G., Barclays H. T., 1991, Nature, 353, 141.

Racine R., 1984, in 'Very Large Telescopes, their Instrumentation and Programs', IAU Colloq. no. 79, ESO, ed., M. -H. Ulrich & Kjär, Garching bei München, FRG, 235.

Racine R., Salmon D., Cowley D., Sovka J., 1991, PASP, 103, 1020.

Readhead A. C. S., Nakajima T. S., Pearson T. J., Neugebauer G., Oke J. B., Sargent W. L. W., 1988, A J, 95, 1278.

Reinheimer T., Weigelt G., 1987, A & A, 176, L17.

Rhodes W. T., Goodman J. W., 1973, J. Opt. Soc. Am., 63, 647.

Ribak E., 1986, J. Opt. Soc. Am. A, 3, 2069.

Ribak E., Lipson S. G., 1981, App. Opt., 20, 1102.

Ribak E., Leibowitz E., Hege E. K., 1985, App. Opt., 24, 3094.

Richardson L. F., 1922, 'Weather Prediction by Numerical Process, Intro': S. Chapman., Cambridge Uni. Press, N. Y.

Ricort G., Aime C., 1979, A & A, 76, 324.

Ridgway S. T., 1988, Proc. NATO-ASI, 'Diffraction Limited Imaging with Very Large Telescopes', ed. D. M. Alloin & J. -M. Mariotti, Cargése, France, 307.

Ridgway S. T., 1992, Proc. ESO-NOAO conf. 'High Resolution Imaging Interferometry', ed., J. M. Beckers & F. Merkle, Garching bei München, FRG, 653.

Riguat F., Cuby J. -G., Caes M., Monin J. -L., Vittot M., Richard J. -C., Rousset G., Léna P., 1992, A & A, 259, L57.

Rigaut F., Salmon D., Arsenault R., Thomas J., Lai O., Rouan D., Véran J. P., Gigan P., Crampton D., Fletcher J. M., Stilburn J., Boyer C., Jagourel P., 1998, PASP, 110, 152.

Robertson J. G., Bedding T. R., Aerts C., Waelkens C., Marson R. G., Barton J. R., 1999, MNRAS, 302, 245.

Roddier C., Roddier F., 1983, Ap J, 270, L23.

Roddier C., Roddier F., 1988, Proc. NATO-ASI, 'Diffraction Limited Imaging with Very Large Telescopes', ed. D. M. Alloin & J. -M. Mariotti, Cargése, France, 221.

Roddier C., Roddier F., Northcott M. J., Graves J. E., Jim K., 1996, Ap J, 463, 326.

Roddier F., 1981, Progress in Optics, XIX, 281.

Roddier F., 1986, Opt. Commun., 60, 145.

Roddier F., 1988a, Proc. NATO-ASI, 'Diffraction Limited Imaging with Very Large Telescopes', ed. D. M. Alloin & J. -M. Mariotti, Cargése, France, 33.

Roddier F., 1988b, Phys. Rep., 170, 97.

Roddier F., 1988c, App. Opt., 27, 1223.

Roddier F., 1990, Opt. Eng., 29, 1239.

Roddier F., 1994, in 'Adaptive Optics in Astronomy', ed., M. A. Esley & F. Merkle, SPIE, Bellingham, WA, 1487, 123.

Roddier F. J., Graves J. E., McKenna D., Northcott M. J., 1991, SPIE Conf., 1524, 248.

Roddier F., Roddier C., 1985, Ap J, 295, L21.

Roddier F., Roddier C., 1997, PASP., 109, 815.

Roddier F., Roddier C., Brahic A., Dumas C., Graves J. E., Northcott M. J., Owen T., 1997, Planet Sp. Sci., 45, 1031.

Roddier F., Roddier C., Graves J. E., Northcott M. J., 1995, Ap J, 443, 249.

Rodriguez L. F., Sosa N., Rosa F., Fuensalida J. J., 1992, Proc. ESO-NOAO conf. 'High Resolution Imaging Interferometry', ed., J. M. Beckers & F. Merkle, Garching bei München, FRG, 621.

Roggemann M. C., Welsh B. M., Fugate R. Q., 1997, Rev. Modern Phys., 69, 437.

Rogstad D. H., 1968, App. Opt., 7, 585.

Rouan D., 1996, Proc. NATO-ASI, 'High Resolution in Astrophysics', Les Houches, France, ed. A. M. Lagrange, D. Mourard & P. Léna, 293.

Rouan D., Field D., Lemaire J. -L., Lai O., de Foresto G. P., Falgarone E., Deltorn J. -M., 1997, MNRAS, 284, 395.

Rouan D., Rigaut F., Alloin D., Doyon R., Lai O., Crampton D., Gendron E., Arsenault R., 1998, astro-ph/9807053, A & A.

Rousset G., 1999, 'Adaptive Optics in Astronomy', ed. F. Roddier, Cambridge Univ. Press, 91.

Rousset G., Fontanella J. C., Kem P., Gigan P., Rigaut F., Léna P., Boyer P., Jagourel P., Gaffard J. P., Merkle F., 1990, A & A, 230, L29.

Ryan S. G., Wood P. G., 1995, Pub. ASA., 12, 89.

Saha S. K., 1999, Ind. J. Phys., 73B, 552.

Saha S. K., Chinnappan V., 1999, BASI, 27, 327.

Saha S. K., Jayarajan A. P., Rangarajan K. E., Chatterjee S., 1988, Proc. ESO-NOAO conf. 'High Resolution Imaging Interferometry', ed. F. Merkle, Garching bei München, FRG, 661.

Saha S. K., Jayarajan A. P., Sudheendra G., Umesh Chandra A., 1997a, BASI, 25, 379.

Saha S. K., Nagabhushana B. S., Ananth A. V., Venkatakrishnan P., 1997b, Kod. Obs. Bull., 13, 91.

Saha S. K., Rajamohan R., Vivekananda Rao P., Som Sunder G., Swaminathan R., Lokanadham B., 1997c, BASI, 25, 563.

Saha S. K., Sankarasubramanian K., Sridharan R., 1999d, 'Auto-correlation of Binary stars' (in preparation).

Saha S. K., Sridharan R., Sankarasubramanian K., 1999b, 'Speckle image reconstruction of binary stars', Submitted to BASI.

Saha S. K., Sridharan R., Sankarasubramanian K., 1999c, 'Triple correlation of Binary stars' (in preparation).

Saha S. K., Sudheendra G., Umesh Chandra A., Chinnappan V., 1999, Experimental Astr., 9, 39.

Saha S. K., Venkatakrishnan P., 1997, BASI, 25, 329.

Saha S. K., Venkatakrishnan P., Jayarajan A. P., Jayavel N., 1987, Curr. Sci., 56, 985.

Sams B. J., Schuster K., Brandl B., 1996, Ap. J., 459, 491.

Sandler D., Cuellar L., Lefebvre M., Barrett T., Arnold R., Johnson P., Rego A., Smith G., Taylor G., Spivey B., 1994, J. Opt. Soc. Am. A, 11, 858.

Saxena A. K., 1993, Private communication.

Saxena A. K., Jayarajan A. P., 1981, App. Opt., 20, 724.

Saxena A. K., Lancelot J. P., 1982, App. Opt., 21, 4030.

Schertl D., Hofmann K. -H., Seggewiss W., Weigelt G., 1996, A & A, 302, 327.

Schöller M., Brandner W., Lehmann T., Weigelt G., Zinnecker H., 1996, A & A, 315, 445.

Séchaud M., 1999, 'Adaptive Optics in Astronomy', ed. F. Roddier, Cambridge Univ. Press, 57.

Seldin J. H., Paxman R. G., 1994, Proc. SPIE., 2302, 268.

Shao M., 1988, Proc. ESO-NOAO conf. 'High Resolution Imaging Interferometry', ed., F. Merkle, Garching bei München, FRG, 823.

Shao M., Colavita M. M., 1987, Proc. ESO-NOAO Workshop., ed. J. W. Goad, 115.

Shao M., Colavita M. M., 1994, IAU Symp. 158, 'Very high resolution imaging', ed., J. G. Robertson and W. J. Tango, 413.

Shao M., Colavita M. M., Hines B. E., Staelin D. H., Hutter D. J., Johnston K. J., Mozurkewich D., Simon R. H., Hershey J. L., Hughes J. A., Kaplan G. H., 1988, A & A, 193, 357.

Shao M., Colavita M. M., Hines B. E., Hershey J. L., Hughes J. A., Hutter D. J., Kaplan G. H., Johnston K. J., Mozurkewich D., Simon R. H., Pan X. -P., 1990, A J, 100, 1701.

Shao M., Colavita M. M., Staelin D. H., 1986a, Proc. SPIE, 628, 250.

Shao M., Colavita M. M., Staelin D. H., Simon R., Johnston K. J., 1986b, Proc. IAU symposium 109, 46.

Shao M., Staelin D. H., 1980, App. Phys., 19, 1519.

Shelton J. C., Baliunas S. L., 1993, Proc. SPIE., on 'Active and Adaptive Optical Components and Systems II', 1920, 371.

Shields G. A., 1999, astro-ph/9903401., PASP.

Sicardy B., Roddier F., Roddier C., Perozzi E., Graves J. E., Guyon O., Northcott M. J., 1999, Nature, 400, 731.

Siegmund O. H. W., Lampton M., Bixler J., Chakrabarti S., Vallaga J., Bowyer S., Malina R. F., 1986, J. Opt. Soc. Am., 3, 2139.

Siegmund O. H. W., Stock J. M., Marsh D. R., Gummin M. A., Raffanti R., Hull J., Gaines G. A., Welsh B. Y., Donakowski B., Jelinsky P. N., Sasseen T., Tom J. L., Higgins B., Magoncelli T., Hamilton W., Battel S. J., Poland A. L., Jhabvala M. D., Sizemore J., Shannon J., 1994, Proc. SPIE, 2280, 89.

Simon M., Close L. M., Beck T. L., 1999, A J, 117, 1375.

Singh K., 1999, Private communication.

Sridharan R., Venkatakrishnan P., 1999, 'Speckle image reconstruction of solar features', Presented at the XIX ASI meeting, Bangalore, India, Feb. 1-4, 1999.

Stachnik R. V., Nisenson P., Ehn D. C., Hudgin R. H., Schirf V. E., 1977, Nature, 266, 149.

Stachnik R. V., Nisenson P., Noyes R. W., 1983, Ap J, 271, L37.

Stahl S. S., Sandler D. G., 1995, Ap J, 454, L153.

Stee P., 1999, http://www.obs-nice.fr/stee/welcome.html

Stee P., de Araújo, Vakili F., Mourard D., Arnold I., Bonneau D., Morand F., Tallon-Bosc I., 1995, A & A, 300, 219.

Stee P., Vakili F., Bonneau D., Mourard D., 1998, A & A, 332, 268.

Tallon M., Foy R., 1990, A & A, 235, 549.

Tallon M., Foy R., Blazit A., 1988, ESO Conf. on 'Very Large Telescopes and their Instrumentation', ed. M.-H. Ulrich, 743.

Tatarski V. I., 1967, 'Wave Propagation in a Turbulent Medium', Dover, N. Y.

Tatarski V. I., 1968, 'The Effect of the Turbulent Atmosphere on Wave propagation', N S F Report TT-68-50464.

Tatarski V. I., 1993, J. Opt. Soc. Am. A, 56, 1380.

Taylor G. L., 1921, in 'Turbulence', ed., S. K. Friedlander & L. Topper, 1961, Wiley-Inerscience, N. Y., 1.

Taylor G. L., 1935, in 'Turbulence', ed., S. K. Friedlander & L. Topper, 1961, Wiley-Inerscience, N. Y., 18.

Tej A., Chandrasekhar T., Ashok M. N., Ragland S., Richichi A., Stecklum B., 1999, A J, 117, 1857.

Thiébaut E., 1994, A & A, 284, 340.

544   S. K. Saha

Thiébaut E., Balega Y., Balega I., Belkine I., Bouvier J., Foy R., Blazit A., Bonneau D., 1995, A & A, 304, L17.

Thom C., Granes P., Vakili F., 1986, A & A, 165, L13.

Thompson L. A., Gardner C. S., 1988, Nature, 328, 229.

Thureau N., Chesneau O., Berio P., Bonneau D., Mourard D., Stee P., Vakili F., Verinaud C., 1998, Proc. SPIE on 'Astronomical Interferometry', 3350, 505.

Timothy J. G., 1986, SPIE Ultraviolet Technology, 687, 109.

Timothy J. G., 1993, Proc. SPIE., 1982, 4.

Timothy J. G., Morgan J.S., Slater D. C., Kasle D. B., Bybee R. L., Culver H. K., 1989, Proc., SPIE, 1158, Ultraviolet Technology III, ed. R. E. Huffmann, 104.

Tokovinin A., 1992, Proc. ESO-NOAO conf. 'High Resolution Imaging Interferometry', ed., J. M. Beckers & F. Merkle, Garching bei München, FRG, 425.

Tokovinin A., 1997, A & AS, 124, 75.

Torres G., Stefanik R. P., Latham D. W., 1997, Ap J, 485, 167.

Troxel S. E., Welsh B. M., Roggemann M. C., 1994, J. Opt. Soc. Am A, 11, 2100.

Tsvang L. R., 1969, Radio Sci., 4, 1175.

Tuthill P. G., Haniff C. A., Baldwin J. E., 1997, MNRAS, 285, 529.

Tuthill P. G., Haniff C. A., Baldwin J. E., 1999a, MNRAS, 306, 353.

Tuthill P. G., Monnier J. D., Danchi W. C., 1999b, Nature, 398, 487.

Twichell J. C., Burke B. E., Reich R. K., McGonagle W. H., Huang C. M., Bautz M. W., Doty J. A., Ricker G. R., Mountain R. W., Dolat V. S., 1990, A. Rev. Sci. Instrum., 61, 2744.

Ulrich M. -H., 1988, Proc. ESO-NOAO conf. 'High Resolution Imaging Interferometry', ed. F. Merkle, Garching bei München, FRG, 33.

Vakili F., Berio P., Bonneau D., Chesneau O., Mourard D., Stee P., Thureau N., 1998a, Proc., 'Be stars', ed. A. M. Hubert and C. Jaschek, 173.

Vakili F., Mourard D., Bonneau D., Morand F., Stee P., 1997, A & A, 323, 183.

Vakili F., Mourard D., Stee P., Bonneau D., Berio P., Chesneau O., Thureau N., Morand F., Labeyrie A., Tallon-Bosc I., 1998b, A & A, 335, 261.

van Belle G. T., Boden A. F., Colavita M. M., Shao M., Vasisht G., Wallace J. K., 1998, Proc. SPIE on 'Astronomical Interferometry', 3350, 362.

van Belle G. T., Dyck H. M., Benson J. A., Lacasse M. G., 1996, A J, 112, 2147.

van Belle G. T., Dyck H. M., Thompson R. R., Benson J. A., Kannappan S. J., 1997, A J, 114, 2150.

Vasisht G., Boden A. F., Colavita M. M., Crawford S. L., Shao M., Swanson P., van Belle G. T., Wallace J. K., 1998, Proc. SPIE on 'Astronomical Interferometry', 3350, 354.

Venkatakrishnan P., 1987, MNRAS, 229, 379.

Venkatakrishnan P., Chatterjee S., 1987, MNRAS, 224, 265.

Venkatakrishnan P., Saha S. K., Shevgaonkar R. K., 1989, Proc., 'Image Processing in Astronomy', ed. T. Velusamy, 57.

Vernin J., Weigelt G., Caccia J. L., Müller M., 1991, A & A, 243, 553.

Von der Lühe O., 1984, J. Opt. Soc. Am. A, 1, 510.

Von der Lühe O., 1989, in High Spatial Resolution Solar Observation, Proc. of the Tenth Sermento Peak Summer Workshop, ed., O. Von der Lühe, Sunspot, New Mexico.

Von der Lühe O., Dunn R. B., 1987, A & A, 177, 265.

Von der Lühe O., Pehlemann E., 1988, Proc. ESO-NOAO conf. 'High Resolution Imaging Interferometry', ed., F. Merkle, Garching bei München, FRG, 159.

Von der Lühe O., Zirker J. B., 1988, Proc. ESO-NOAO conf. 'High Resolution Imaging Interferometry', ed., F. Merkle, Garching bei München, FRG, 77.

Walker G., Chapman S., Mandushev G., Racine R., Nadeau D., Doyon R., Véran J. P., 1998, astro-ph 9810443.

Walters D. L., Kunkel K. E., 1981, J. Opt. Soc. Am., 71, 397.

Weigelt G., 1977, Opt. Communication, 21, 55.

Weigelt G., 1978, App. Opt., 17, 2660.

Weigelt G., 1988, Proc. NATO-ASI, 'Diffraction Limited Imaging with Very Large Telescopes', ed. D. M. Alloin & J. -M. Mariotti, Cargése, France, 191.

Weigelt G., Bair G., 1985, A & A, 150, L18.

Weigelt G., Balega Y., Blöcker T., Fleischer A. J., Osterbart R., Winters J. M., 1998, A & A, 333, L51.

Weigelt G., Balega Y., Hofmann K. -H., Scholz M., 1996, A & A, 316, L21.

Weigelt G., Balega Y., Preibisch T., Schertl D., Schöller M., Zinnecker H., 1999, astro-ph/9906233 (to appear in A & A).

Weigelt G., Ebersberger J., 1986, A & A, 163, L5.

Weigelt G., Grieger F., Hofmann K. -H., Pausenberger R., 1992, Proc. ESO-NOAO conf. 'High Resolution Imaging Interferometry', ed., J. M. Beckers & F. Merkle, Garching bei München, FRG, 471.

Weinberger A. J., Neugebauer G., Mathews K., 1996, MNRAS, 196, 1005.

Weitzel N., Haas M., Leinert Ch., 1992, Proc. ESO-NOAO conf. 'High Resolution Imaging Interferometry', ed., J. M. Beckers & F. Merkle, Garching bei München, FRG, 511.

Wilken V., de Boer C. R., Denkar C., Kneer F., 1997, A & A, 325, 819.

Wilson R. W., Baldwin J. E., Busher D. F., Warner P. J., 1992, MNRAS, 257, 369.

Wilson R. W., Dhillon V. S., Haniff C. A., 1997, MNRAS, 291, 819.

Wirnitzer B., 1985, J. Opt. Soc. Am. A, 2, 14.

Wittkowski M., Balega Y., Beckert T., Duschi W. J., Hofmann K. -H., Weigelt G., 1998b, A & A, 329, L45.

Wittkowski M., Langer N., Weigelt G., 1998a, A & A, 340, L39.

Wizinovitch P. L., Nelson J. E., Mast T. S., Glecker A. D., 1994, Proc. SPIE., on 'Adaptive Optics in Astronomy', 2201, 22.

Wood P. R., 1985, Proc., A S A, 6, 120.

Wood P. R., Bessel M. S., Dopita M. A., 1986, Ap J, 311, 632.

Wood P. R., Meatheringham S. J., Dopita M. A., Morgan, D. M., 1987, Ap J, 320, 178.

Wood P. R., Nulsen P. E. J., Gillingham P. R., Bessel M. S., Dopita M. A., McCowage C., 1989, Ap J, 339, 1073.

Woolf N. J., Cheng A., 1988, ESO Conf. on 'Very Large Telescopes and their Instrumentation', ed. M.-H. Ulrich, 845.

Worden S. P., Lynds C. R., Harvey J. W., 1976, J. Opt. Soc. Am., 66, 1243.

Wyngaard J. C., Izumi Y., Collins S. A., 1971, J. Opt. Soc. Am., 60, 1495.

Wyant J. C., 1974, App. Opt., 13, 200.

Wyant J. C., Kaliopoulos C. L., 1981, in Agard Conf. Proc., 300.

Young J. S., Baldwin J. E., Beckett G., Boysen R. C., Haniff C. A., Lawson P. R., Mackay C. D., Rogers J., St-Jacques D., Warner P. J., Wilson D. M. A., 1998, Proc. SPIE., on 'Astronomical Interferometry', 3350, 746.

Young S., Packham C., Hough J. H., Efstathiou A., 1996, MNRAS, 283, L1.

Zago L., 1995, http://www.eso.org/gen-fac/pubs/astclim/lz-thesis/node4-html.

Zappa F., Lacaita A. L., Cova S. D., Lovati P., 1996, Opt. Eng., 35, 938.

Zeidler P., Appenzeller I., Hofmann K. -H., Mauder W., Wagner S., Weigelt G., 1992, Proc. ESO-NOAO conf. 'High Resolution Imaging Interferometry', ed., J. M. Beckers & F. Merkle, Garching bei München, FRG, 67.

Zienkiewicz O. C., 1967, 'The Finite Element Methods in Structural and Continuum Mechanics', McGrawhill Publication.

Appendix I

Table of symbols

$V(\mathbf{r}, t)$	the monochromatic optical wave
$\mathbf{r} = (x, y, z)$	position vector of a point in space
t	time
ν_0	frequency of the wave

$a(\mathbf{r})$	complex amplitude of the wave
$\mathcal{U}(\mathbf{r},t)$	complex representation of the analytical signal
$\Psi(\mathbf{r})$	complex vector functions of position $\mathbf{r}$
$\Psi(\mathbf{x})$	complex amplitude in the image plane
$\mathcal{I}(\mathbf{x})$	intensity of light
$<\ >$	ensemble average
$*$	complex operator
λ	wavelength
$\mathbf{x}=(x,y)$	2-dimensional space vector
$\Psi_\circ(\mathbf{x}_\circ)$	complex amplitude in the telescope pupil plane
$\mathcal{T}(\mathbf{x},\mathbf{x}_\circ)$	impulse response of the optical system
$\mathcal{P}(\mathbf{x})$	the pupil transmission function
$*$	convolution operator
$\widehat{\mathcal{P}}(\mathbf{u})$	transfer function
$\mathcal{S}(\mathbf{x})$	point spread function (PSF)
$\widehat{\mathcal{S}}(\mathbf{u})$	optical transfer function (OTF)
$\mid\widehat{\mathcal{S}}(\mathbf{u})\mid^2$	modulus transfer function (MTF)
$\mathcal{R}$	resolving power of an optical system
ω	angular frequency
T	period
$\mathbf{V}_j$	monochromatic wave vector
j	$=1,2,3$
$\mathcal{J}_{12}$	interference term
δ	phase difference
$\Delta\varphi$	optical path difference (OPD)
$\lambda_\circ$	wavelength in vacuum
$\mathbf{K}_j$	constants
r_j	pin-holes in the wave field
s_j	distances of a meeting point of the two beams from the two pin-holes
τ_j	travel time from the respective pin-holes to the meeting point
c	velocity of light
$\boldsymbol{\gamma}_{12}(\tau)$	complex degree of (mutual) coherence
$\boldsymbol{\Gamma}_{12}(\tau)\cdot$	mutual coherence
$\boldsymbol{\Gamma}_{11}(\tau)$	self coherence
τ	delay
τ_c	temporal width or coherence time
$\Delta\nu$	spectral width
l_c	coherence length
$\boldsymbol{\gamma}_{12}(0)$	spatial coherence
ψ_{12}	argument of $\boldsymbol{\gamma}_{12}(\tau)$
x	distance from the origin
z	distance from the aperture
$d(x)$	OPD corresponding to x
b	distance between the two apertures
$\mathcal{V}$	contrast of the fringes

$\mathbf{B}$	baseline vector
D	diameter of the sub-apertures
f	focal length
$\Psi(D \cdot x)$	envelop of the image of each sub-apertures (Airy disk)
ψ_B	phase of $\gamma_B(0)$
d	extra optical path in front of one aperture
v_a	average velocity of a viscous fluid
l	characteristic size of viscous fluid
R_e	Reynolds number
ν_v	kinematic viscosity of fluid
L_0	outer scale length
k_{L_0}	spatial frequency of outer scale
$n(\mathbf{r}, \mathbf{t})$	refractive index of the atmosphere
n_0	mean refractive index of air
P	pressure
T	temperature
$\Phi_n(\mathbf{k})$	power spectral density
k_0	critical wave number
l_0	inner scale length
k_{l_0}	spatial frequency of inner scale
C_n^2	refractive index structure constant
$\mathcal{D}_n(\mathbf{r})$	refractive index structure function
$\mathcal{B}_n(\mathbf{r})$	covariance function
$\mathcal{D}_v(\mathbf{r})$	velocity structure function
C_v^2	velocity structure constant
$\mathcal{D}_T(\mathbf{r})$	temperature structure function
C_T^2	temperature structure constant
h	height
$(\mathbf{x}, h)$	co-ordinate
$\Psi_h(\mathbf{x})$	complex amplitude at co-ordinate, $(\mathbf{x}, h)$
$< \psi_h(\mathbf{x}) >$	average value of the phase at h
δh_j	thickness of the turbulence layer
$\mathcal{D}_{\psi_j}(\boldsymbol{\xi})$	phase structure function
$\mathcal{D}_n(\boldsymbol{\xi}, \zeta)$	refractive index structure function
$\mathcal{B}_{h_j}(\boldsymbol{\xi})$	covariance of the phase
$\mathcal{B}(\boldsymbol{\xi})$	coherence function
γ	distance from the zenith
r_0	Fried's parameter
$\mathcal{O}(\mathbf{x})$	object illumination
$< \widehat{\mathcal{S}}(\mathbf{u}) >$	transfer function for long-exposure images
$\mathbf{u}$	spatial frequency vector with magnitude u
$\widehat{\mathcal{I}}(\mathbf{u})$	image spectrum
$\widehat{\mathcal{O}}(\mathbf{u})$	object spectrum
$\mathcal{B}(\mathbf{u})$	atmosphere transfer function
$\mathcal{T}(\mathbf{u})$	telescope transfer function

$\psi(\mathbf{u})$	Fourier phase at $\mathbf{u}$
$arg \,\|\,\|$	the phase of ' '
$\mathcal{P}$	aperture of large telescope
p_j	sub-apertures
σ	coherence area
$\mathcal{N}_j(\mathbf{x})$	noise contamination
$\mathcal{W}(\mathbf{x})$	intensity distribution of objective prism speckle spectrogram
$\mathcal{G}_m(\mathbf{x})$	spectrum of the object pixel
$\mathcal{D}_\mathcal{I}(\mathbf{x})$	differential image
β_{123}	closure phase
θ_i, θ_j	error terms introduced by errors at the individual antennae
$\mathcal{A}\delta(\mathbf{x})$	Dirac impulse of a point source
$\mathcal{C}_{\mathcal{O}_1}(\mathbf{x})$	autocorrelation of the object
$\mathbf{x}_k$	position of the brightest pixel
$\mathcal{I}_{sa}(\mathbf{x})$	shift-and-add image
$w[\mathcal{I}_k(\mathbf{x}_k)]$	weighting of the brightest pixel
$mask_m(\mathbf{x})$	m^{th} speckle mask
$m\mathcal{I}_m(\mathbf{x})$	m^{th} masked speckled image
$\otimes$	correlation
$\mathbf{x}'_k$	constant position vectors
d_k	positive constant
$\mathcal{N}(\mathbf{u})$	noise spectrum
$<\|\widehat{\mathcal{I}}(\mathbf{u})\|^2>$	image energy spectrum
$\Delta\mathbf{u}$	offset spatial frequency
$\theta_{\mathcal{O}}^{TC}$	phase of the bispectrum
θ_j	apertures